Development of a Handheld Fiber-Optic Probe-Based Raman Imaging Instrumentation: Raman ChemLighter

Kumulative Dissertation

zur Erlangung des akademischen Grades Doktor-Ingenieur

(Dr. -Ing.)

vorgelegt dem Rat der Chemische-Geowissenschaftlichen Fakultät der

Friedrich-Schiller-Universität Jena von

Master of Engineering (M. Eng.) Wei Yang

geboren am 25.10.1989 in Hubei, China

Gutachter

1. Prof. Dr. Jürgen Popp
   Institut für Physikalische Chemie, Friedrich-Schiller-Universität Jena
2. Prof. Dr. Iwan W. Schie
   Fachbereich Medizintechnik und Biotechnologie, Ernst-Abbe-Hochschule Jena

Tag der Verteidigung: 17. Februar 2022

Contents

List of Figures

List of Abbreviations

2D	2-Dimensional
3D	3-Dimensional
AC	Alternating Current
ADUs	analog-digital-units
CARS	Coherent anti-Stokes Raman Scattering
CCD	Charged Coupled Device
CMOS	Complementary Metal–oxide–Semiconductor
CT	Computed Tomography
FLIm	Fluorescence Lifetime Imaging microscopy
FOV	Field of View
FPC	Flexible Printed Circuit
HCA	Hierarchical Cluster Analysis
Lidar	Light Detection and Ranging
LUT	Look-up Table
MRI	Magnetic Resonance Imaging
NA	Numerical Aperture
OCT	Optical Coherence Tomography
PCA	Principal Component Analysis
ROI	Region of Interest
SHG	Second Harmonic Generation
UV	Ultraviolet

1. Introduction

1.1 Motivation

Raman spectroscopy is a highly promising optical modality that enables the provision of label-free, non-contacted, non-invasive, and fingerprinting information of molecular vibrations, and has been applied in different fields, such as analytical chemistry, material science, clinical analytics, biology, and pharmacy [1]. In recent years, Raman-based technologies have shown significant promise for biomedical and clinical applications, especially in the field of medical diagnosis, e.g. tumor characterization, or delineation between tumor and healthy tissues [2–7]. In general, commercially available Raman systems are mostly based on a confocal imaging microscope. The configuration of this kind of system contains a standard optical microscope, equipped with a Raman unit, which shares the optical transmission path with the microscope, but uses a different set of excitation and acquisition components. The advantage of the system is that it allows users to observe the brightfield image of the sample with a selected magnification and adapted field of view (FOV) on a micro-scale, and to automatically map a defined region of interest (ROI). The Raman signal is generated in the focal spot of the excitation laser on the sample, and mapping is realized by acquiring signals at each location and mechanically translating the sample following a defined grid. From Raman mapping, it is quite straightforward to construct Raman images through simple plotting of the intensity of certain Raman band, or based on a more complex analysis of the entire Raman spectra. Raman images visualize the spectroscopic information related to the distribution of macromolecules in the sample and allow to overly with brightfield images for further diagnosis and delineation of the distribution. These microscopy Raman devices have been widely used for *ex vivo* Raman imaging of tissue or biopsies [8–10]. Nevertheless, this kind of Raman system is usually large, rigid, and not very portable, only allowing *ex vivo* measurements with minimal access to the patient site. On the contrary, benefitting from its intrinsically smaller size, Raman systems based on fiber-optical probes display significant advantages in comparison to high-performance, but rigid confocal microscopy systems, as it enables direct access to the measurement sites, and easier to translate to clinical in-vivo applications [11–13]. However, there are still three

common disadvantages that significantly hamper the application of fiber-optic Raman spectroscopy in broader clinical scenarios:

(1) Focus disadvantage: In general, Raman probes acquire scattered signals in-contact with the sample surface or by focusing the excitation laser through a focal objective lens for more efficient excitation and collection. While the in-contact acquisition mode may be restricted to only a few instances [14], it is mandatory to avoid any disturbance or contamination of the sample surface and the probe head. Furthermore, using a probe in-contact mode increases the risk of deforming and damaging the sample. Employing probes equipped with a focal objective lens avoids the aforementioned alterations of the sample, however, requires the user to permanently maintain the probe at its focal distance relative to the sample surface for effectively exciting and collecting the Raman signal. Attaching a removable distance regulator [15] to the tip of the probe may circumvent this challenge, but this approach suffers from the same drawbacks as the in-contact acquisition, e.g. sample contamination. Thus, there is an urgent demand for such kind of fiber-optic probes, which allow for efficient non-contact measurement, but also have the ability to automatically maintaining the correct focal distance relative to the sample surface.

(2) Single point-measurement: Acquiring the Raman scattering signal generated within the focal spot of the excitation laser through an objective lens also implies that the probe only has the point-measurement ability. Due to the rigid built, conventional Raman mapping performed by mechanical translation of samples cannot be easily realized within *in vivo* measurement scenarios in operating theatres. Although there are methods to achieve scanning, for example, based on physical tracking of the probe movement, which involves passively registering the coordinates of the surgeon's hand or robotic arm [16–18], the task becomes very complex. Thus, there is a demand for an approach that enables dynamical tracking of the movements of the probe, while allowing simple co-registration of the Raman information together with the measurement positions.

(3) Direct visualization and 3D visualization: The current lack of straightforward methods to co-register the Raman information with the positions prevents visualization of the Raman data in an intuitive and easily understandable way. The off-line processing and data analysis after the acquisition of spectra for conventional Raman imaging severely delays the diagnostic correlation of the spectral information sample. To overcome these obstacles, it is

necessary to implement a Raman imaging method with on-line data analysis and real-time visualization. Besides the real-time data analysis and visualization, many clinically relevant samples have also a defined topography, which is largely ignored during the acquisition, and Raman images are normally acquired from an X-Y coordinate two-dimensional (2D) plane, neglecting the height information of the sample. It is very attractive and interesting to combine 3D reconstruction methods with Raman modalities to offer the potential clinical user scenario powerful tool, which not only reveals the distribution of macromolecules on the surface but also take height information of the sample into consideration.

These common disadvantages of fiber-optic Raman probes motivate the investigations in this thesis. To address these issues, it is necessary to briefly refer to the theory of Raman scattering and the current state-of-the-art techniques in the field of Raman spectroscopy. Following that, related methods and detailed explanations of each issue and proposed approaches will be provided in chapter 2 and chapter 3.

1.2 Theory of the Raman Scattering process

In the letter published by C. V. Raman and K. S. Krishnan in *Nature* in 1928 [19], they first pointed out that there is secondary radiation with at red-shifted wavelengths in scattered light, that experimentally opened up the study of inelastic scattering interactions between light and matter (molecules). This light scattering phenomenon is known as the Raman Effect, named after the discoverer. The external incident electromagnetic wave **E** induces displacements of the electron cloud within the molecule, resulting in an induced dipole moment **P** of the molecule given by [20]:

$$P = \alpha E = \alpha E_0 \cos 2\pi \nu_0 t \tag{1-1}$$

where α is the polarizability of the molecule. The polarizability measures the deformability of the molecules' electron cloud upon interaction with the external electric field. E_0 and ν_0 are the amplitude and frequency of the incident electromagnetic wave at time t, respectively. The polarizability is modulated by the molecular vibration and expressed as a Taylor series expanded around equilibrium nuclear geometry q = 0. The molecular vibration usually is considered as a harmonic oscillation at the frequency ν_R with the amplitude of q_0, so that:

$$\alpha = \alpha(0) + \left(\frac{\partial\alpha}{\partial q}\right)_{q=0} \cdot q + \cdots$$
$$q = q_0 \cos 2\pi\nu_R t \tag{1-2}$$

Taking Eq. (1-1) and Eq. (1-2) into account, ignoring higher-order terms in Eq. (1-2) and doing basic trigonometric transformation, one can get:

$$\begin{aligned} P = {} & \alpha(0)E_0 \cos 2\pi\nu_0 t \\ & + \frac{1}{2}\left(\frac{\partial\alpha}{\partial q}\right)_{q=0} E_0 q_0 \cos 2\pi(\nu_0 - \nu_R)t \\ & + \frac{1}{2}\left(\frac{\partial\alpha}{\partial q}\right)_{q=0} E_0 q_0 \cos 2\pi(\nu_0 + \nu_R)t \end{aligned} \tag{1-3}$$

According to the classical analysis, the polarized electrons radiate light at the frequency of their oscillations. It also agrees with the modern quantum analysis that Raman scattering can be considered as an interaction between light and molecules in vibrational states, where a photon excites the molecule to a short-lived intermediate state (virtual state). The photon interacts elastically with the molecule resulting in a scattered photon of the same energy as the incident one, which is indicated as the first right-hand side term of Eq. (1-3), known as Rayleigh scattering (green, middle in Figure 1.1). There is a very small probability, typically less than one photon in a million that the incident photon interacts inelastically with the molecule upon energy transfer between them. The case of energy transfer from the photon to the molecule, results in excitation of vibrational states is called Stokes scattering (red, left in Figure 1.1), which is indicated by the second term of Eq. (1-3). The other case of energy transfer from the molecule in excited vibrational states to the photon is called anti-Stokes scattering (blue, right in Figure 1.1), which indicates the third part of Eq. (1-3). According to the Boltzmann distribution, at room temperature, the vibrational ground state is more populated than higher vibrational states, which makes anti-Stokes scattering less probable than Stokes scattering. This also explains that in vibrational spectra Stokes scattering occurs with higher intensity comparing to anti-Stokes so that Stokes scattering is referred to Raman scattering. The vibrational modes ν_R of a given molecule are inherently depending on its chemical structure, i.e. number and mass of constituting atoms as well as the type of chemical bonds between them, which is unique for different molecules. Therefore, the analysis of a Raman spectrum allows to identify and discriminate molecules in a mixture of compounds. From Eq. (1-3), one can also see that Raman scattering only occurs under the condition that the polarizability of a molecule

changes upon vibration. From the classical treatment for calculating the emitted power of a Hertzian dipole, the Raman intensity I_{Raman} depends among others on the intensity I_0 of excitation light as well as the number of molecules N within the excitation volume:

$$I_{Raman} \sim N\, I_0\, (\nu_0 - \nu_R)^4 \left[\left(\frac{\partial \alpha}{\partial q}\right)_{q=0}\right]^2 \tag{1-4}$$

Eq. (1-4) shows the Raman intensity (I_{Raman}) is related to the density of the sample, excitation light intensity (I_0) and frequency (wavelength) of the incoming light, and the induced polarizability derivative.

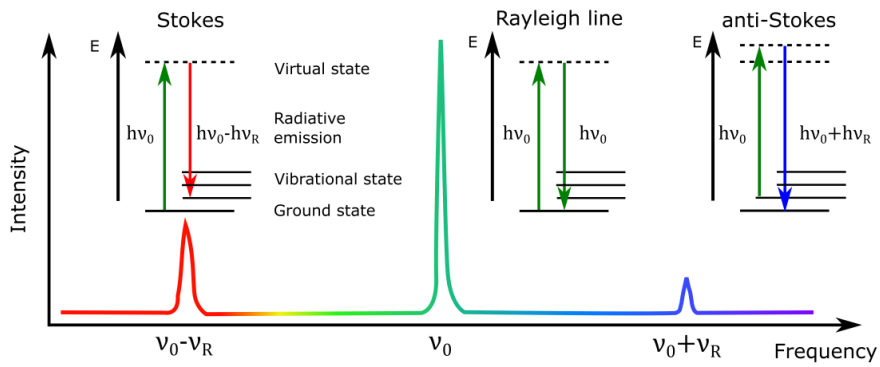

Figure 1.1 Band diagrams of scattering and related Jablonski diagrams. Stokes scattering in red, Rayleigh scattering in green and anti-Stokes scattering in blue of which are results of interactions between photons and molecules in the ground state or vibrational state.

1.3 Raman instrumentation and Raman probes

Raman spectroscopy is a low-light implementation, i.e. less than one in a million photons is scattered inelastically so that successful observation of Raman scattering and acquiring meaningful molecular information is strongly dependent on the instrumentation to facilitate the measurement of the weak signals. Figure 1.2 (a) shows the configuration of a typical Raman microscope. The monochromatic excitation laser light is delivered by fiber and collimated to pass through a band-pass filter removing undesired silica Raman background from the excitation fiber. Then the excitation beam is reflected by a dichroic mirror and focused on the sample by an objective lens. The generated Raman signal is collected by the same objective lens and subsequently passed through a long-pass filter to suppress the Rayleigh line. Finally, the scattered light is coupled into a collection fiber, which is attached to a spectrometer. The

spectrometer disperses the light into spectral components and images the signal on a charged coupled device (CCD), where the incident photons create electron-hole pairs, which are converted by an analog-digital converter to analog-digital-units (ADUs) as a function of their respective wavelength. Principally, this setup configuration is quite basic, however, thanks to fast-evolving technological developments especially in the field of high-intensity laser sources, low-loss optical fibers, high-quality lens manufacturing and coating, and high-resolution spectrometers and detectors, modern Raman microscopic setups nowadays are much more powerful and mainly limited by the noise level and unspecific background scattering. The aforementioned basic configuration can be combined with a microscopic optical modality to form a confocal microscopic Raman system, which allows the users to observe a microscopic bright-field image of the sample with adapted FOV. However, this kind of instrumentation is quite large and rigid, not suitable for measurement conditions with only small working-space or even remote-controlled facilities, i.e. endoscopic and handheld measurement systems. For that, fiber-optical Raman probes are applied to overcome these issues.

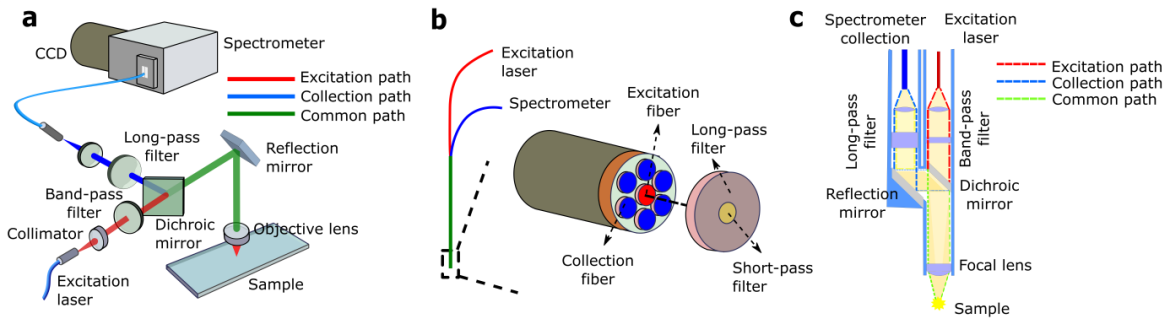

Figure 1.2 Typical Raman instrumentations: Conventional Raman microscope (a); A six plus one Raman endoscopic fiber probe with micro-filters located at the tip (b); A handheld fiber-optic Raman probe with a coaxial, dual-channel configuration.

The fiber optical probes combine the advantages of guiding the light, for both excitation and collection channel, and integrating all essential optical components on the fiber itself or into small-size housings [2,21,22]. Two representative Raman probe designs, such as a miniaturized probe and a handheld probe are shown in Figure 1.2 (b) and (c), respectively. Figure 1.2 (b) shows an example of an N+1 Raman probe containing N multi-channel collection fibers and one excitation fiber. Here N is 6 and can be readily increased, while also leads to a significant increase in the difficulty of manufacturing. The excitation light is scattered elastically and inelastically in all directions, thus a higher number of collection fibers typically translates into higher signal intensity. In this configuration, the laser light is coupled into the

excitation fiber and passes through a short-pass filter, which is coated on the center of the probe tip to get rid of the silica background. The long-pass filter coated in a ring-shaped fashion onto the collection fibers can reject the elastically scattered light. The collected Raman signal is coupled into a spectrometer for further spectral analysis. This type of miniaturized endoscopic probes offers a high advantage with its small size, of which the diameter can be miniaturized to sub-millimeter dimensions and adapted to endoscopic applications. Yet, it is also very obvious that the radiated laser beam is divergent at the fiber exit. The low numerical aperture (NA) of the fibers results in a low collection efficiency, which can be partly circumvented by increasing the number of collection fibers or integrating lenses on the fiber tip. Figure 1.2(c) shows a handheld Raman probe with miniaturized optical components integrated into a handheld housing. This probe design allows to freely access measurement sites on most surfaces, and therefore, can be an ideal tool for the clinical applications diagnosis and differentiation of healthy and diseased tissue during routine examination or surgery. Thanks to the employment of an objective lens, the laser radiation is focused on the sample, increasing the energy density of excitation. Additionally, the sufficiently high NA of the lens also promises higher collection efficiency compared to the miniaturized fiber probes. The flexibility of this type of handheld probes comes at a price, i.e. the focal distance changes and the inability to acquire images since the signal is generated from a single point. This dissertation is focusing on how to overcome these drawbacks.

1.4 Aim of the work

Considering all information above, the goal of this work is to overcome the comprehensive disadvantages when applying handheld Raman probes for clinical applications, i.e. the disadvantages of proper focusing, single-point measurements, and direct visualization.

The first part of the work aims at the development of an autofocus unit to overcome the problems occurring with fixed focus lenses. A new fiber-optical Raman probe design and implementation with an integrated liquid lens is presented. Compared with typically fixed focus probes, this probe can achieve fast focus adjustment and significantly stabilize the signal. Chapter 3.1 provides the design consideration and experimental verification of the in-house build probe with an autofocus function operating in handheld operation. The design of the probe

is based on coaxial dual optical paths, which deliver the excitation light and acquire Raman signals through a voltage-driven liquid lens. Thanks to stable and fast focus adjustments, the combination of the liquid lens and the built-in auto-focus algorithm can minimize the impact of distance changes during handheld operation. This method has a high potential for drug characterization and clinical *in vivo* applications and can be further extended to any other spectroscopic methods that require light to be focused on the sample.

The second part of the work presents a solution to the single point measurement issue of fiber probes by implementing a computer vision-based positional tracking of the laser focus. The proposed approach is based on a scanning procedure by moving the probe above the sample by hand, simultaneously assessing positional information of the probe, and acquiring and processing the spectroscopic data in real-time. This way Raman images from the biological sample can be reconstructed live in a short time. The chemical information can be evaluated and co-register for each position to demonstrate the biochemical distribution on the sample surface. This method allows easily to distinguish borders of different biomolecular composition and can be extended to clinical applications of tumor margin delineation.

In the third part, the direct visualization of the measurements recorded with the developed Raman probe imaging system is performed in an augmented and mixed reality. The Raman imaging system is based on the combination of Raman spectral measurements with simultaneous positional registration. This allows forming the biochemical augmented reality image by overlaying the Raman image on the visual image of the sample. The results are then displayed on a computer screen. Furthermore, with the help of a laser projector, the mixed reality can be directly shown on the physical position and observed by the naked-eye by live back-projecting the Raman image onto the sample. By applying the proposed approach, direct access to patients for diagnosing and distinguishing diseased from the healthy tissue is given by visualizing the results both on the computer screen and in the physical location. This approach especially can be extended as a potential image-guided instrument for disease diagnostics and surgical resection.

In the fourth part, the designed Raman imaging system is further improved by implementing the photometric stereo method for 3D reconstruction to visualize the Raman image in a 3D view scenario. This method offers users a more intuitive way to view the distribution of the chemical information on the surface in a 3D scenario compared to the

conventional 2D image. This also provides extended possibilities and the huge advantage of joint registration of Raman images with 3D reconstruction modalities such as CT, OCT, and MRI to strengthen the diagnosis.

2. Methods

2.1 Liquid lens-based autofocus algorithm

Conventional lenses are made from transparent materials such as glass and plastic, through polishing or molding to the desired shape. A light beam is focused or dispersed through refraction, which is determined by the shape of the lens and the resulting path length difference. To acquire higher Raman scattering signals it is, on the one hand, important to increase the local energy density of the laser beam on the sample, and on the other hand, to efficiently collect the generated signal. Considering a typical Raman setup, the focal plane is imaged on the entrance slit of the spectrometer, while ensuring that the NAs are matched. This also requires that the sample is positioned exactly in the focus, because otherwise the image of the focal plane on the entrance slit will be large and the coupling will be inefficient, i.e. the signal will be proportionally reduced. Normally, lenses have a fixed focal length since they are made from solid materials, making the focal adjustment not straightforward. There are, however, other, non-solid materials, which can be used for lenses. For example, liquid material can be used to create a lens, e.g. water droplet, which can magnify the surface it is deposited on. A new type of lenses, liquid lenses, can use the shape-changing property of liquids to rapidly change the curvature of a lens, and as such, the focal length. Those lenses are based on a physical phenomenon known as electrowetting. The effect refers to the wettability of a droplet on a substrate, which can be changed by applying an external voltage between the droplet and the insulating substrate leading to the deformation of the droplet curvature, and enabling a rapid adjustment of the focal distance [23,24] as shown in Fig. 2.1. The liquid lenses have been readily used for various applications, such as photographic cameras [25,26], microscopy [27], dual-beam laser autofocus [28], adaptive eyeglasses [29], optical coherence tomography angiography [30], and optical sectioning tomography [31]. Also, a liquid lens-based

commercial Raman spectrometer has been made available recently [32,33]. In contrast to probes made of conventional lens material requiring to maintain a certain probe-to-sample distance to achieve in-focus measurements, liquid lenses have variable focal length, which allows for a flexible working range. With the help of an autofocus algorithm applied to the liquid lens, the focal lengths can be dynamically adjusted to fit with the probe-to-sample distances.

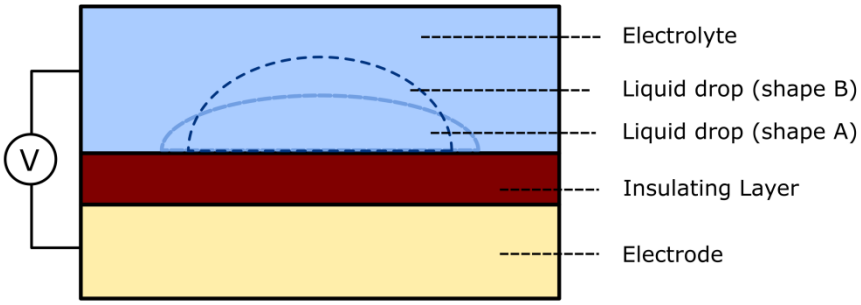

Figure 2.1 Schematic diagrams of the liquid lens. An insulating and non-polar liquid is deposited on the bottom wall, which is made of insulating and transparent material. Various voltages applied on the electrolyte layer and electrode layer lead to the deformation of the droplet curvature, for instance, from shape A to Shape B, resulting in changes in the focal length of the liquid lens.

The autofocus algorithm follows the auto-control theory, which deals with dynamic systems in the engineering processes. Fundamentally, there are mainly two types of control loops: closed-loop (feedback) control and open-loop control [34]. The difference between them is whether the control parameter is internal or external. Fig. 2.2 displays a flowchart of how both methods can be implemented for autofocusing purposes using liquid lenses as an objective lens for Raman probes. The closed-loop control is based on the feedback regarding the Raman signal intensity, i.e. according to the iterative changes in signal intensity the control voltages of the liquid lens are adjusted for optimal intensity. The open-loop control is based on the information of an external distance sensor. According to the readouts from the distance sensor, the voltages for controlling the liquid lens are similarly adjusted to the desired focal length. In principle, the closed-loop method is more advantageous because it does not require additional hardware to be implemented for the autofocus process. Since the external sensor in open-loop control may introduce extra measurement errors into the system, closed-loop routines often achieve control with higher accuracies. The main disadvantage is that it requires multiple acquisitions (between 8 to 12 times [35]) to find the correct voltage for the liquid lens according to the iterative feedback. This is especially challenging for low-light implementations, such as

Raman spectroscopy, which may significantly delay the measurement procedure. Using the open-loop method, the distance measurement is independent of the Raman signal acquisition so that the focal length of the liquid lens can be associated with the correct focal position through a look-up table (LUT). This can be done because there is a linear relationship between the focusing power vs. voltage response. Therefore, the entire process can be faster, but at the cost of increasing complexity. Since Raman spectroscopy is an application with very low signal intensity, only open-loop implementation seems to be possible. However, since the open-loop method alone can lead to a certain loss of accuracy, a combined method can be used for a fast and precise autofocusing method, which applies open-loop control for the coarse search and closed-loop control for the fine adjustment. This method has been performed and experimentally evaluated in [**WY1**] and detailed explanations are provided in Chapter 3.1.

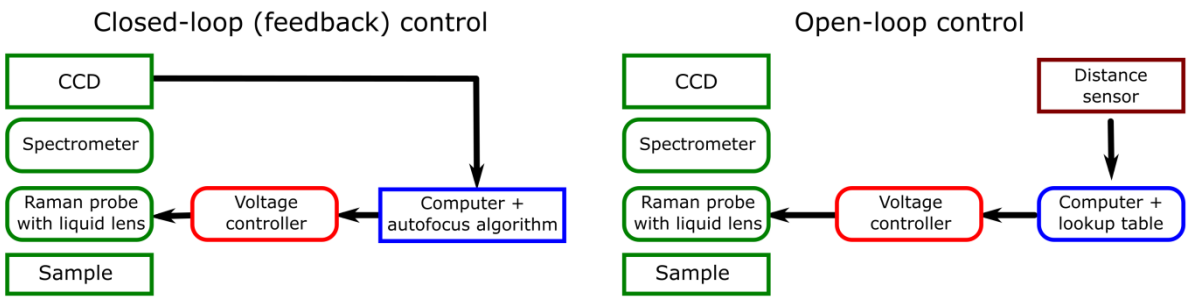

Figure 2.2 Diagrams of two autofocus control loops: Closed-loop control (left) where the control is based on the internal feedback signal, i.e. the Raman intensity; and open-loop control (right) where the control is based on the signal from the external sensor, i.e. distance sensor.

2.2 Positional tracking of the laser spot

The use of handheld probes for *in vivo* and surgical applications requires efficient methods for realizing mapping or scanning procedures. Besides, the acquired Raman information also lacks a co-registering method with the position where the measurement has been performed. To solve these problems, the computer-vision based positional tracking method can be applied, which has been reported to face a similar situation of Fluorescence Lifetime Imaging measurements (FLIm) [36]. In this study, a blue laser was applied as an aiming beam for tracking, since the conventional brightfield camera cannot detect the excitation laser for FLIm, which is in the ultraviolet (UV) region. According to Eq. (1-4), shorter wavelengths, i.e. visible and ultraviolet excitation laser, can achieve higher-intensity Raman scattering, however, it can also induce significant fluorescence that interferes with the Raman

signals. For biomedical related Raman measurements, it is advisable to use excitation wavelengths in the near-infrared, such as 785 nm laser as the excitation source, to achieve a compromise between the fluorescence background and the Raman signal intensity. So for Raman measurements with a handheld probe, the diffuse reflection and Rayleigh scattering of the excitation laser spot on the sample is visible and can be directly used as a tracker with no need for the additional aiming beam. The computer-vision based positional tracking relates to image processing techniques on the captured images of conventional brightfield camera which can, on one hand, co-register the Raman information with the positions of measurements in the image plane, on the other hand, can achieve mapping or scanning procedure by loop-operating the point-measurements. Different methods of image processing have been investigated for detecting and tracking the laser spot, such as color segment, threshold value, pattern recognition or modified circular Hough transform [37,38]. Here, a color-segment and threshold-based method was selected for the final implementation. The algorithm of this method is shown in Figure 1.4. First of all, a conventional RGB brightfield image is captured, which is a 32-bits 2D image, containing four 8-bits channels, i.e. red, green, blue, and alpha, as shown in Figure 2.3 (a). The laser spot contains the red and higher intensity pixels than the surrounding, that a segment of the red plane is applied to the brightfield image (Figure 2.3b) and a threshold is applied on the red plane to keep the higher intensity pixels, i.e. the remaining laser spot, resulting in a binary image (Figure 2.3c). To determine the central position and shape of the excitation spot, the contour of the spot is extracted first by using a Laplacian filter, which extracts neighboring pixels with significant variations of intensities. The Laplacian 3×3 convolution kernel is defined as:

$$\begin{matrix} a & d & c \\ b & x & b \\ c & d & a \end{matrix}$$

For this filter function the relation x = 2*(|a|+|b|+|c|+|d|) produces a contour of the focal spot. At last, an ellipse fitting function is applied to the extracted contour to figure out the corresponding ellipse as shown in Figure 2.3 (d).

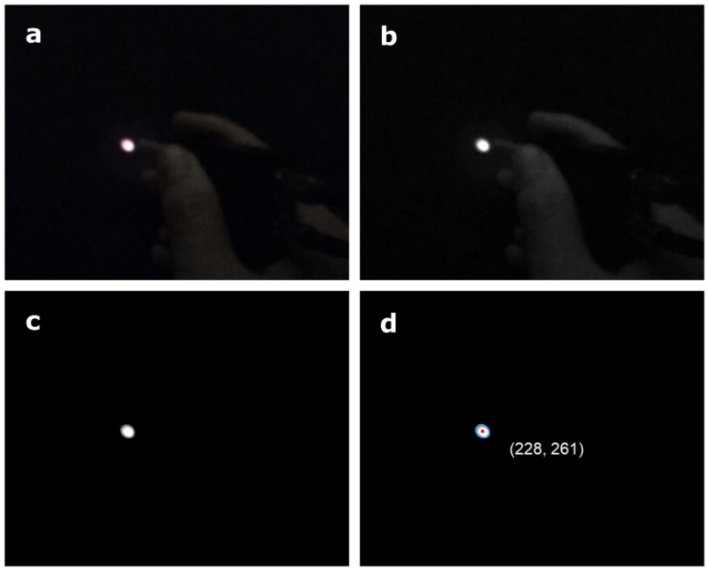

Figure 2.3 Diagrams of positional tracking algorithm of the laser spot. The images of conventional brightfield image (a), the eight-bit image of the extracted red plane from the brightfield image (b), after the application of a threshold, only high-intensity part, i.e. the laser spot(c), and image with overlaid center information based on an ellipse fitting (d).

By using this positional tracking algorithm of the laser spot, one can easily extract the necessary parameters, i.e. center, angle, major radius, and minor radius of the laser spot. Then, the scanning or mapping procedure can be achieved by loop-running the image capture and processing for each frame when moving the probe above the sample, which further can be integrated with real-time Raman spectroscopic data analysis to enable synchronized Raman image reconstruction. The reconstructed Raman image allows easily to co-register with the brightfield image for further steps of visualization. This method has been performed in [**WY2, WY3**] and detailed explanations are provided in Chapter 3.2.

2.3 Data processing algorithm for Raman spectra

The biomedical information can be extracted from the spectral Raman data by various methods. The easiest and most straightforward way is based on Raman intensities of some certain bands, which can be used to represent the chemical components. However, Raman intensities of bands can be influenced by a couple of factors, such as intensity loss because of out-of-focus measurement or broad background fluorescence. Another method that can be used for extracting Raman information is based on curve fitting [39]. Typically, with prior knowledge of the experimental dataset, i.e. pure spectra from the individual chemical components of the

sample, a least-squares fitting method enables online analysis of the acquired spectrum. The percentile amount for each of these components can be derived and assigned to the actual measurement point in the Raman image[40]. Then, each measured spectrum was preprocessed with asymmetrically least-squares baseline correction and normalization [41] and least-squares fitted using the molecular signatures from the database. Then, to visualize the concentration, each acquired spectrum is assigned an RGB color, representing the relative contribution of the different chemical components. Furthermore, multivariate data analysis methods using chemometric tools, such as generic principal component analysis (PCA), and various cluster analysis algorithms like K-means, hierarchical cluster analysis (HCA) can be used for extracting the Raman information without the need for prior knowledge of what is present within the sample, resulting in higher quality Raman images [42–45]. However, it is only feasible for the off-line procedure since these methods require the use of all data points of the Raman image. Since the aim of this thesis is to focus on flexible *in-vivo* clinical applications, the least-squares fitting method was selected.

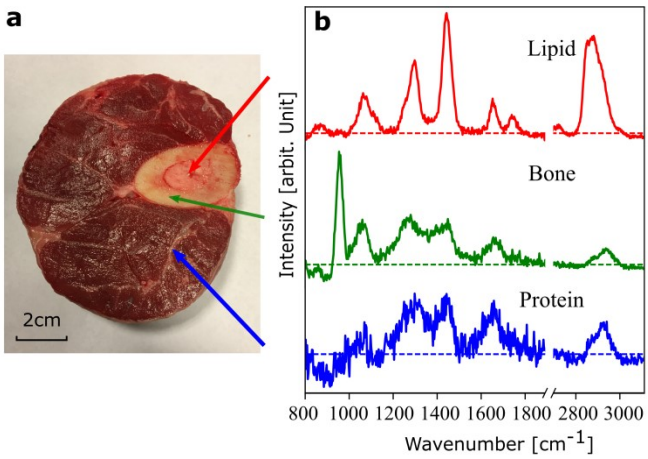

Figure 2.4 Photography of a proposed sample, a beef steak with a bone (a). And the mean spectra of the main chemical contributions of the sample, lipid, bone, and protein (b). Adapted from Figrue 3 in **[WY2]** with permission.

One example of the least-squares fitting method is shown in section 2.3 of **[WY2]**, with a bio-sample with components of lipid, bone, and protein. To realize real-time evaluation of chemicals, data processing procedures are executed in real-time during the data acquisition process. First, a series of data preprocessing steps are applied: wavelength calibration, intensity calibration, offset voltage offset correction, normalization, and baseline correction [41,46–48]. Then, to visualize the distribution of specific macromolecules in the sample, spectra from

relevant macromolecules present in biological samples were acquired, i.e. lipid, bone, and protein in Fig. 2.4(a), and the spectra of these three macromolecules are shown in Fig 2.4(b). To determine the relative macromolecule at a specific location of the sample, each measured spectrum was processed by least-squares fitting to the molecular signatures of interest from the database[40]. According to the least-squares fitting results, i.e. the relative contribution of the different chemical components, and combining with the positional information, intensity image planes which are related to the concentration of each component can be reconstructed. To visualize the information each image plane is assigned an RGB color, representing. The final Raman image is formed by merging the various intensity planes. Here, the RGB color was assigned as red for lipid, green for bone, and blue for protein.

2.4 Augmented reality and mixed reality

With the help of the detection and tracking of the laser spot, a dynamic link between the reconstructed Raman image and the brightfield image is created, which provides the possibility to build an augmented reality scenario. This yields a very high potential for image-guided instrumentation in disease diagnostics and surgical resection. For better visualization of Raman images for *in vivo* clinical applications, augmented reality and mixed reality approaches probably are ideal tools to display the Raman information, which can be significant add-on features for improving and supplementing real-time diagnosis or surgery [49–52]. Augmented reality technology provides users with an interactive experience with computer-generated perception information on a computer screen or through glasses to augment objects in the real world. Especially for clinical applications, image-based instrumentation combined with augmented reality can be a powerful tool to combine, i.e. the biochemical information of Raman spectroscopy with the visual inspection of the patient, improving real-time diagnosis or surgery [49]. Various imaging modalities have already been combined with augmented reality to provide the surgeon with additional information based on the respective optical advantages. Such techniques are computed tomography (CT) [53], optical coherence tomography (OCT) [54], magnetic resonance imaging (MRI) [55,56], optoacoustic imaging [57], fluorescence lifetime imaging [36,58], and ultrasound imaging [59,60]. The implementation of fiber optic-based Raman imaging with augmented reality has the advantage that it allows to obtain and analyze comprehensive biochemical information, which most of the other techniques cannot or only provide limited information of. Hence, a direct interpretation by real-time superimposing

the Raman image during the probe scanning procedure onto the brightfield image to detect and determine locations of unhealthy parts can be achieved. The visualization of augmented reality normally is on a computer screen or tablet. However, it can also be extended to a projector-based augmented reality, or so-called mixed reality, by back-projecting the Raman image directly onto the sample, which allows observing the chemical information with the naked eye. Since the Raman image is reconstructed on the same dimensional space as the brightfield image, the implementation of augmented reality can be directly realized by overlaying the Raman image onto the brightfield image. For visualizing a mixed reality scenario, the projector has to be pre-aligned with the brightfield camera. Since the height of the sample is much smaller than the distance between the projector and the workbench, and Raman information have approximately the same distance, it allows to approximately treat the surface of the workbench as the sample plane. The projecting plane of the projector can therefore be linked with the image plane of the camera by a homographic relationship, which can be built by using a coordinate checkerboard [61–63] as shown in Figure 2.5. After pre-calibration, the reconstructed Raman image can be transformed into the projecting plane, and by that overlaid with the original sample to form the mixed reality scenario. Detailed explanation and evaluation of the pre-calibration procedure is presented in the Supplementary information in **[WY3]**. Furthermore, this kind of visualization can be updated in real-time during the measurement procedure including an on-line spectral data processing. The augmented reality method has been demonstrated in [**WY2],** and together with mixed reality method has been applied in **[WY3**]. The detailed explanations and results are provided in Chapter 3.3.

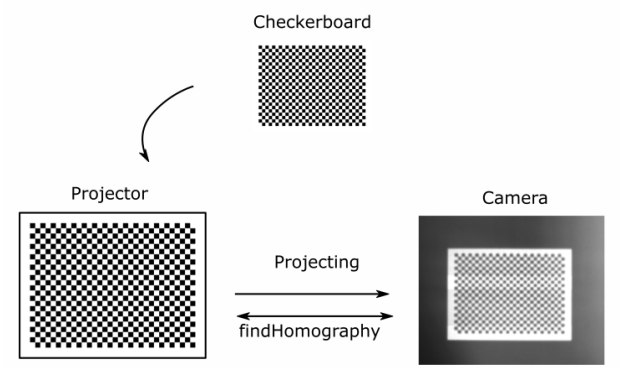

Figure 2.5 Flowchart of the projector-camera calibration: a checkerboard image is projected onto the workbench and captured by the brightfield camera. The homographic relationship is constructed by comparing the corresponding corner positions on individual images.

2.5 3D reconstruction

Conventional Raman imaging is performed on the surface of the sample in a 2D-focal plane, and accordingly, the results are displayed as 2D images. However, in many clinical applications, the sample has a 3D structure, and integrating 3D reconstruction methods with Raman imaging has obvious advantages because it represents the distribution of macromolecules on uneven sample surfaces more naturally. 3D reconstruction methods can be roughly divided into two categories: active methods or passive methods. The active methods have to actively interfere with the object, either mechanically or radiometrically. CT and MRI are representative examples for medical imaging applications, which use X-ray and strong magnetic fields, respectively, to acquire volumetric pixels (or voxels) of the measured sample, including its internal structure. The Lidar (light detection and ranging)-based approach is another example of an active method, which illuminates the target with laser light and measures the reflection with a sensor [64]. Structured-light is also a well-known approach of an active method, which illuminates the sample with specially designed 2D patterns, and analyses the distortion of the back-projected structured-light pattern to reconstruct the 3D surface image [65,66]. Contrarily, passive methods do not require interference with objects, and usually, cameras are applied to acquire a set of conventional images or videos to extract topological information. Computer stereo vision is one representative approach of passive methods, which is based on two displaced horizontal cameras acquiring two differing views on the sample inspired by the biological binocular vision [67]. The 3D information can be extracted from the disparity map by comparing these two images. The other representative approach is the photometric stereo technique, which estimates the depth and surface orientation of the targeted image from multiple images originating from the same viewpoint under different illumination directions [68–70].

Considering the convenience of combining Raman imaging with 3D reconstruction, especially to co-register a 2D Raman image of a 3D sample model, the photometric stereo method has been selected and integrated into the instrumentation as shown in **[WY3]**. Here, a four source photometric stereo approach [71,72] is applied, which allows acquiring four 2D images under four different illumination orientations from the top, right, bottom, and left. For an image of a Lambertian object with varying reflectivity (albedo) and assuming no self-

occlusion, the intensity value of the same pixel from these four 2D images, I_n, is determined by the following formula [73]:

$$\boldsymbol{I_n} = k(\boldsymbol{L_n} \cdot \boldsymbol{N}) \tag{2-1}$$

Here, N is the surface normal; k is the albedo and L_n is the coordinate of the four different illuminations. With the standard least-squares error procedure, $k\boldsymbol{N} = (\boldsymbol{L_n^T L_n})^{-1}\boldsymbol{L_n^T I_n}$, the normal $\boldsymbol{N}$ becomes a unit vector and albedo k can be estimated as the length of this vector. Furthermore, with the known coordinate of the four illumination sources and acquiring four 2D images, the surface normal of each pixel can be calculated. The gradient of each pixel can be estimated as following:

$$G_{x,y} = (\frac{N_x}{N_z}, \frac{N_y}{N_z}) \tag{2-2}$$

And taking a known start point (normally setting the height point manually) into the gradient map, the surface height image, i.e. the reconstructed 3D surface image, can be iteratively calculated. Because the same camera is used for the brightfield image, the positional tracking, and the 3D reconstruction, the Raman image has the same dimensional space as the fundamental plane of the reconstructed 3D model. This allows a straightforward way to project the Raman image onto the 3-dimensional sample surface and hence offering a Raman image with height information providing a better understanding of the distribution of the biochemical information. Further detailed explanation and evaluation of the photometric stereo procedure have been shown as the Supplementary information in **[WY3]**. Chapter 3.4 provides the results of combining Raman imaging and photometric stereo measurements of biological samples.

3. Results

In this chapter, an overview of the investigations, approaches, and experimental studies dealing with the main open research issues when applying handheld Raman probes for clinical applications is presented. The scientific significances of each topic are illustrated separately within the following subchapters.

3.1 Fiber-optic Raman probe with an integrated autofocus unit

Since a handheld fiber-optical Raman probe has the advantages of small size and easy access to the patient to acquire Raman spectroscopic information, it is an ideal and highly potential tool for clinical applications. However, a conventional probe has an objective lens with a fixed focal length, which requires the user to continuously maintain a predefined working distance. Otherwise, the acquired signal will be reduced significantly. To address this problem, a novel Raman probe was designed, which uses a liquid lens is the objective lens. The diagram of the in-house build Raman probe with an integrated liquid lens as the objective lens is shown as Fig. 3.1 (Fig.1 in **[WY1])**. The main part of the probe is similar to the conventional handheld probe which has a coaxial, dual-channel configuration. The excitation laser light is guided by one channel, where a bandpass filter removes the Raman signal from the fiber, i.e. the silica background, and gets focused on the sample by the liquid lens (C-S-25H0-096-03; Corning Varioptic Lenses, Lyon, France [74]). The liquid lens is connected through a flexible printed circuit (FPC) cable to a power source (USB-M Flexiboard, Corning Varioptic Lenses, Lyon, France), which is software-controlled through a USB cable to a computer, delivering a 1 kHz alternating current (AC) voltage to drive the liquid lens. The Raman signal is generated at the focal spot and collected by the liquid lens. The backscattered light is reflected by a dichroic mirror into the second channel where a long-pass filter gets rid of the Rayleigh scattering signal and then guided to the spectrometer. The key requirement for applying the Raman probe with the integrated liquid lens is how to adjust the applied voltage to the liquid lens to change the focal distance so that it correlates to the real probe-to-sample distance. As stated in chapter 2.1, a suitable autofocus algorithm has to be developed to enable the automatic adjustment of the

applied voltage without human intervention. Taking both speed and accuracy of the focus adjustment into account, a hybrid method is feasible to be applied here i.e. open-loop method for coarse search and closed-loop method for fine adjustment.

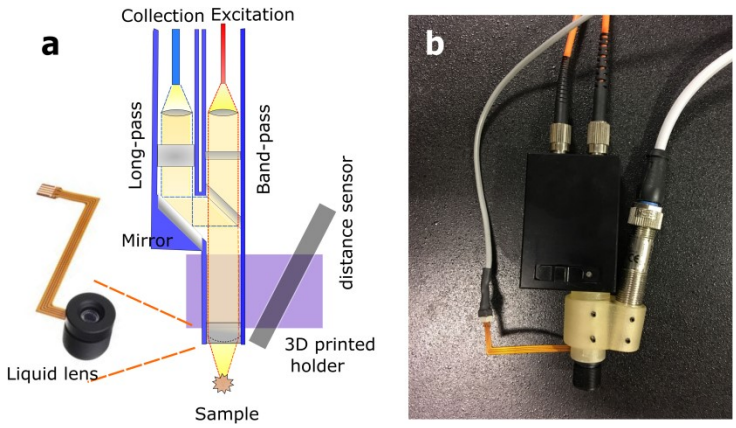

Figure 3.1 Diagram (a) and photograph (b) of the in-house build Raman probe with an integrated liquid lens as the objective lens. The attached distance sensor is fixed by a 3D-printed holder to maintain a defined relation for the realization of the autofocus function. Adapted from Figure 1 in **[WY1]** with permission.

The open-loop method is mainly based on the feedback of distance measurements. Various technologies have been applied for distance measurements, such as time-of-flight, triangulation, or ultrasound which are based on calculating the reflection of light or sound waves. Considering the speed, working range, and the possibility of combining it with a Raman probe, an ultrasonic distance sensor (UM12-1172271; SICK, Germany) is selected which is small in size, pen-like, voltage-driven and has a response time of 30 ms. The ultrasound measurement is independent of the Raman spectroscopic measurement since there is no mutual conflict between laser light and ultrasonic waves. Fig 3.1 demonstrates the Raman probe integrated with the ultrasonic sensor by mounting them on a 3D-printed holder. The sensor requires a 10 V driven-voltage, while the readout is also in voltage format so that a multifunction I/O device (USB6001; National Instruments, Austin, Texas) is applied for both delivering the driven-voltage and receiving the voltage-readout. To develop the algorithm, a functional relationship between the distance readout of the ultrasonic sensor and the correctly applied voltage to the liquid lens, a look-up-table had to be established through an initial calibration. The focal length f of the liquid lens is equal to the reciprocal of the dioptric power D, which itself is linear to the driving voltage U_L in the optical power [23,24]:

$$f = \frac{1}{D} = \frac{1}{a_1 \cdot U_L + b_1} \tag{3-1}$$

Here a_1 and b_1 are constants for the equation. For the ultrasonic sensor, there is a linear relationship between the voltage-readout U_S and the real distance d_S, a_2 and b_2 are the constants:

$$d_S = a_2 \cdot U_S + b_2 \tag{3-2}$$

Furthermore, as shown in Fig.2 in **[WY1]**, there is always a trigonometric function between the focal length f and the measured distance d_S of the distance sensor as following:

$$f = cos\alpha \cdot d_s - d_0 \tag{3-3}$$

α and d_0 is the angle and vertical distance between the lens with the distance sensor, respectively. These are constant once the liquid lens and ultrasonic sensor are fixed with the holder. Combining these equations, the relationship between U_L and U_S can be established as follows:

$$U_L = \frac{1}{cos\alpha a_1 a_2 \cdot U_S + cos\alpha a_1 b_2 - a_1 d_0} - \frac{b_1}{a_1} \tag{3-4}$$

Then, by combining the constants and simplifying the equation, the mathematical formula for the probe autofocus is as following:

$$U_L = \frac{1}{a \cdot U_S + b} + c \tag{3-5}$$

Thus, compared to the complex measurements of constants, such as α, d_0, d_s or establishing the relationship between f and U_L, the relation between U_L and U_S can be built by fitting the mathematical formula to data points acquired from changing the probe-to-sample distance step by step while recording the voltages of the distance sensor, and the best-driven voltages according to the highest Raman signal intensities. Fig.3 (b) in **[WY1]** plots the recorded data of the voltage readout of the distance sensor vs. the related best-driven voltage for the liquid lens (green dots) as well as the calculated curve fit (blue dashed curve) based on the mathematical formula. With the help of the calibrated fitting results, the driven-voltage U_L can be calculated from the distance readout U_S for each measurement.

During the calibration process, when the distance from the probe to the sample is gradually changed, there is a step of finding the corresponding optimal driven-voltage for the highest intensity of the Raman signal under the condition of a specific voltage of the distance sensor. Surely, this step can be achieved by manually adjusting the driven-voltage to find the moment of highest Raman intensity. However, for higher accuracy and minimal manual operation, the closed-loop method can be applied based on iterative feedback of the differences in the Raman signals at each step. For having defined U_S values, the Raman probe is placed on

a z-translational stage. Fig. 3.2 shows the flowchart of this closed-loop method, which contains the following steps:

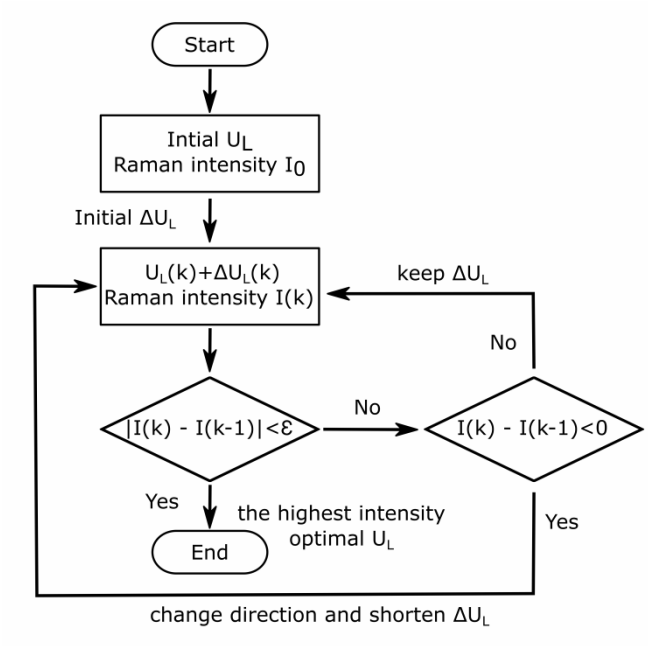

Figure 3.2 Flowchart of the closed-loop method. In briefly, the iterative signal, i.e. the highest intensity of the acquired spectrum or the intensity of a specific Raman band, is compared to a previous value: if the signal is increasing the algorithm changes the voltage continuous in the same direction; if the signal is decreasing the algorithm changes the voltage to the opposite direction and shorten the change step. Until the change of the signal maintains in a pre-defined threshold, the algorithm stops.

(a) Give an initial driven-voltage U_L to the liquid lens (such as 45 V since the range of driven-voltage is from 25 V to 70 V), either the highest intensity of the acquired spectrum or the intensity of a specific band is recorded as the initial Raman intensity (I_0);

(b) Increase the driven-voltage step by step and either measure the highest intensity of the acquired spectrum or the intensity of the specific band;

(c) Compare the current Raman intensity (I_k) to the pre-frame one (I_{k-1}), if $I(k) - I(k-1) > 0$, continue turning the driven-voltage up if $I(k) - I(k-1) < 0$, change and decrease the driven-voltage;

(d) When the turning direction changes, shorten the turning step according to the desired precision;

(e) Repeat steps (c) and (d) until $|I(k) - I(k-1)| < \varepsilon$ where ε is the pre-defined threshold.

Fig.3 (a) in **[WY1]** shows a representative procedure to determine the best driven-voltage to the liquid lens for U_S = 0.24 V. The closed-loop procedure is repeated for different probe-to-sample distances, and a relationship between the distance sensor and the liquid lens can be calibrated. Furthermore, this closed-loop method is also applied for the fine search of the autofocus procedure afterward. Based on the combined open-loop and closed-loop method, the probe allows fast, dynamic, and accurate adjustment of the focal length, while the probe is moved over the sample and a simultaneous Raman signal is acquired.

To evaluate the autofocus function of the presented Raman probe, a comparative experiment between using the autofocus function and a fixed focal length was carried out. The probe was fixed on the manual z-translational stage, the probe-to-sample distance was changed over a range of 4 mm and simultaneously Raman spectra were recorded. The detailed information of this comparative experiment can be found in section 3.2 in **[WY1]**. The experiment proves that the autofocus function can greatly reduce the loss of the Raman signal caused by defocusing effects when using the fixed focal length. The improvement will also vary depending on the distance from the probe to the sample, and for the current implementation, the improvement can be as high as 10-fold. The experimental features show that the reported Raman probe with the liquid lens has z-axis working range of ~2.8 mm to 6.4 mm instead of a fixed working distance, and can effectively compensate for signal reduction related to the distance. The current working range is limited by the maximum adjustability of the liquid lens, which can be improved by custom-designed liquid lenses optimized for the specific application. With the autofocus function, the probe can dynamically adjust the focal length to adapt to the distance from the lens to the sample, thereby guaranteeing a clear and discernible Raman spectrum.

Since the motivation of developing the autofocus probe aims to improve the handheld operation, further experimental evaluations were performed by comparing the measurements with the fixed length and autofocus function under handheld conditions. The acquisition time was set to 0.5 s and due to rapid hand movement, only the open-loop method was applied for the adjustment of the focus. Section 3.3 in **[WY1]** describes the information of this comparative experiment. In a similar range of probe-to-sample change, a ~12-fold reduction of the collected signal with the fixed-length was observed by comparing the Raman intensities varying during the measurement, while with the autofocusing probe only a ~2.2-fold reduction. It can be seen that while the variation of the distances is comparable, the standard deviation of the acquired

Raman spectra is significantly reduced by using the autofocus algorithm. Besides, since the effect of response time becomes more obvious as the acquisition time decreases, measurements for acquisition times of 0.1 s and 1 s were also performed. For shorter acquisition times, it is more challenging to adjust the voltage-based distance change than for longer acquisition times. The reason is the speed limitation caused by the open-loop method, which is about 45 ms and close to the acquisition time of 100 ms. As soon as hand movement occurs during the acquisition process, the liquid lens may delay the adjustment of the focal length, resulting in more significant Raman intensity changes. For longer acquisition time, the delay of the liquid lens response is not obvious, and it has no significant effect on the intensity, so the intensity is more stable. Nevertheless, the stability is still higher than during measurements with fixed focal length, which can be seen by comparing the experimental results between the fixed focal length and the autofocus function (Fig. 5 and Fig. 6, **[WY1]**).

Last but not least, the developed probe has been applied for Raman imaging, which also compares the experimental results between the autofocus algorithm and the fixed focal length. The imaging experiments were performed on a biological sample, which was placed titled at 15° on an X-Y motor scanning stage (MLS203-1, Thorlabs, Newton, New Jersey). The net z-directional displacement from one side to the other was approx. 1.8 mm and the Raman imaging was based on the intensity mapping of the Raman band at 1459 cm^{-1}. The results are shown in Fig.7 in **[WY1]**. As expected, for the situation with fixed focal length, due to the tilt of the sample and the resulting change in the probe-to-sample distance, a significant intensity change can be observed in the x-dimension of the image. Since the tilt is only on the x-axis, there is no obvious intensity change on the y-axis. The experiment was repeated using the autofocus algorithm in the same position, including the closed-loop method because the probe was fixed and not used in handheld operation. The liquid lens using the auto-focus method can eliminate the mismatch between the probe-to-sample distance and the focal length, thereby almost completely corrects the effect of the tilt. However, it should be pointed out that the limitation of the implemented ultrasonic distance sensor is a flat surface of at least 3 mm^2 to reflect the ultrasonic waves to the detector, so that the probe with an open-loop method or hybrid method can be used on samples, including liquid or powder samples. On the other hand, the closed-loop algorithm is not limited to measurements of uneven surfaces. However, it may limit the autofocus process for measurements, where very fast sampling is needed. However, modifications to the ultrasonic sensor (allowing for improved focusing capabilities) can

significantly increase the resolution and range of applications. Furthermore, the proposed method can be extended for many other optical modalities that need to focus light on the sample, such as FLIM, second harmonic generation (SHG) imaging, and coherent anti-Stokes Raman Scattering (CARS).

3.2 Fiber-optic Raman probe imaging system based on computer-vision tracking

Using a handheld fiber-optic Raman probe in a free-hands approach allows easy and flexible access to the site of interest during surgery or diagnostics. Because of uncontrolled hand or patient movement, the correct co-registration between the measurement site and the collected Raman spectrum is challenging, and the acquisition of Raman images not possible. This, however, significantly reduces the opportunities for using Raman spectroscopy for in vivo molecular margin differentiation. One possibility to improve this is by using a mechanical arm, which could be used to register the information, but this significantly increases the complexity and reduces the flexibility of the approach. A more elegant solution is based on laser spot tracking and accurate detection of a laser spot through real-time image processing of a video stream from a brightfield camera. The latter approach was implemented in the theses. With the help of positional tracking, the Raman imaging procedure can be realized by continuously assessing the positional information of the laser spot and synchronously acquiring Raman information from the same location. Also, sparse sampling, i.e. incomplete characterization of the region of interest, can be avoided by laser spot tracking. The position information is obtained from the bright field images, which are taken simultaneously with the Raman spectra. Color segmentation and thresholding are applied to extract the laser position. The positional information can be extracted from the conventional RBG images which are captured during the Raman measurement by color segment and threshold as described in chapter 2.2. Meanwhile, the biomedical information can be extracted from the spectral Raman data by the least-squares fitting method as described in chapter 2.3.

Knowing the laser position, i.e. the measurement site, and the composition of the measured sample, the Raman image can be reconstructed and visualized. For each spectrum, a circle is generated and shown on top of the bright field image. In **[WY2]**, the diameter of the reconstructed circles is a fixed parameter. Depending on the speed of the fiber probe movement a fixed diameter causes a sparse or a blurred image, respectively. To avoid this, a modification

was implemented in **[WY3].** The diameters of the circles are no longer fixed but are adapted to the speed of movement of the Raman probe. In details, the scalable diameter d of the circle is determined by the minor radius (r) of the fitted ellipse and the Euclidian distance D between the center of the currently fitted ellipse and the one from the previous frame according to the following rules:

$$d = \begin{cases} 0.5r, & if\ D < r \\ r, & if\ r \leq D < 2r \\ 2r, & else \end{cases} \tag{3-6}$$

This compromise between the speed of the probe movement during the measurement and the size of the reconstruction circle serves to improve image reconstruction as compared to **[WY2]**. Then, by assigning intensity planes of the known components to various basic colors, these planes can be combined to reconstruct the Raman image. Also, **[WY3]** combined with the producer/consumer queue function, the reconstruction of Raman images runs in parallel with Raman measurements and position tracking. Compared with the sequential execution in **[WY2]** of the two steps, higher efficiency and processing speed can be obtained.

The fiber-optic Raman probe imaging system was implemented based on the approaches mentioned above. The spatial resolution of the presented Raman imaging is an important parameter and has been theoretically analyzed and experimentally evaluated. Theoretically, the spatial resolution is determined by a comparison between the size of the laser spot and the spatial resolution of the brightfield camera, which provides the positional information of the laser spot. For the measurements, the resolution of the brightfield camera is set as 640 × 512 pixels with a field of view of around 15.6 cm × 12.5 cm in **[WY3]** (320 × 240 pixels for about 15 × 12 cm in **[WY2]**). This results in a spatial resolution of around 0.24 mm per pixel. The diameter of the output laser spot is around 0.1 mm as the excitation fiber, with a core diameter of 105 µm, is imaged 1:1 into the sample plane. Taking the spatial resolution of the brightfield camera and the size of the laser spot into account, the theoretic spatial resolution of the whole system is around 0.24 mm per pixel. Using a high-resolution brightfield camera and a smaller laser spot can improve the spatial resolution. This, of course, increases the acquisition time for Raman images of the same size. The current parameters are a trade-off between the time taken for full coverage scanning and the appropriate image quality. Additionally, the reconstruction in each frame of the Raman imaging is based on the scalable circle of which diameter is determined by the minor radius of the fitted ellipse as mentioned in chapter 2.2. To perform

this adjustment, at least five points are required [79], i.e. the laser spot, like the reconstructed circle, must have a diameter of at least 2 pixels, and the reconstruction requires minimal ±1 pixel surrounding the center position to draw the constructed circle, so that the resolution would be around 0.5 mm per reconstructed circle. For experimental evaluation, a spatial resolution target of various width stripes was designed and in-house fabricated by 3D printing as shown in Fig. 6 of **[WY3]**. The width of the strips varies from 0.5 mm to 5 mm. The main body part of the target is made of Poly (methyl methacrylate) (PMMA), while the grooves between the strips are filled with moldable thermoplastic for gaps >1 mm and powdery paracetamol for gaps ≤1 mm, respectively. The proposed Raman imaging method was performed, using PMMA, thermoplastic and paracetamol as reference spectra. Assigning different LUT colors to these three intensity-image planes, i.e. red for PMMA, green for plastic, and blue for paracetamol, allows reconstructing a 24-bit pseudo-color Raman image as shown in Fig. 6e of **[WY3]**. It can be seen from the results that the experimental spatial resolution is consistent with the theoretical analysis, and the size of each pixel in the reconstructed plane is about 0.24 mm and the constructed circle has a size of at least around 0.5mm. This parameter is suitable for the scene of the image-guided instrument for clinical applications and can be adjusted as needed to meet the experimental requirements.

Based on the proposed fiber-optic Raman probe imaging system, measurements have been performed on different kinds of bio-sample. In **[WY2]**, a beef steak with bone was selected as the sample which contains multiple structured components, i.e. bone, lipid, and protein-rich structures, Fig 3.3(a_1). The used bright field camera was set to 320 ×240 pixels and a frame rate of 24 fps. The power of the excitation laser was set to 100 mW at the sample and the spectral acquisition time to 50 ms to enable a near video-rate acquisition. Within 6 min. of scanning, including positional tracking of the laser spot and spectral analysis, it is possible to sample a large part of the biological tissue, Fig 3.3(a_2). The color-coded reconstructed Raman image consisted of 640 points. With the set resolution of the bright field camera and the field of view of approximately 15 cm × 12 cm in the sample plane, the resulting spatial resolution was 0.47 mm. Due to the low-speed processing of the sequential execution, a low camera resolution was selected to cover a large enough area in a reasonable time. As the first implementation of the presented approach, in **[WY2],** it is possible to distinguish between different components during the data acquisition process, resulting in a real-time assessment of the macromolecular

distribution of the sample, offering a great potential to visually distinguish non-differentiable samples based on their molecular profile.

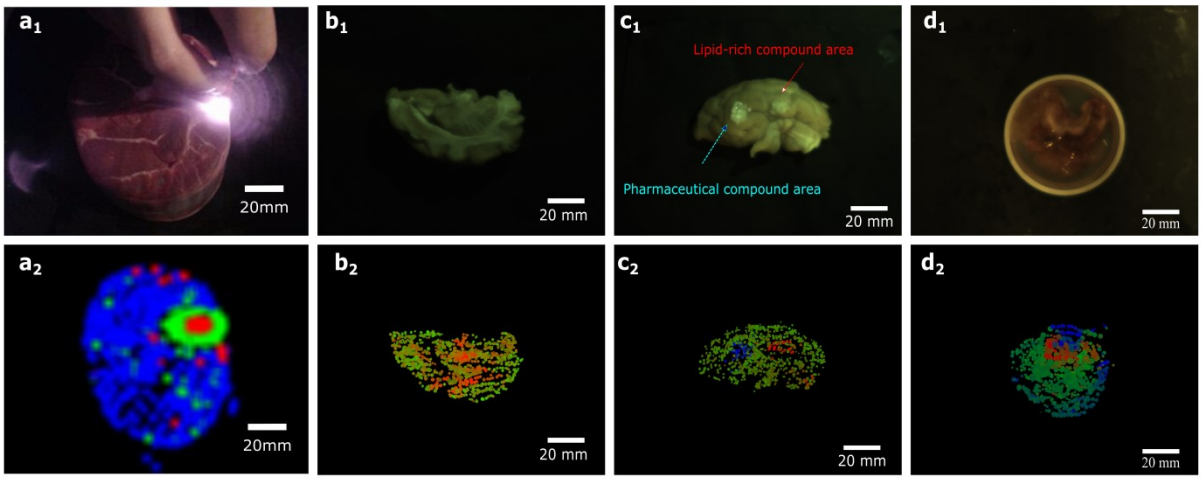

Figure 3.3 Representative results of brightfield images and Raman images of different samples, Beef sample(a_1,a_2), exposed porcine brain sample (b_1, b_2), porcine cerebrum sample model with two simulate areas (c_1, c_2), and clinical biopsy sample (d_1,d_2), respectively. Adapted from **[WY2]** and **[WY3]** with permission.

In **[WY3]**, a complementary metal-oxide-semiconductor (CMOS) camera (DCC1645C; Thorlabs, Austin, Texas) replaced the conventional webcam as it has a 650 nm short-pass filter to decrease the influence of the reflection of too bright Rayleigh scattering, which may make the detection area larger than the actual one. The processing speed was also improved by using a parallel data processing algorithm. To demonstrate the developed proposed approach, it has been applied to further bio-samples. First of all, to demonstrate the principle performance of the reported approach on a sample with a flat surface, a porcine cerebrum brain was selected and cut horizontally to reveal the structured components, i.e. white matter and grey matter, and had a size around 7.3 cm × 3.7 cm, Fig 3.3(b_1). A pre-processing step built the known database of white matter and grey matter. During 210 s of handheld probe scanning of the sample 987 points were acquired, resulting in full coverage of the Raman image, and the separation of the molecule contributions of interest according to the pre-built reference spectra could be shown, Fig 3.3(b_2). With the help of parallel data analysis, an almost triple speed of data processing has been achieved by comparing the current speed rate of 4.7 Hz with the previous measurement of 1.8Hz. And with the improved spatial resolution, results in a decrease in the size of the pixel and an obvious improvement of the fineness of the Raman image. Another experiment has been performed on a porcine cerebrum with a size around of 7 cm × 4 cm × 2.6 cm to measure the 3D structure of the cerebral cortex to demonstrate the combination of the proposed Raman

imaging approach with optical 3D reconstruction method, which will be explained in details in chapter 3.4. Here, the focus is the Raman imaging part. Because the surface of the brain mainly only contains gray matter, a model was created to increase the chemical difference and to simulate two cases, i.e. tumor presence, which was realized by locally applying a lipid-rich compound, and local presence of medication, which was realized by locally applying a pharmaceutical compound, Fig 3.3(c_1). In 260 s 856 Raman measurements of the brain surface with the three chemical compounds, i.e. the white matter, lipid, and pharmaceutical, were performed, Fig 3.3(c_2). The reconstructed data shows that the proposed approach allows to dynamically distinguish the components by their specific Raman information and demonstrate the distribution of these components with various colors on the image plane. More importantly, to demonstrate the performance of the reported approach for clinical applications, the proposed approach has been applied on two *ex vivo* biopsy samples with the help of the cooperated partners in University Clinic Jena. One experiment was performed on a sample resected from a tumor surgery with a size of 5.2 cm× 4.1 cm, Fig 3.3(d_1). In general, in about 184 s with 994 points, nearly full coverage and distributed Raman image was constructed which shown three various biochemical components on the sample, Fig 3.3(d_2). The other experiment was performed on a sample, which was resected from surgery for extensive intramuscular lipoma in the area of the pectoralis major muscle of a 68-year-old patient with a size of 4 cm × 2.8 cm, as shown in the supplementary information of **[WY3]**. In about 160 s with 672 points, the Raman image of this biopsy was constructed. However, since the sample was resected from the intramuscular lipoma, only lipid spectrum has been detected, that no biomedical difference was found. Although measurements aim to detect tumor from the healthy tissue, the samples we got were the center parts of the suspected tissue, and the border parts which may have healthy tissue need to be histologically studied for the concern of patients so that no difference between tumor and healthy tissue can be detected. Based on the performed experiments, one can see that the proposed approach has wide applicability, and is not restricted to a specific organ or tissue, which has broad potentials as image-guided instrumentation for clinical applications.

3.3 Raman imaging in combination with augmented and mixed chemical reality

Besides the advantage of the convenient movement of applying the handheld Raman probe to achieve Raman imaging procedure, as mentioned in chapter 2.3 the reconstructed Raman image

allows being applied further to combine with the brightfield image to form the augmented chemical reality and to combine with the original sample through back-projecting to form the mixed chemical reality. Figure 3.4 indicates the schematic diagrams of the realization of augmented chemical and mixed chemical reality, respectively.

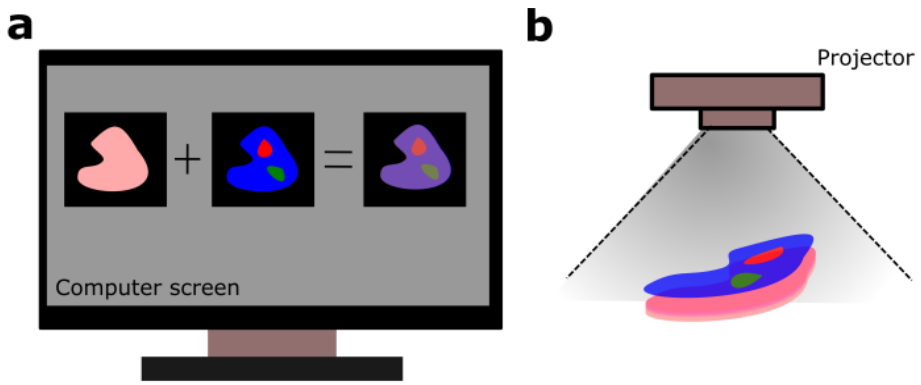

Figure 3.4 Schematic diagrams of the realization of augmented chemical reality (a) and mixed chemical reality(b): the augmented reality is realized by overlaying the Raman image yielded from the handheld Raman probe based instruction with the brightfield image captured by the camera, which can be observed on the computer screen; the mixed reality is realized by real-time projecting the Raman image on the original sample surface with help of a laser projector, which can be observed by naked eyes.

As Figure 3.4 (a) shows, since the Raman image has the same dimensional space as the brightfield image, the augmented reality is realized by merging the images. Furthermore, because the proposed Raman imaging approach is reconstructed as point-by-point in real-time, the augmented reality is also live updated with the measurement running point-by-point. Combining the Raman imaging with the static brightfield image allows dynamically displaying the augmented chemical information, which offers a real-time assessment of the macromolecular distribution of the sample and a further positional link between the Raman image and the brightfield image. The Raman image of the sample of beefsteak was shown in the augmented reality scenario in **[WY2]**. More measurements have been performed in **[WY3]**, not only demonstrating the advantages of augmented chemical reality but also have performed mixed chemical reality by real-time projecting the Raman image on the original sample surface with help of the laser projector. After the image calibration by building the homographic relationship between the brightfield camera and the projector, it allows projecting the Raman image fit on the original sample surface for demonstrating the macromolecular distribution of the sample, which can be easily observed by users with naked- eyes, Figure 3.4 (b). Augmented reality and mixed reality have been performed on the flat surface exposed brain sample, the

brain sample model with 3D structure, and two *ex vivo* biopsy samples, Fig. 3.5. Detailed information about the results can be found in Figure 1 and Figure 2 in **[WY3]** and Figure S3 in Supplementary Information. Each measurement has been separately recorded by video and can be found as the supplementary videos in the supplementary information. From these results, the proposed Raman imaging approach based on the handheld Raman probe allows to visualize the Raman image results of various kinds of samples in augmented reality and mixed reality manner, dynamically and directly providing the biochemical distribution of on the sample surface, and can be linked with the original positions where the point-measurements have been performed. This kind of visualizations further underlines the proposed approach has significant potential as image-guided instrumentation for *in vivo* imaging.

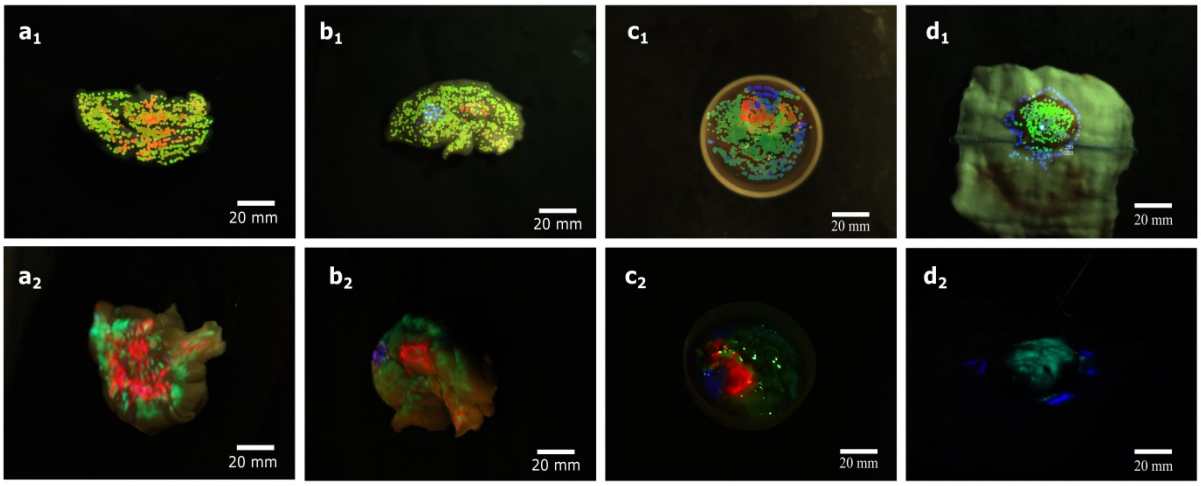

Figure 3.5 Representative results of augmented Raman reality and mixed Raman reality of different samples, The exposed brain sample (a_1, a_2), brain sample model with two simulate areas (b_1, b_2), and two clinical biopsy samples (c_1, c_2, d_1, and d_2), respectively. Adapted from **[WY3]** with permission.

3.4 Raman imaging in combination with 3D reconstruction

Raman spectroscopy can acquire information from different depths and allows for reconstructing a three-dimensional (3D) confocal Raman image for very small samples, such as single eukaryotic cells or small ploy particles [75–77] due to the low penetration depth of laser light in the visible range in tissue, Raman scattering has very low probability to occur in the deep layers of the sample (below 100 micrometers of the surface) [78]. For conventional Raman measurements, the height information of the sample usually is ignored, and Raman imaging is realized in a 2D plane. It would also be attractive and interesting to combine the Raman information with height information, i.e. a 3D representation of the sample, which not

only shows the distribution of macromolecules on the surface but also adds the height information of the sample. To achieve this aim, a 3D reconstruction method based on photometric stereo has been selected and integrated into the instrumentation.

First of all, an evaluated measurement of the photometric stereo method was applied on a hemisphere phantom which has a diameter of 25 mm and was designed and fabricated by 3D printing, as shown in Figure 3.6(a). It has slices of every 20° from the center on the horizontal plane and vertical plane, respectively. After acquiring conventional images under different illuminated directions, results of the untextured 3D scene and textured 3D scene of different view from the top, front, and side, respectively are shown as Fig. 3.6 (b). Fig. 3.6 (c) indicates the height maps of the reconstructed, real, and the absolute difference between the reconstructed and real, respectively. The real height map is plotted according to the equation: $\mathbf{z} = \sqrt{\boldsymbol{r}^2 - (\boldsymbol{x} - \mathbf{320})^2 - (\boldsymbol{y} - \mathbf{256})^2 + \boldsymbol{b}}$, here r = 104, (25 mm÷ 0.24 mm/pixel) is the radius of the hemisphere, (320, 256) is the center of the image and b = 8.3 (2 mm) in the lower part of the phantom. The root-mean-square error (RMSE) between reconstructed and real is ~3.7 pixels (0.9 mm) and the normalized root-mean-square error (NRMSE) is 3.3%. This error may come from various factors, i.e. the different illumination power of the LEDs, the accuracy of the equipment assembly, and the quality of the camera (image distortion). Nevertheless, this scale of error is acceptable for the current implementation. Then, the reconstructed 3D model was applied to combine with the reported Raman imaging method, which allows to map the molecular information on the 3D-surface, forming an augmented reality image, Fig. 4c in **[WY3].**

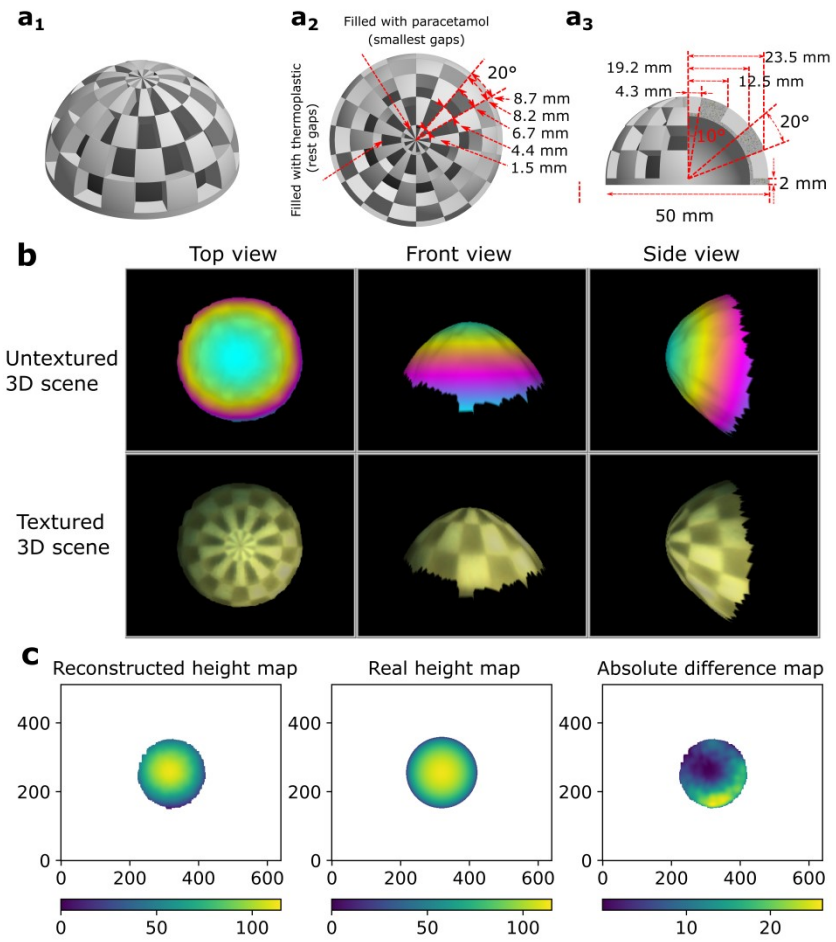

Figure 3.6 Diagram of the hemisphere phantom, which has slices of every 20° from the center on the horizontal plane and vertical plane, respectively, and the spaced area on the surface is excavated and refilled with paracetamol (smallest gaps), and moldable thermoplastic (rest gaps) (a_1). Top-view of the phantom, which shows the arc lengths of a 20° slice on each horizontal level (a_2). Three-quarter side-view of the phantom, which shows the radiuses of each horizontal level. (a_3) The reconstructed image under untextured 3D scene and textured 3D scene with a different view from the top, front, and side, respectively (b). The height maps of the reconstructed, real, and the absolute difference between the reconstructed and real (c). Adapted from **[WY3]** with permission.

Furthermore, to demonstrate the visualization of Raman image combining with the photometric stereo method, experimental measurement has been performed on porcine cerebrum with the 3D structure in **[WY3]**. As shown in Fig. 3.7(a and b), the non-textured height image and the textured image with the original color image of the brain sample was reconstructed using the method of the photometric stereo system, which is based on the analysis of the images of the sample under different light orientations. Additionally, since the same brightfield camera is applied for both the photometric stereo and the positional tracking step for Raman imaging, it allows mapping the Raman image on the reconstructed height 3D image that

users can observe the chemical distribution of the surface from the sample in a 3D Raman information textured scenario as predicted in Fig. 3.7(c). A related 3D scene view video of the structured sample in individual windows of non-textured height image, original color textured image, and Raman textured image is attached as Supplementary Video 1a in **[WY3]**.

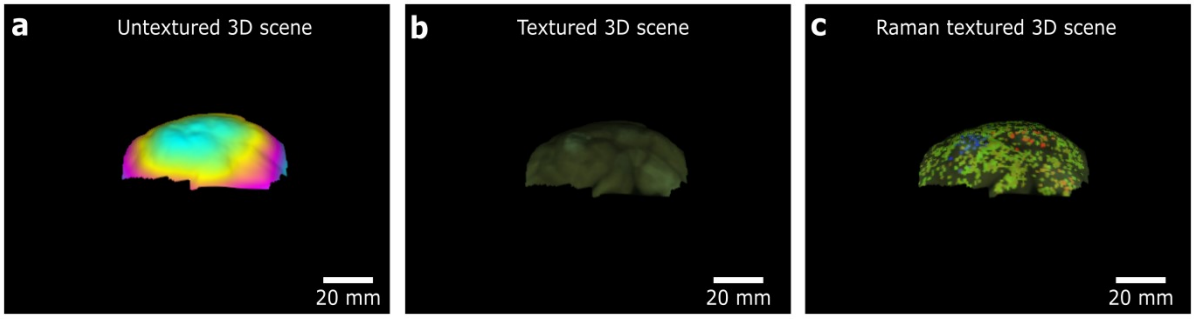

Figure 3.7 Representative results of applying the photometric stereo method on the brain to get the untextured height 3D scene image (a) and textured 3D scene image with original colors (b). Coating the Raman image on the 3D reconstructed model to form the Raman textured 3D scene image (c). The color information represents different chemical components, i.e. red for the lipid-rich compound, green for protein, and blue for the pharmaceutical compound. Adapted from **[WY3]** with permission.

Here, the result shows the possibility of the Raman image combining with the photometric stereo method to show the Raman image results in a 3D view. More importantly, this visualization of Raman image in a 3D scenario has full potential to be extended to other 3D optical reconstruction methods or medical imaging methods, such as laser scanning, computer stereo vision, CT, OCT, and MRI for further clinical applications as a supplier for image-guided instrumentations.

4. Summary

Raman spectroscopy-based technologies have been emphasized to be translated into biomedical and clinical applications in recent years. Typically, Raman systems based on handheld fiber-optic probes are more feasible for these applications compared to the conventional microscopic Raman system, since the probe offers advantages in terms of smaller sizes and easier access to the measurement sites, making it more favorable for complex environments. However, there are also several common drawbacks of applying probes for many applications: (1) the focus issue stemming from a fixed working distance of the objective lens. Regular probes have a fixed focal length, which requires the user to maintain a certain working distance to acquire higher Raman signals, otherwise, the defocusing results in a significant loss in signal intensity. (2) The single-point-measurement issue arises from the fact that the probe can only acquire spectra from the focal spot of the excitation laser, which lacks efficient methods for realizing a mapping or scanning procedure. (3) Direct visualization of the Raman data in an intuitive and easily understandable way is hampered due to the lack of real-time data processing and a straightforward co-registering method to link the Raman information with the respective measurement position. These tasks were tackled in this thesis and the investigations reported are related to these main themes.

In the first part of this dissertation, a handheld fiber-optic Raman probe with an autofocus unit was presented to overcome the problem arising from using fixed-focus lenses, by using a liquid lens as the objective lens, which allows dynamical adjustment of the focal length of the probe, published in **[WY1]**. The reported approach is based on the liquid-lens implementation combined with a hybrid algorithm consisting of the open-loop and closed-loop method. The former is used for a coarse focus search by adjusting the focal length of the liquid lens according to the distance-readout of an ultrasonic distance sensor, whereas the latter is based on the iterative feedback of the acquired Raman intensity for fine search. To evaluate the performance of the probe with the autofocus unit, experiments have been performed on the acquisition of Raman spectra from a sample with and without autofocus algorithm by translating the probe via a z-directional stage continuously changing the probe-to-sample

distance. The results show that autofocusing allows acquiring Raman spectra without reduced distance-related signal intensities, whereas the experiment with a fixed focal distance probe resulted in significant signal loss. Additionally, to demonstrate the performance of the probe for handheld operation, experiments at different Raman acquisition times have been performed by operating the probe by hand in combination with the autofocus function or with a fixed focal length. The results demonstrate that under current experimental conditions the presented probe has a dynamic distance range of about 2.8 mm to 6.4 mm, and a response time of 45 ms, which can easily tolerate the instability of handheld operation. This reported work can significantly improve the performance of handheld Raman probes and enables the acquisition of spectra without reduced signals. Furthermore, this approach can be extended to other spectroscopy and microscopy modalities, such as FLIM, SHG, CARS, and others.

In the second part, to overcome the single-point-measurement matter of Raman fiber probes, an implementation of a computer vision-based positional tracking to co-register the regular Raman spectroscopic measurements with the spatial location has been proposed and experimentally demonstrated. This enables fast recording of a Raman image from a large tissue sample by combining positional tracking of the laser spot through brightfield images, with the simultaneous spectral acquisition and online processing to assess the chemical information. The performance of the proposed approach was experimentally evaluated on several biological and clinical samples, showing that a Raman image can be created using a handheld probe and molecular signatures can be discriminated. Presented in **[WY2],** a Raman image from a large biological tissue of 15 cm × 12 cm at a resolution of 3.76 mm can be acquired in only 6 min, with a spectral acquisition speed of 1.8 Hz. After optimizing the currently sequential data processing, the acquisition time can be even further reduced, which was demonstrated in **[WY3].** A producer/consumer queue function replaced the sequential process and significantly improved the processing speed which allows parallel data processing between collection and analysis. Experimental measurements were performed on different samples in **[WY3]** showing that the parallel data analysis and processing can achieve a speed rate of 4.7 Hz, about three times faster than in **[WY2]**. Furthermore, the spatial resolution was also improved, which has been theoretically analyzed and experimentally evaluated, indicating a resolution of 0.24 nm per point. The developed Raman imaging system satisfies the need for an image-guided method, which can be adjusted according to real requirements. The proposed method can contribute to bringing Raman spectroscopy into the clinical environment by offering the possibility for real-

time, online tissue characterization during surgery. Possible clinical applications are the diagnosis of diseased tissue and delineation of neoplasia from healthy tissue during surgery.

In the third and fourth part of this dissertation, the visualization of the Raman image has been extended to augmented and mixed reality and combined with a 3D reconstruction method to offer an intuitive and easily understandable way of presenting the Raman image. These methods have been demonstrated in **[WY3]**. By implementing the developed fiber-optic probe-based Raman imaging system, a Raman image can be easily positional co-registered with the measurement site, which allows to link and overlay the Raman image with the brightfield image and show it in an augmented reality scenario on the computer screen. With the help of a small-size laser-projector, the Raman image can be back-projected on the original sample in the physical world to present the Raman information in a mixed reality sense. These two methods can significantly improve the visualization of the Raman imaging results in an intuitive and easily understandable manner. Furthermore, the reconstructed Raman image can be combined with the 3D surface reconstruction method called photometric stereo. This allows projecting the Raman image on the actual 3D surface of the sample to demonstrate the molecular distribution and tissue boundaries in a 3D view. To demonstrate this direct visualization of a Raman image, *ex vivo* experiments have been performed on different samples to demonstrate various functions. The experimental results fully demonstrate the key features of the presented work, which enables fast recording of a Raman image based on a handheld Raman probe, live visualization of the Raman image in an augmented or mixed reality, as well as in a 3D view. Hereby, complex Raman signatures of biological macromolecules can be displayed incomprehensible ways. The proposed approach has significant and attractive potential value for the clinical environment as image-guided instrumentation for cancer diagnostics and surgical resection and also allows to be combined with current medical equipment, such as CT and MRI.

In conclusion, this thesis is an advance towards resolving the open concerns of applying handheld Raman probes for clinical applications as a potential image-guided tool. The presented work provides (1) development and evaluation of a Raman probe with an autofocus unit to overcome the focus issue of handheld probes; (2) a handheld probe-based Raman imaging method, which allows to co-register the acquired Raman spectrum with the spatial measurement positions to deal with the single-point-measurement drawback; (3) visualizing Raman images in direct and intuitive ways of augmented and mixed reality scenarios and

combining that with a 3D surface reconstruction method to display the complex Raman signatures of biological macromolecules. All these advances are substantial and highly beneficial to further drive the clinical translation of Raman spectroscopy as potential image-guided instrumentation.

5. Zusammenfassung

In den letzten Jahren wurde ein Augenmerk auf die Translation von Raman spektroskopischen Technologien für die biomedizinische und klinische Anwendungen gesetzt. Typischerweise sind Raman-Systeme, die auf tragbaren faseroptischen Sonden basieren, für diese Anwendungen im Vergleich zu herkömmlichen mikroskopischen Raman-Systemen praktikabler, da die Sonde Vorteile in Bezug auf ihre kleinere Größe aufzeigt und diese einen leichteren Zugang zu den Messstellen bietet, was für komplexe Umgebungen günstig ist. Es gibt jedoch auch einige typische Nachteile bei der Verwendung von Sonden für viele Anwendungen: (1) Das Fokusproblem ergibt sich aus einem festen Arbeitsabstand der Objektivlinse. Normale Sonden haben eine feste Brennweite, so dass der Benutzer einen bestimmten Arbeitsabstand einhalten muss, um höhere Raman-Signale zu erfassen. Andernfalls führt die Defokussierung zu einem signifikanten Verlust der spektralen Intensität. (2) Das Problem der Einzelpunktmessung ergibt sich aus der Tatsache, dass die Sonde nur Spektren vom Fokusspot des Anregungslasers erfassen kann und effiziente Methoden zur Realisierung eines Abbildungs- oder Abtastvorgangs fehlen. Zusammenfassend lässt sich sagen, dass die direkte Visualisierung der Raman-Daten auf intuitive und leicht verständliche Weise aufgrund des Fehlens einer Methode zur gemeinsamen Registrierung der Raman-Informationen mit der jeweiligen Messposition behindert wird. Diese Aufgaben wurden in der vorliegenden Arbeit behandelt und die publizierten und vorgestellten Untersuchungen beziehen sich auf diese Hauptthemen.

Im ersten Teil dieser Dissertation wurde eine handgehaltene faseroptische Raman-Sonde mit einer Autofokuseinheit vorgestellt, um das Fokusproblem zu überwinden, indem die Brennweite der Sonde unter Verwendung einer Flüssigkeitslinse als Objektivlinse dynamisch angepasst wird, was in **[WY1]** veröffentlicht wurde. Der berichtete Ansatz basiert auf der Implementierung von Flüssigkeitslinsen in Kombination mit einem Hybridalgorithmus, der aus der sogenannten Open-Loop- und der Closed-Loop-Methode besteht. Ersteres wird für eine Grobfokussuche verwendet, indem die Brennweite der Flüssigkeitslinse gemäß der Abstandsanzeige eines Ultraschall-Abstandssensors angepasst wird, während letzteres auf der

iterativen Rückkopplung der erfassten Raman-Intensität für die Feinsuche basiert. Um die Leistung der Sonde mit integrierter Autofokuseinheit zu bewerten, wurden Experimente zur Erfassung von Raman-Spektren einer Probe mit und ohne Autofokus-Algorithmus durchgeführt, indem die Sonde über einen z-veränderbaren Tisch verschoben wurde, wobei der Abstand von Sonde zu Probe kontinuierlich geändert wurde. Es zeigte sich deutlich, dass die Autofokussierung die Erfassung von Raman-Spektren ohne entfernungsbedingt verringerten Signalintensitäten ermöglicht, während das Experiment mit einer Sonde mit fester Brennweite zu einem signifikanten Signalverlust führte. Um die Leistung der Sonde für den Handbetrieb zu demonstrieren, wurden zusätzlich Experimente mit verschiedenen Raman-Aufnahmezeiten durchgeführt, indem die Sonde von Hand bewegt wurde und die Autofokusfunktion verwendet oder mit einer festen Brennweite gemessen wurde. Die Ergebnisse zeigen, dass die vorgestellte Sonde unter den gegenwärtigen Versuchsbedingungen einen dynamischen Abstandsbereich von etwa 2,8 mm bis 6,4 mm und eine Reaktionszeit von 45 ms aufweist, wodurch die Instabilität des Handbetriebs leicht kompensiert werden kann. Diese Arbeit kann die Anwendbarkeit von handgehaltenen Raman-Sonden erheblich verbessern und die Erfassung von Spektren ohne reduzierte Signale ermöglichen. Darüber hinaus kann dieser Ansatz auf andere Spektroskopie- und Mikroskopiemodalitäten wie FLIM, SHG, CARS und andere ausweitet werden.

Im zweiten Teil wurde zur Überwindung der Einzelpunktmessung von Raman-Fasersonden eine Implementierung einer computergestützten Positionsverfolgung vorgeschlagen und experimentell demonstriert, um die regulären Raman-spektroskopischen Messungen zusammen mit der Ortsinformation zu registrieren. Dies ermöglicht eine schnelle Aufzeichnung eines Raman-Bildes von einer großen Gewebeprobe, indem die Positionsverfolgung des Laserspots durch Hellfeldbilder mit der gleichzeitigen Erfassung und Verarbeitung von Raman-Spektren zur Bewertung der chemischen Informationen kombiniert wird. Die Leistung des vorgeschlagenen Ansatzes wurde experimentell an mehreren biologischen Proben bewertet, wobei gezeigt wurde, dass man mit einer Handsonde ein Raman-Bild erstellen und molekulare Signaturen unterschieden kann. In **[WY2]** wurde ein Raman-Bild aus einem großen biologischen Gewebe von 15 cm × 12 cm mit einer Auflösung von 3,76 mm in nur 6 Minuten mit einer spektralen Erfassungsgeschwindigkeit von 1,8 Hz aufgenommen. Nach einer Optimierung der derzeit sequentiellen Datenverarbeitung kann die Erfassungszeit noch weiter reduziert werden, was in **[WY3]** gezeigt wurde. Eine Producer / Consumer-

Warteschlangenfunktion ersetzte den sequentiellen Prozess und verbesserte die Verarbeitungsgeschwindigkeit erheblich, was eine parallele Datenverarbeitung zwischen Erfassung und Analyse ermöglicht. Experimentelle Messungen wurden an verschiedenen Proben in **[WY3]** durchgeführt, welche zeigten, dass die parallele Datenanalyse und -verarbeitung eine Geschwindigkeitsrate von 4,7 Hz erreichen kann, etwa dreimal schneller als in **[WY2]**. Darüber hinaus wurde auch die räumliche Auflösung, die theoretisch analysiert und experimentell bewertet wurde, auf 0,24 nm pro Punkt verbessert. Das entwickelte Raman-System erfüllt somit die Anforderung einer bildgebenden Methode, die an die tatsächlichen Anforderungen angepasst werden kann. Die vorgeschlagene Methode kann dazu beitragen, die Raman-Spektroskopie in die klinische Umgebung zu bringen, da sie die Verwendung während einer Operation in Echtzeit bietet. Mögliche klinische Anwendungen sind die Diagnose von erkranktem Gewebe und die Abgrenzung von Neoplasien von gesundem Gewebe während einer Operation.

Im dritten und vierten Teil dieser Dissertation wurde die Visualisierung des Raman-Bildes auf die erweiterte (engl. augmented) und gemischte Realität erweitert und mit einer 3D-Rekonstruktionsmethode kombiniert, um eine intuitive und leicht verständliche Darstellung des Raman-Bildes zu bieten. Diese Methoden wurden in **[WY3]** demonstriert. Durch die Implementierung des entwickelten Raman-Bildgebungssystems auf Basis einer faseroptischen Sonde kann ein Raman-Bild zusammen mit der realen Messposition aufgenommen werden, wobei das Raman-Bild mit dem Hellfeldbild verknüpft und überlagert und in einem Augmented-Reality-Szenario auf dem Computerbildschirm dargestellt werden kann. Mit Hilfe eines kleinen Projektors kann das Raman-Bild sogar auf das Originalmuster in der physischen Welt zurückprojiziert werden, um die Raman-Informationen in einem Mixed-Reality-Szenario darzustellen. Diese beiden Methoden können die Visualisierung der Raman-Bildgebungsergebnisse auf intuitive und leicht verständliche Weise erheblich verbessern. Darüber hinaus kann das rekonstruierte Raman-Bild mit dem als photometrisches Stereo bezeichneten 3D-Oberflächenrekonstruktionsverfahren kombiniert werden. Dies ermöglicht die Projektion des Raman-Bildes auf die tatsächliche 3D-Oberfläche der Probe, um die molekulare Verteilung und die Gewebegrenzen in einer 3D-Ansicht wiederzugeben. Um diese direkte Visualisierung eines Raman-Bildes zu demonstrieren, wurden *ex vivo*-Experimente an verschiedenen Proben durchgeführt, um verschiedene Funktionen zu zeigen. Die experimentellen Ergebnisse demonstrieren umfassend die Neuerungen der vorgestellten Arbeit,

die eine schnelle Aufzeichnung eines Raman-Bildes mit einer handgehaltenen Raman-Sonde, einer Live-Visualisierung des Raman-Bildes in einer erweiterten oder gemischten Realität sowie in einer 3D-Ansicht ermöglicht. Hierdurch können komplexe Raman-Signaturen biologischer Makromoleküle nachvollziehbar dargestellt werden. Der vorgeschlagene Ansatz hat ein signifikantes und attraktives Potenzial für klinische Einsätze als bildgesteuertes Instrument für die Krebsdiagnostik oder die chirurgische Resektion und ermöglicht auch die Kombination mit derzeitigen medizinischen Geräten wie CT und MRT.

Zusammenfassend ist die vorliegende Dissertation ein Fortschritt bei der Lösung der bisherigen Beeinträchtigungen bezüglich des Einsatzes tragbarer Raman-Sonden für die klinische Anwendungen als mögliches bildgesteuertes Werkzeug. Die vorgestellte Arbeit bietet: (1) die Entwicklung und Bewertung einer Raman-Sonde mit einer Autofokuseinheit, um das Fokusproblem von Hand gesteuerten Sonden zu überwinden; (2) ein handgehaltenes, Sonden-basiertes Raman-Bildgebungsverfahren, das ermöglicht, das erfasste Raman-Spektrum zusammen mit der räumlichen Messposition zu registrieren, um den Nachteil der Einzelpunktmessung zu beheben; (3) die Visualisieren von Raman-Bildern auf direkte und intuitive Weise in Augmented- und Mixed-Reality-Szenarien und das Kombinieren dieser mit einer 3D-Oberflächenrekonstruktionsmethode, um die komplexen Raman-Signaturen biologischer Makromoleküle anzuzeigen. All diese Fortschritte sind äußerst nützlich und von großer Bedeutung, um die klinische Translation der Raman-Spektroskopie als bildgesteuerte Instrumentierung weiter voranzutreiben.

6. Bibliography

1. M. Schmitt and J. Popp, "Raman spectroscopy at the beginning of the twenty-first century," J. Raman Spectrosc. **37**(1–3), 20–28 (2006).

2. E. Cordero, I. Latka, C. Matthäus, I. W. Schie, and J. Popp, "In-vivo Raman spectroscopy: from basics to applications," J. Biomed. Opt. **23**(07), 1 (2018).

3. B. Han, W. Xu, Z. Yu, Y. Du, C. Zheng, G. Zhao, P. Gao, and Z. Fan, "The Clinical Application of Raman Spectroscopy for Breast Cancer Detection," J. Spectrosc. **2017**(1), 1–10 (2017).

4. M. Jermyn, J. Desroches, K. Aubertin, K. St-Arnaud, W. J. Madore, E. De Montigny, M. C. Guiot, D. Trudel, B. C. Wilson, K. Petrecca, and F. Leblond, "A review of Raman spectroscopy advances with an emphasis on clinical translation challenges in oncology," Phys. Med. Biol. **61**(23), R370–R400 (2016).

5. W. Wang, J. Zhao, M. Short, and H. Zeng, "Real-time in vivo cancer diagnosis using raman spectroscopy," J. Biophotonics **8**(7), 527–545 (2015).

6. L. A. Austin, S. Osseiran, and C. L. Evans, "Raman technologies in cancer diagnostics," Analyst **141**(2), 476–503 (2016).

7. Cm. Krishna and S. Rubina, "Raman spectroscopy in cervical cancers: An update," J. Cancer Res. Ther. **11**(1), 10 (2015).

8. J. W. Tunnell, M. K. Markey, J. S. Reichenberg, K. R. Sebastian, J. Zhang, A. J. Moy, M. C. Fox, H. T. M. Nguyen, and X. Feng, "Raman active components of skin cancer," Biomed. Opt. Express **8**(6), 2835 (2017).

9. T. Liu, C. Chen, X. Shi, and C. Liu, "Evaluation of Raman spectra of human brain tumor tissue using the learning vector quantization neural network," Laser Phys. **26**(5), (2016).

10. S. Cui, S. Zhang, and S. Yue, "Raman Spectroscopy and Imaging for Cancer Diagnosis," J. Healthc. Eng. **2018**, 1–11 (2018).

11. T. Shaipanich, H. Zeng, H. C. McGregor, S. Lam, W. Wang, D. N. Ionescu, G. Chen, J. Zhao, M. A. Short, and A. McWilliams, " Real-time endoscopic Raman spectroscopy for in vivo early lung cancer detection ," J. Biophotonics **10**(1), 98–110 (2016).

12. O. Stevens, I. E. Iping Petterson, J. C. C. Day, and N. Stone, "Developing fibre optic Raman probes for applications in clinical spectroscopy," Chem. Soc. Rev. **45**(7), 1919–1934 (2016).

13. I. Pence and A. Mahadevan-Jansen, "Clinical instrumentation and applications of Raman spectroscopy," Chem. Soc. Rev. **45**(7), 1958–1979 (2016).

14. J. Wang, M. S. Bergholt, W. Zheng, and Z. Huang, "Development of a beveled fiber-optic confocal Raman probe for enhancing in vivo epithelial tissue Raman measurements at endoscopy," Opt. Lett. **38**(13), 2321 (2013).

15. "Integrated Raman Probe," https://www.ipslasers.com/integrated-Raman-probe.html.

16. L. A. Reisner, B. W. King, M. D. Klein, G. W. Auner, and A. K. Pandya, "A prototype biosensor-integrated image-guided surgery system," Int. J. Med. Robot. Comput. Assist. Surg. **3**(1), 82–88 (2007).

17. R. J. Lapeer, S. J. Jeffrey, J. T. Dao, G. G. García, M. Chen, S. M. Shickell, R. S. Rowland, and C. M. Philpott, "Using a passive coordinate measurement arm for motion tracking of a rigid endoscope for augmented-reality image-guided surgery," Int. J. Med. Robot. Comput. Assist. Surg. **10**(1), 65–77 (2014).

18. P. C. Ashok, M. E. Giardini, K. Dholakia, and W. Sibbett, "A Raman spectroscopy bio-sensor for tissue discrimination in surgical robotics," J. Biophotonics **7**(1–2), 103–109 (2014).

19. C. V. RAMAN and K. S. KRISHNAN, "A New Type of Secondary Radiation," Nature **121**(3048), 501–502 (1928).

20. R. L. McCreery, *Raman Spectroscopy for Chemical Analysis* (John Wiley & Sons, Inc., 2000).

21. I. Latka, S. Dochow, C. Krafft, B. Dietzek, and J. Popp, "Fiber optic probes for linear and nonlinear Raman applications - Current trends and future development," Laser Photonics Rev. **7**(5), 698–731 (2013).

22. C. Krafft, S. Dochow, I. Latka, B. Dietzek, and J. Popp, "Diagnosis and screening of cancer tissues by fiber-optic probe Raman spectroscopy," Biomed. Spectrosc. Imaging **1**(1), 39–55 (2012).

23. B. Berge and J. Peseux, "Variable focal lens controlled by an external voltage: An application of electrowetting," Eur. Phys. J. E **3**(2), 159–163 (2000).

24. B. Berge, "Liquid lens technology: principle of electrowetting based lenses and applications to imaging," in *18th IEEE International Conference on Micro Electro Mechanical Systems, 2005. MEMS 2005.* (IEEE, n.d.), pp. 227–230.

25. J. Fuentes-Fernández, S. Cuevas, L. C. Álvarez-Nuñez, and A. Watson, "Tests and evaluation of a variable focus liquid lens for curvature wavefront sensors in astronomy," Appl. Opt. **52**(30), 7256–7264 (2013).

26. S. Pasinetti, I. Bodini, M. Lancini, F. Docchio, and G. Sansoni, "Experimental characterization of an autofocus algorithm based on liquid lens objective for in-focus imaging in the macro range," in *Proceedings - 2017 7th International Workshop on Advances in Sensors and Interfaces, IWASI 2017* (IEEE, 2017), pp. 195–200.

27. M. Bathe-Peters, P. Annibale, and M. J. Lohse, "All-optical microscope autofocus based on an electrically tunable lens and a totally internally reflected IR laser," Opt. Express **26**(3), 2359 (2018).

28. F. Zhang, Y. Yao, X. Qu, T. Zhang, and B. Pei, "Dual-beam laser autofocusing system based on liquid lens," Opt. Laser Technol. **88**, 198–204 (2017).

29. N. Hasan, A. Banerjee, H. Kim, and C. H. Mastrangelo, "Tunable-focus lens for adaptive eyeglasses," Opt. Express **25**(2), 1221 (2017).

30. J. Yang, L. Liu, J. P. Campbell, D. Huang, and G. Liu, "Handheld optical coherence tomography angiography," Biomed. Opt. Express **8**(4), 2287 (2017).

31. C. Xu, W. Zhao, J. Hu, B. Zhang, and S. Wang, "Liquid lens-based optical sectioning tomography for three-dimensional flame temperature measurement," Fuel **196**, 550–563 (2017).

32. "THE FIRST IN THE INDUSTRY TO USE AN AUTOFOCUS SOLUTION IN A RAMAN SPECTROMETER," https://serstech.com/industry-first-autofocus-an-

interview-with-katja-szybek/.

33. K. Szybek and J. Sonnvik, "Raman spectroscopy system," U.S. patent US10295408B2 (2019).

34. K. Sharma, "Automation Strategies," in *Overview of Industrial Process Automation* (Elsevier, 2011), pp. 53–62.

35. "The product brochure of CorningVariopticLenses," https://www.corning.com/media/worldwide/Innovation/documents/FINAL_CorningVariopticLenses_productbrochure_5.4.18_lowresWEB.pdf.

36. D. Gorpas, D. Ma, J. Bec, D. R. Yankelevich, and L. Marcu, "Real-Time Visualization of Tissue Surface Biochemical Features Derived from Fluorescence Lifetime Measurements," IEEE Trans. Med. Imaging **35**(8), 1802–1811 (2016).

37. F. Chávez, F. Fernández, R. Alcalá, J. Alcalá-Fdez, G. Olague, and F. Herrera, "Hybrid laser pointer detection algorithm based on template matching and fuzzy rule-based systems for domotic control in real home environments," Appl. Intell. **36**(2), 407–423 (2012).

38. D. Krstinić, A. Skelin, and I. Milatić, "Laser Spot Tracking Based on Modified Circular Hough Transform and Motion Pattern Analysis," Sensors **14**(11), 20112–20133 (2014).

39. T. J. Vickers, R. E. Wambles, and C. K. Mann, "Curve Fitting and Linearity: Data Processing in Raman Spectroscopy," Appl. Spectrosc. **55**(4), 389–393 (2001).

40. I. W. Schie, L. Nolte, T. L. Pedersen, Z. Smith, J. Wu, I. Yahiatène, J. W. Newman, and T. Huser, "Direct comparison of fatty acid ratios in single cellular lipid droplets as determined by comparative Raman spectroscopy and gas chromatography," Analyst **138**(21), 6662 (2013).

41. S.-J. Baek, A. Park, Y.-J. Ahn, and J. Choo, "Baseline correction using asymmetrically reweighted penalized least squares smoothing," Analyst **140**(1), 250–257 (2015).

42. R. Gautam, S. Vanga, F. Ariese, and S. Umapathy, "Review of multidimensional data processing approaches for Raman and infrared spectroscopy," EPJ Tech. Instrum. **2**(1), 8 (2015).

43. O. A. Maslova, G. Guimbretière, M. R. Ammar, L. Desgranges, C. Jégou, A. Canizarès,

and P. Simon, "Raman imaging and principal component analysis-based data processing on uranium oxide ceramics," Mater. Charact. **129**, 260–269 (2017).

44. L. Zhang, M. J. Henson, and S. S. Sekulic, "Multivariate data analysis for Raman imaging of a model pharmaceutical tablet," Anal. Chim. Acta **545**(2), 262–278 (2005).

45. H. Shinzawa, K. Awa, W. Kanematsu, and Y. Ozaki, "Multivariate data analysis for Raman spectroscopic imaging," J. Raman Spectrosc. **40**(12), 1720–1725 (2009).

46. C. H. Tseng, J. F. Ford, C. K. Mann, and T. J. Vickers, "Wavelength calibration of a multichannel spectrometer," Appl. Spectrosc. **47**(11), 1808–1813 (1993).

47. M. Fryling, C. J. Frank, and R. L. Mccreery, "Intensity calibration and sensitivity comparisons for CCD/raman spectrometers," Appl. Spectrosc. **47**(12), 1965–1974 (1993).

48. P. H. C. Eilers, "A perfect smoother," Anal. Chem. **75**(14), 3631–3636 (2003).

49. S. Nicolau, L. Soler, D. Mutter, and J. Marescaux, "Augmented reality in laparoscopic surgical oncology," Surg. Oncol. **20**(3), 189–201 (2011).

50. S. Bernhardt, S. A. Nicolau, L. Soler, and C. Doignon, "The status of augmented reality in laparoscopic surgery as of 2016," Med. Image Anal. **37**, 66–90 (2017).

51. M. Kersten-Oertel, P. Jannin, and D. L. Collins, "The state of the art of visualization in mixed reality image guided surgery," Comput. Med. Imaging Graph. **37**(2), 98–112 (2013).

52. P. Vávra, J. Roman, P. Zonča, P. Ihnát, M. Němec, J. Kumar, N. Habib, and A. El-Gendi, "Recent Development of Augmented Reality in Surgery: A Review," J. Healthc. Eng. **2017**, 1–9 (2017).

53. P. Pratt, M. Ives, G. Lawton, J. Simmons, N. Radev, L. Spyropoulou, and D. Amiras, "Through the HoloLens^{TM} looking glass: augmented reality for extremity reconstruction surgery using 3D vascular models with perforating vessels," Eur. Radiol. Exp. **2**(1), 2 (2018).

54. D. Lee, C. Lee, S. Kim, Q. Zhou, J. Kim, and C. Kim, "In Vivo Near Infrared Virtual Intraoperative Surgical Photoacoustic Optical Coherence Tomography," Sci. Rep. **6**(1), 35176 (2016).

55. J. Morita, S. Shimamura, M. Kanegae, Y. Uema, M. Takahashi, M. Inami, T. Hayashida, and M. Sugimoto, "MRI overlay system using optical see-through for marking assistance," in *2015 IEEE Virtual Reality Conference, VR 2015 - Proceedings* (IEEE, 2015), pp. 239–240.

56. L. Besharati Tabrizi and M. Mahvash, "Augmented reality–guided neurosurgery: accuracy and intraoperative application of an image projection technique," J. Neurosurg. **123**(1), 206–211 (2015).

57. L. Lan, Y. Xia, R. Li, K. Liu, J. Mai, J. A. Medley, S. Obeng-Gyasi, L. K. Han, P. Wang, and J. X. Cheng, "A fiber optoacoustic guide with augmented reality for precision breast-conserving surgery article," Light Sci. Appl. **7**(1), (2018).

58. J. L. Lagarto, V. Shcheslavskiy, F. Saverio Pavone, and R. Cicchi, "Simultaneous fluorescence lifetime and Raman fiber-based mapping of tissues," Opt. Lett. **45**(8), 2247 (2020).

59. L. Yang, J. Wang, T. Ando, A. Kubota, H. Yamashita, I. Sakuma, T. Chiba, and E. Kobayashi, "Vision-based endoscope tracking for 3D ultrasound image-guided surgical navigation," Comput. Med. Imaging Graph. **40**, 205–216 (2015).

60. F. Mahmood, E. Mahmood, R. G. Dorfman, J. Mitchell, F. U. Mahmood, S. B. Jones, and R. Matyal, "Augmented Reality and Ultrasound Education: Initial Experience," J. Cardiothorac. Vasc. Anesth. **32**(3), 1363–1367 (2018).

61. Z. Zhang, "A flexible new technique for camera calibration," IEEE Trans. Pattern Anal. Mach. Intell. **22**(11), 1330–1334 (2000).

62. O. Chum, T. Pajdla, and P. Sturm, "The geometric error for homographies," Comput. Vis. Image Underst. **97**(1), 86–102 (2005).

63. D. Moreno and G. Taubin, "Simple, accurate, and robust projector-camera calibration," Proc. - 2nd Jt. 3DIM/3DPVT Conf. 3D Imaging, Model. Process. Vis. Transm. 3DIMPVT 2012 464–471 (2012).

64. J. Tachella, Y. Altmann, N. Mellado, A. McCarthy, R. Tobin, G. S. Buller, J.-Y. Tourneret, and S. McLaughlin, "Real-time 3D reconstruction from single-photon lidar data using plug-and-play point cloud denoisers," Nat. Commun. **10**(1), 4984 (2019).

65. J. Geng, "Structured-light 3D surface imaging: a tutorial," Adv. Opt. Photonics **3**(2), 128 (2011).

66. M. Gupta, A. Agrawal, A. Veeraraghavan, and S. G. Narasimhan, "Structured light 3D scanning in the presence of global illumination," in *CVPR 2011* (IEEE, 2011), pp. 713–720.

67. M. Faisal, H. Mathkour, M. Alsulaiman, and M. Zuair, "Multi-sensors multi-baseline mapping system for mobile robot using stereovision camera and laser-range device," Adv. Mech. Eng. **8**(6), 168781401665463 (2016).

68. Y. Sun, J. Dong, M. Jian, and L. Qi, "Fast 3D face reconstruction based on uncalibrated photometric stereo," Multimed. Tools Appl. **74**(11), 3635–3650 (2015).

69. B. Shi, Y. Matsushita, Y. Wei, C. Xu, and P. Tan, "Self-calibrating photometric stereo," in *2010 IEEE Computer Society Conference on Computer Vision and Pattern Recognition* (IEEE, 2010), pp. 1118–1125.

70. M. F. Hansen, G. A. Atkinson, L. N. Smith, and M. L. Smith, "3D face reconstructions from photometric stereo using near infrared and visible light," Comput. Vis. Image Underst. **114**(8), 942–951 (2010).

71. S. Barsky and M. Petrou, "The 4-source photometric stereo technique for three-dimensional surfaces in the presence of highlights and shadows," IEEE Trans. Pattern Anal. Mach. Intell. **25**(10), 1239–1252 (2003).

72. Y. Zhang, G. M. Gibson, R. Hay, R. W. Bowman, M. J. Padgett, and M. P. Edgar, "A fast 3D reconstruction system with a low-cost camera accessory," Sci. Rep. **5**(1), 10909 (2015).

73. C. Hernandez, G. Vogiatzis, and R. Cipolla, "Multiview photometric stereo," IEEE Trans. Pattern Anal. Mach. Intell. **30**(3), 548–554 (2008).

74. "C-S-25H0-096 Auto Focus Lens Module," https://www.corning.com/worldwide/en/innovation/corning-emerging-innovations/corning-varioptic-lenses/auto-focus-lens-modules-c-s-series/varioptic-C-S-25H0-096.html.

75. K. Majzner, A. Kaczor, N. Kachamakova-Trojanowska, A. Fedorowicz, S. Chlopicki,

and M. Baranska, "3D confocal Raman imaging of endothelial cells and vascular wall: perspectives in analytical spectroscopy of biomedical research," Analyst **138**(2), 603–610 (2013).

76. N. Everall, "Optimising image quality in 2D and 3D confocal Raman mapping," J. Raman Spectrosc. **45**(1), 133–138 (2014).

77. S. J. Baldock, A. C. S. Talari, R. Smith, K. L. Wright, and L. Ashton, "Single-cell Raman microscopy of microengineered cell scaffolds," J. Raman Spectrosc. **50**(3), 371–379 (2019).

78. F. Adar, "Depth Resolution of the Raman Microscope: Optical Limitations and Sample Characteristics," https://www.spectroscopyonline.com/view/depth-resolution-raman-microscope-optical-limitations-and-sample-characteristics.

7. Publications

In this section, the reprints of the publications are considered for the thesis as shown following. All details regarding the copyright are indicated on each title page.

[WY 1] Development and evaluation of a hand-held fiber-optic Raman probe with an integrated autofocus unit

Wei Yang, Florian Knorr, Jürgen Popp, and Iwan W. Schie

Optics Express, vol. 28, no. 21, pp. 30760-30770, 2020

DOI: 10.1364/OE.401207

[WY 2] Raman ChemLighter: Fiber optic Raman probe imaging in combination with augmented chemical reality

Wei Yang, Abdullah S. Mondol, Clara Stiebing, Laura Marcu, Jürgen Popp, and Iwan W. Schie

Journal of biophotonics, vol.12, no.7, e201800447,2019

DOI: 10.1002/jbio.201800447

[WY 3] Real-time molecular imaging of near-surface tissue using Raman spectroscopy

Wei Yang, Florian Knorr, Ines Latka, Jürgen Popp, and Iwan W. Schie

Light: Science & Applications, vol.11, no.90, 2022

DOI: 10.1038/s41377-022-00773-0

7.1 [WY 1]

Development and evaluation of a hand-held fiber-optic Raman probe with an integrated autofocus unit

Wei Yang, Florian Knorr, Jürgen Popp, and Iwan W. Schie

Optics Express, vol. 28, no. 21, pp. 30760-30770, 2020
DOI: 10.1364/OE.401207

Der Nachdruck der folgenden Publikation erscheint mit freundlicher Genehmigung von OSA
Erklärung zu den Eigenanteile der Promovend sowie weitere Doktoranden / Doktorandinnen als Koautoren an den Publikationen und Zweitpublikationsrechten bei einer kumulativen Dissertation.

Doktoranden	Wei Yang
Konzeption des Forschungsansatzes	X
Planung der Untersuchungen	X
Datenerhebung	X
Datenanalyse und –interpretation	X
Schreiben des Manuskripts	X
Vorschlag Anrechnung Publikationsäquivalente	1,0

Research Article Vol. 28, No. 21 / 12 October 2020 / Optics Express 30760

Optics EXPRESS

Development and evaluation of a hand-held fiber-optic Raman probe with an integrated autofocus unit

WEI YANG,[1] FLORIAN KNORR,[1] JÜRGEN POPP,[1,2] AND IWAN W. SCHIE[1,3,*]

[1] *Leibniz Institute of Photonic Technology Jena, Albert-Einstein-Strasse 9, 07745 Jena, Germany*
[2] *Institute of Physical Chemistry and Abbe Center of Photonics, Friedrich Schiller University Jena, Helmholtzweg 4, 07743 Jena, Germany*
[3] *Department of Medical Engineering and Biotechnology, University of Applied Sciences - Jena, Carl-Zeiss-Promenade 2, 07745 Jena, Germany*
[*] *iwan.schie@leibniz-ipht.de*

Abstract: Current implementations of fiber-optic Raman spectroscopy probes are frequently based on non-contact probes with a fixed focus and thus and have to precisely maintain the probe-to-sample distance to ensure a sufficient signal collection. We propose and experimentally demonstrate a novel hand-held fiber-optic Raman probe design, which is based on a liquid lens autofocusing unit, combined with a distance sensor and an in-house developed algorithm to precisely determine the probe-to-sample distance. The reported probe significantly improves the signal stability even for hand-held operation, while reducing distance-dependent artifacts for the acquisition of Raman spectra and can improve the acquisition of Raman spectra in a variety of applications.

1. Introduction

In recent years, there has been a significant effort to use Raman spectroscopy in a clinical and pharmaceutical environment, because it is label-free and non-invasive and can provide specific molecular fingerprint information from organic and inorganic materials [1–6]. Because of their small size fiber-optic Raman probes provide significant advantages in comparison to high-performance, but rigid microscopy setups, because they allow a direct access to measurement sites where needed. Hence, they are favored for complex environments, such as *in vivo* clinical applications, over confocal Raman microscopy platforms [7–9]. Typically, fiber-optic probes acquire Raman signal in contact or by focusing the excitation light using a fixed focal length objective lens, which requires the user to maintain the same probe-to-sample distance to effectively excite and collect the Raman signal. This restricts the usability and the advantages of the probe as a hand-held device [10]. To circumvent this challenge one approach is to use Raman probes in contact [11] or attach a removable distance regulator to the tip of the probe [12]. However, in certain instances, e.g. clinical and pharmaceutical applications, using a probe in contact is not desirable to avoid any disturbance or contamination of the sample and the probe head. Furthermore, the risk of deforming and damaging the sample increases when measuring in contact. As such, there is a demand for fiber-optical probes, which allow a stable non-contact measurement, but automatically maintaining the correct focal distance between the probe and the sample.

In recent years, there has been a continuous development of novel beam shaping approaches, which allow a rapid adjustment of the focal distance. One of the most commonly used is implemented with liquid lenses, which are based on electrowetting, i.e. the change of the wettability of a droplet on a substrate induced by changing the voltage between the droplet and

Research Article Vol. 28, No. 21 / 12 October 2020 / Optics Express 30761
Optics EXPRESS

the insulating substrate. This change leads to deformation of the droplet curvature, and as such, change in the optical focal length [13,14]. Liquid lenses have been readily used for various applications, such as autofocus cameras [15,16], microscopy imaging [17], optical coherence tomography angiography [18], optical sectioning tomography [19], lasers [20] and eyeglasses [21]. Also, a commercial Raman spectrometer based on a liquid lens has been recently made available [22,23].

In this work, we present a new fiber optical Raman probe design and implementation with an integrated liquid lens that allows a rapid focal distance adjustment and enables significant signal stabilization when compared to a fixed-focus implementations. We provide the design considerations and validate experimentally the in-house build fiber-optic Raman probe with the autofocus feature operated in hand-held mode. The probe design is based on coaxial, dual fibers that deliver the excitation light and acquire the Raman signal through a voltage-driven liquid lens. Thanks to the stable and fast focal distance adjustment, the liquid lens combined with the in-house build autofocus algorithm can minimize the influence from distance changes during hand-held operation. The approach has a high potential for pharmaceutical characterization and clinical *in-vivo* applications and can further be extended to any other optical spectroscopic approach, which requires focusing light onto a sample.

2. Materials and methods

The in-house build probe is designed in a coaxial, dual-channel configuration, where one channel guides the excitation laser to the probe and the second guides the Raman signal to the spectrometer (see Fig. 1). The laser light is delivered by a 105 µm fiber and passes through a 785 nm band-pass filter to remove the silica Raman background from the excitation fiber. A liquid lens unit (C-S-25H0-096-03; Corning Varioptic Lenses, Lyon, France [24]) with an f# of 3.7 was used in-reverse. The generated Raman signal is collected by the liquid lens and, after passing a dichroic and long-pass filter, coupled into a 200 µm multimode fiber that is attached to a spectrometer. The liquid lens has a variable dioptric power ranging from −15 diopters to +38 diopters and is connected to the power supply through a flexible printed circuit (FPC) cable. The liquid lens has an anti-reflective coating, which has been optimized in the near infrared and has a transmission above 90% between 800–1100 nm, covering the high- and low-wavenumber region for a 785 nm Raman excitation. The supply driver (USB-M Flexiboard, Corning Varioptic Lenses, Lyon, France) is software-controlled through a USB cable, delivering a 1 kHz alternating current (AC) voltage to drive the liquid lens and allowing the liquid lens a response time of about 15 ms. The Raman spectroscopy setup is equipped with a 785 nm laser, reaching a maximum output power of 300 mW (FERGIE-785 nm laser; Princeton Instruments, Trenton, New Jersey), a spectrometer (Acton LS785; Princeton Instruments, Trenton, New Jersey) and a back-illuminated deep-depletion charged coupled device (BI-DD-CCD, PIXIS-100-BReXcelon; Princeton Instruments, Trenton, New Jersey).

Generally, there are two ways to realize an autofocus function for the designed probe: open- and close-loop implementation. The open-loop method uses an external sensor to adjust the focus distance of the liquid lens; the closed-loop method is changing the focus distance by evaluating the Raman signal intensity. In principle, the closed-loop method is more favorable, as no additional hardware is required for the implementation of the autofocusing procedure, while providing a high accuracy [16]. The main disadvantage, especially for low-light implementations, is that multiple acquisitions (between 8 to 12) are required [25] to find the correct voltage for the liquid lens, making it less feasible for low-light applications. In the open-loop method the distance measurement is decoupled from the signal acquisition, since an additional sensor is used, which can be correlated to the correct focal position using a look-up table (LUT). This can be done, since the response of the liquid lens has a linear focusing power vs. voltage response. Thus, the whole procedure can be faster, but at the cost of increased complexity. Since Raman

Research Article Vol. 28, No. 21 / 12 October 2020 / Optics Express 30762
Optics EXPRESS

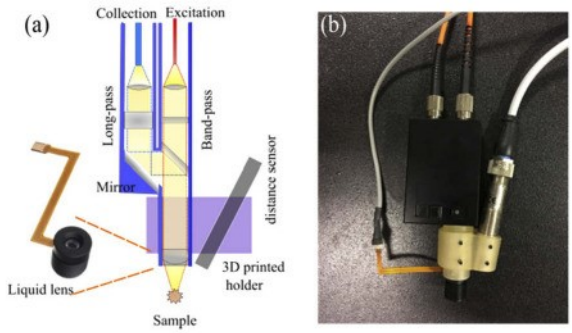

Fig. 1. Diagram of the in-house build Raman probe with an integrated liquid lens as the objective lens and a distance sensor, which is attached to the probe by a 3D-printed holder to maintain a defined relation for the realization of the autofocus function (a). Photograph of the hand-held Raman probe (b).

spectroscopy is a very low-light application, i.e. dependent on the sample less than one in a billion photons get scattered, only the open-loop implementation appears to be feasible. However, because the open-loop method alone can lead to some loss in accuracy a combined method for a fast and precise autofocusing procedure, i.e. open-loop for coarse search and closed-loop for fine adjustment can be desirable. For the coarse search, as indicated in Fig. 1(b), an ultrasonic distance sensor (UM12-1172271; SICK, Germany), which is voltage-driven and has a response time of 30 ms is read out by a multifunction I/O device (USB6001; National Instruments, Austin, Texas) and is fixed to the probe with a three-dimensional (3D) printed holder. Adding the 15 ms response time of the liquid lens, the total response time for the open-loop method is 45 ms. For the fine search, we apply a closed-loop method to find the best driven voltage for the liquid lens by iterative maximization of the Raman signal. The approach is similar to the sharpness-based optimization in Ref. [16]. The recorded signal, i.e. defined Raman band, is compared to an initial value and the voltage of the lens is adjusted accordingly and a new signal is recorded. If the signal is increasing the algorithm changes the voltage continuous in the same direction. If the signal is decreasing the algorithm goes to the opposite direction from the initial starting point until the signal decreases again, and the algorithm stops. We have been using bands with the highest intensity when performing the closed-loop implementation. One has to keep in mind that potential problems stemming from sample autofluorescence or heterogeneous molecular content distribution could arise when using only a single band. In such situations, a more comprehensive approach, for example based on spectral fitting should be applied. Nevertheless, for the proof-of-principle experiment the single-band approach has been quite suitable. Once the distance sensor detects a distance change beyond the certain threshold, the autofocus procedure will go back to the open-loop method followed by the closed-loop method. It is also important to point-out that the closed-loop approach can only be used when sufficient Raman signal is generated, or the change in the probe-to-sample distance does not change faster than the signal maximization procedure.

For the open-loop method, a calibration is performed by building a functional relationship between the distance sensor and the liquid lens. As shown in Fig. 2, there is always a trigonometric function between the focus length f and measured distance d_s of the distance sensor as following:

$$f = cos\alpha \cdot d_s - d_0 \tag{1}$$

α and d_0 represents the angle and vertical distance between the lens with the distance sensor and are constant once the liquid lens and distance sensor are fixed with the probe. Additionally, the focal length f is equal to the reciprocal of the dioptric power D, which itself is linear to the

Research Article Vol. 28, No. 21 / 12 October 2020 / Optics Express 30763
Optics EXPRESS

driving voltage U_L in the optical power [13,24], and d_s is linear to the readout voltage U_S of the distance sensor; a_1, b_1, a_2, b_2 are respectively constants for each equations:

$$\begin{cases} f = \frac{1}{D} = \frac{1}{a_1 \cdot U_L + b_1} \\ d_S = a_2 \cdot U_S + b_2 \end{cases} \tag{2}$$

By combining Eq. (1) and (2), we can determine the relationship between U_L and U_S as following:

$$U_L = \frac{1}{cos\alpha a_1 a_2 \cdot U_S + cos\alpha a_1 b_2 - a_1 d_0} - \frac{b_1}{a_1} \tag{3}$$

To simplify Eq. (3), the constants are combined, and new constant characters are assigned, resulting in a mathematic formula for the autofocusing of the probe as following:

$$U_L = \frac{1}{a \cdot U_S + b} + c \tag{4}$$

Instead of performing complex measurements of α, d_0, d_s or establishing the relationship between f and U_L, a calibration function for the relation between U_L and U_S can be built by changing the probe-to-sample distance step by step, while measuring the voltages of the distance sensor and the best-driven voltages according to the Raman signal intensities. To find corresponding best-driver voltages for the highest Raman signals we additionally used the close-loop approach, which is based on the iterative feedback of the difference of the Raman signals. The closed-loop method is also applied for the fine search for the autofocus procedure afterwards. Based on the combined open-loop and closed-loop method, the probe allows fast, dynamic and accurate adjustment of the focus length, while the probe is moved over the sample, and a simultaneous Raman signal acquisition.

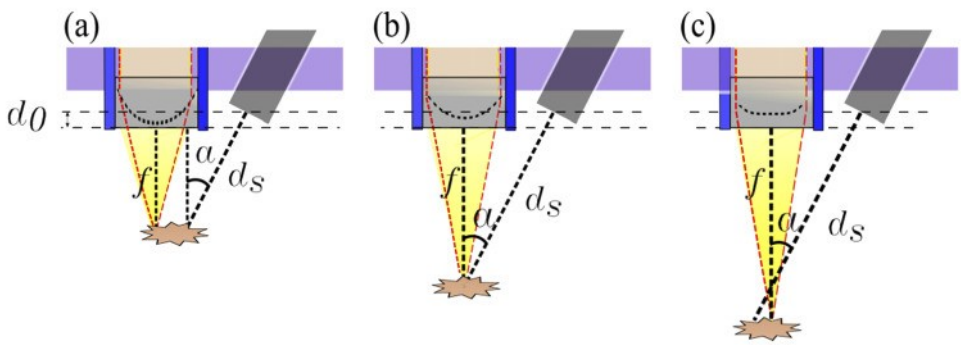

Fig. 2. Repetitive positions of the sample at close distance (a), correct distance (b) and far distance (c). The triangle function between f and d_s is always true once the liquid lens and the distance sensor are fixed.

3. Results and discussion

3.1. Calibration

For calibration, the probe is placed on a manual z-translational stage, which allows to accurately change the probe-to-sample distance step-by-step. For each step the voltage of the distance sensor V_S as well as the related best-driving voltage of the liquid lens U_L is measured. Figure 3(a) shows a repetitive result of finding the best driving voltage for the liquid lens for $U_S = 0.24$ V using the closed-loop method based on iterative feedback. Here, the output excitation power

Research Article Vol. 28, No. 21 / 12 October 2020 / Optics Express 30764
Optics EXPRESS

from the probe was about 80 mW and the detector was set to an acquisition time of 0.5 s, acquiring Raman spectra from a piece of plastic sample. Then, the measurement was repeated by changing the positions of the z-translational stage. The recorded data of the voltage readout of the distance sensor vs. the related best-driver voltage for the liquid lens (green dots) and the curve fit (blue dashed curve) using the derived mathematic relation, Eq. (4), are plotted in Fig. 3(b). The corresponding Raman spectra, after baseline removal [26], acquired during the calibration procedure are shown in Fig. 3(c). The Raman bands of each spectrum are clearly comparable, despite the different probe-to-sample distances. There is, however, a small difference between the recorded intensities, which are mainly due to the fact that various focal length lead to different numerical apertures (NA), and in consequence lead to different ability to accept the inelastically scattered light. The red and blue dot indicates the intensity of the Raman band around 830 cm^{-1} for $U_S = 0.21$ V and 0.43 V respectively, thus the longer focal length leads to the smaller NA, reduced ability to accept light, and vice versa. This effect certainly can be compensated by either calculating the NA-dependent change of the intensity or by mapping this change experimentally. However, the correction will be limited by different noise-levels of the signals.

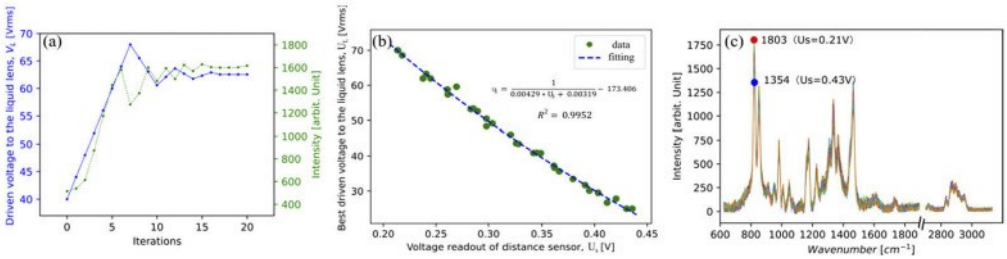

Fig. 3. Calibration procedure to determine the best-driver voltage to the liquid lens for $U_S = 0.24$ V (a), of various voltages of readout of distance sensor vs. best driven voltages for the liquid lens (b), and of the recorded Raman spectra during the whole procedure (c).

3.2. Evaluation of autofocus function

To evaluate the autofocus function established in the calibration procedure, Fig. 3(b), we have placed the sample on a manual z-translational stage and changed the probe-to-sample distance over a range of 4 mm, i.e. ± 1.8 mm around the central focal position. During the gradual and periodical change Raman spectra were recorded simultaneously. The corresponding signal, here the Raman band intensity at 830 cm^{-1}, is plotted in blue at the top of Fig. 4(a) and the distance change vs. time is plotted in the green at the bottom of Fig. 4(a). Representative spectra from three measurement points (MPs), corresponding to different probe-to-sample distances and indicated by the dots in Fig. 4(a), are plotted in Fig. 4(b). As was already seen in Fig. 4(a), the signal intensity has not significantly changed over the distance range of 3.6 mm, e.g. the ratio of the distance range −1.8 mm and +1.8 mm (MP3 to MP1) is 0.77 (1259/1632). As stated before, the observed intensity difference comes from the changing in the NA, thus shorter focal length can accept more inelastically scattered Raman signal, resulting in higher Raman intensities. Although the intensity at each MP does vary, the corresponding Raman spectra are clearly recognizable.

For comparison, we also performed the same experiment, but without the developed autofocus features, i.e. with a fixed focal length, Fig. 4(c, d). From these plots we can deduce that the focal length is around 5 mm, where the highest Raman signal intensity is collected. Changing the distances of the sample to the probe in the same range as in the previous experiment, +1.8 mm to −1.8 mm, leads to a significant signal intensity loss, to a point where almost no signal can be recovered. This can be seen in the Raman spectra measured at MP4-6, Fig. 4(d). Among

Research Article Vol. 28, No. 21 / 12 October 2020 / Optics Express 30765
Optics EXPRESS

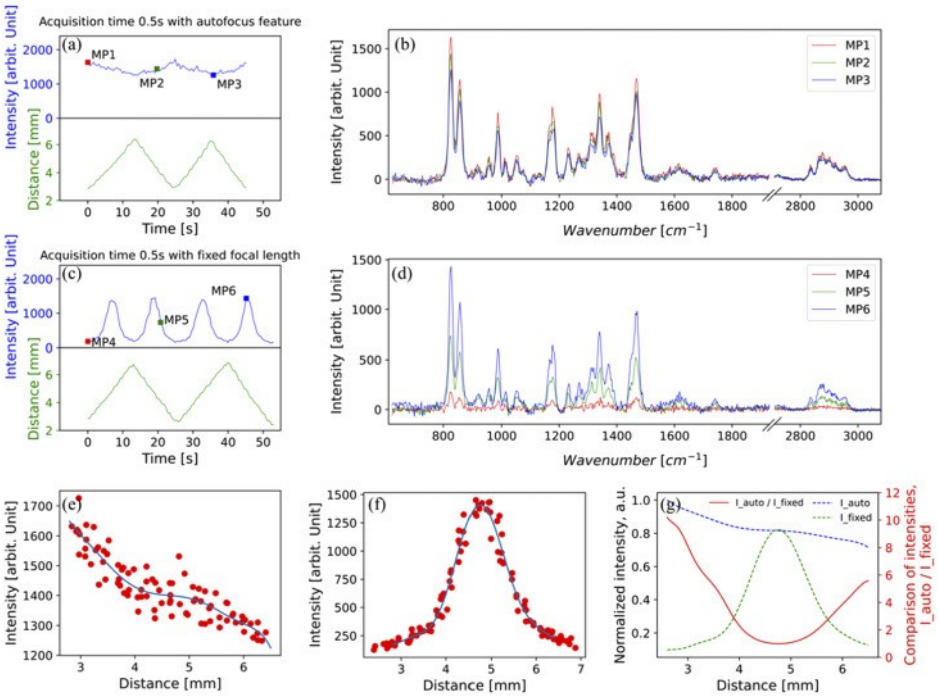

Fig. 4. Comparison and characterization of Raman signal acquired with fixed and autofocus adjustment. Raman intensity of the band at 830 cm^{-1} and distances recorded from continuously changing the objective-to-sample distance with autofocus focal length (a) and with fixed focal length (c). Raman spectra of three represent measurement points (MPs) respectively for both cases (b) and (d). Intensity of measurements from (a) and (c) plotted vs. sample-to-probe distance for autofocus probe (e) and with fixed focal length probe (f) additionally with a 5th-oder polynomial fit. Intensity normalized fits, $I_{\_auto}$ and $I_{\_fixed}$, and ratios of those values provide the gain-factor for the autofocusing approach in comparison to fixed-focal lens (g).

these three points, point 6 is located in the best focus and has the highest intensity spectrum (blue). The MPs 4 (red) and 5 (green) are out of focus measurements, resulting in significantly reduced signal intensity, with a ratio between lowest MP4 to highest MP6, of 0.12 (177/1433). In other words, the collected signal is reduced ~8-fold, while for the autofocusing approach only ~1.3-fold, resulting in a 6-fold improvement for this case. It is evident that the improvement must be distance-dependent, because for an identical focal length and probe-to-sample distance, the signals must be equal, i.e. the gain factor is one, while for out-of-focus measurements the autofocus probe would provide a measurable improvement. To determine the distance-depended gain-factor we have plotted the distance dependent changes for each distance-intensity pair in a scatter plots for both measurement conditions, Fig. 4(e and f). A 5th order polynomial fitting was applied to the data points, providing an approximation for the probe-to-sample intensity variation, blue lines. The curves for both focusing approaches are strikingly different. In the autofocusing approach the signal intensity is increasing when the focus is located closer to the probe; for the fixed-focal length probe the signal follows a Gaussian shape. The two distance-intensity curves were normalized to the max. intensity and plotted as $I_{\_auto}$ and $I_{\_fixed}$ in common distance range, Fig. 4(g). It can be seen that at the same focal length and sample-to-probe distance the signals are identical but begin to deviate for out-of-focus measurements for the fixed focus. To determine the achievable and distance-dependent gain factor we also plot in red the ratio between

Research Article Vol. 28, No. 21 / 12 October 2020 / Optics Express 30766
Optics EXPRESS

the normalized curves, Fig. 4(g). From this data- it can be seen that the gain will differ for the probe-to-sample distance, and can be as high as 10-fold for the current implementation. The experimental characterization demonstrates that the reported Raman probe with the liquid lens has a z-axis working range of ~2.8 mm to 6.4 mm instead of a fixed working distance, and effectively compensates for distance-dependent signal reductions. The current working range is limited by the maximum tunability of the liquid lens but can be improved with an optimized and custom-designed liquid lens tailored for the applications. With the help of the autofocus feature the probe dynamically adjusts the focal length to fit with the objective-to-sample distance to get clear and distinguished Raman spectra.

3.3. Performance and further discussion

To show the improved functionality using the autofocusing hand-held probe, we have first performed a measurement with a fixed focal length and an acquisition time of 0.5 s. Because the hand movement is quite rapid, only the open loop method was used to correct for the distance changes. The intensity of the strongest band at 823 cm^{-1} (blue trace) and the distance (green trace) are plotted versus time, Fig. 5(a). As expected, it is not feasible to maintain a stable sample-to-probe distance, resulting in a reduction of the signal intensity, which can be seen on the high standard deviation as indicated in the graph. The corresponding mean spectrum with standard deviation is plotted in Fig. 5(b). To show that the newly developed probe can improve the signal collection during a real hand-held measurement 100 Raman spectra were continuously acquired from the same sample, while holding the probe by hand. The intensity band at 823 cm^{-1} (blue trace) and the distance (green trace) are plotted versus time, Fig. 5(c) and the corresponding mean spectrum with standard deviation is plotted in Fig. 5(d). During the hand-held acquisitions the probe-to-sample distance (green trace) changes significantly, up to 3 mm, the intensity (blue trace), however, remains very stable when compared to the variations for the fixed focal distance probe, Fig. 5(a). The improvement can be seen when comparing the mean spectra and the standard deviation Fig. 5(b) and (c). Even if there are some sudden hand movements, the autofocus function can rapidly adjust the focal length to achieve improved results.

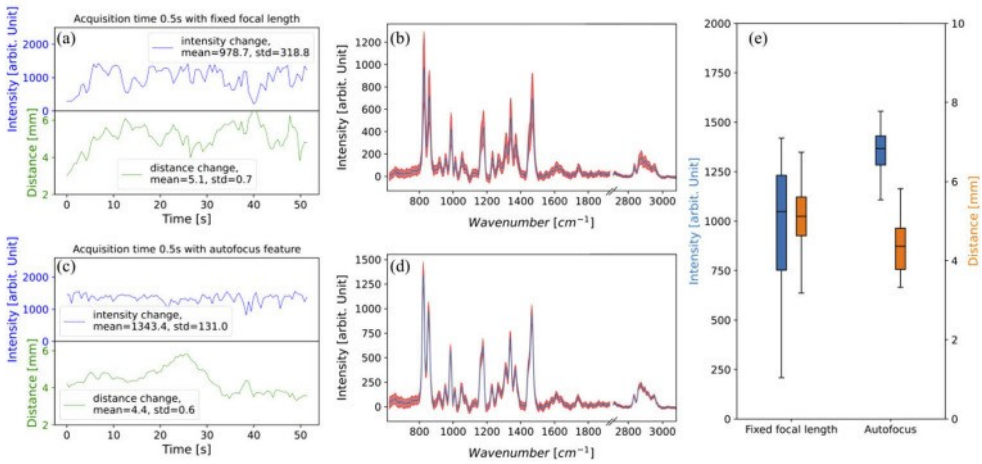

Fig. 5. Raman signal recorded vs. the distances in handheld operation for both cases. Raman intensity of the band at 823 cm^{-1} and the sample-to-probe are plotted vs. time for the fixed-focal length (a); corresponding mean Raman spectrum (blue) with standard deviation (red) (b). Raman intensity of the band at 823 cm^{-1} and the sample-to-probe are plotted vs. time for the autofocus method (c); corresponding mean Raman spectrum (blue) with standard deviation (red) (d).

Research Article Vol. 28, No. 21 / 12 October 2020 / Optics Express 30767
Optics EXPRESS

To better compare those results, the intensity change and distance change were plotted in a box plot, Fig. 5(e). It can be clearly seen that while the variations of the distances are comparable, the standard deviation of the intensity is significantly reduced.

Furthermore, since the response-time effects is more noticeable with reduced acquisition time, measurements were also performed for 0.1 s and 1 s, Fig. 6. The intensity and distance vs. time traces are plotted in Fig. 6(a) and (c); and the corresponding mean Raman spectra with the standard deviation are plotted in Fig. 6(b) and (d). A comparison between the different acquisition times shows that it can influence the intensity compensation, i.e. for shorter acquisition time it is more challenging to adjust the distance change, when compared to longer acquisition time. This is due to speed limitation resulting from the open-loop method, which is approx. 45 ms and as such, close to the acquisition time of 100 ms. Once the hand movement occurs during the acquisition the liquid lens may delay the adjustment of the focal length, leading to higher intensity changes. Nevertheless, the stability is still higher than for the fixed focal length, which can be seen by comparing Fig. 5(a) and Fig. 6(a). For longer acquisition time, the delay of liquid lens response is not obvious and does not play a significant role for the intensity, thus the intensity is more stable.

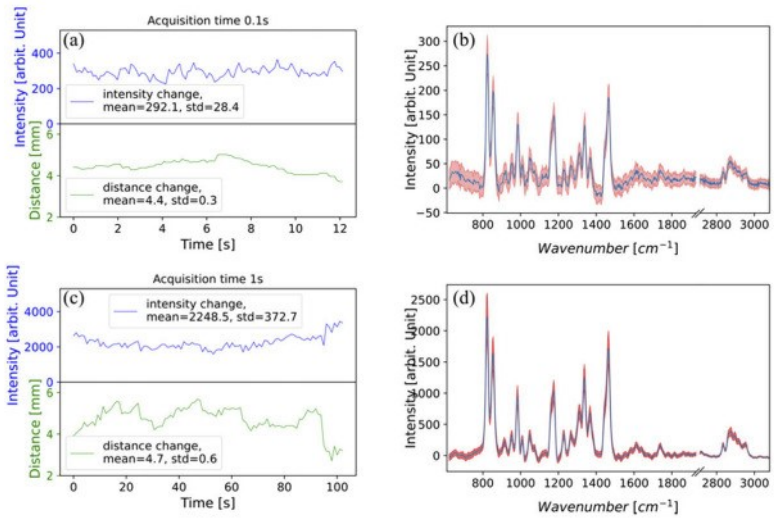

Fig. 6. Raman spectra acquired with the autofocusing probe at different acquisition times. Raman intensity of the band at 823 cm^{-1} and the sample-to-probe distance plotted vs. time for an acquisition time of 0.1s (a); corresponding mean Raman spectrum (blue) with standard deviation (red) (c). Raman intensity of the band at 823 cm^{-1} and the sample-to-probe plotted vs. time for an acquisition time of 1.0 s (a); corresponding mean Raman spectrum (blue) with standard deviation (red) (d).

In addition, we have used the developed probe for Raman imaging, which provides visual information on the distribution of macromolecules in the sample. In this experiment the probe was fixed vertically on a holder and a bio-sample (a piece of pork meat) was placed tilted by 15° on a X-Y motor scanning stage (MLS203-1, Thorlabs, Newton, New Jersey), Fig. 7(a). An image with 14×14 points and a step size of 500 µm was acquired using fixed focal length configuration with an acquisition time of 0.5 s. The net z-directionally displacement from one side to the other was approx. 1.8 mm. The Raman image based on the intensity mapping of the Raman band at 1459 cm^{-1} and corresponding mean spectrum with standard deviation are shown in Fig. 7(b) and (c), respectively. As expected, due to the tilt of the sample and the resulting change in the probe-to-sample distances a significant intensity change can be observed in the x-dimension in

Research Article Vol. 28, No. 21 / 12 October 2020 / Optics Express 30768
Optics EXPRESS

the image. Because the tilt was in the x-axis only, the probe-to-sample distances is the same in the y-axis. The experiment was repeated in the same location, but with the use of the autofocus probe. Because the probe was fixed in place, the close loop approach was also used. The resulting Raman image and corresponding mean Raman spectrum with the standard deviation are shown as Fig. 7(d) and (e), respectively. For comparison, the intensity variation for the 1459 cm^{-1} band for the fixed focal length and for the autofocus mode were plotted in a box plot, Fig. 7(f). Comparing the results, it is obvious that using the liquid lens with the autofocus approach almost completely offsets the influence of tilt, and as such, the mismatch between the probe-to-sample distance and the focal length. The method can, therefore, also be used for performing Raman imaging on uneven surface, which was realized using translational piezo stages. It is, however, important to point out that the limitation of the implemented ultrasonic distance sensor is that a flat surface of at least 3 mm^2, i.e. ca. 1 mm in diameter is, required to reflect the ultrasound back to the receiver, thus, the probe can work with the sample which satisfies this condition, including liquid or powdery samples. The current combined autofocus algorithm is restricted to the sample with highly uneven surface; on the other hand, the closed-loop algorithm has no restriction on this kind of applications, however, if a very fast sampling is required it could limit the autofocus procedure. As such, the designed probe with only the open-loop approach, may be restricted to low-resolution. However, modifications on the ultrasound sensor, which allow improved focusing ability could significantly improve the resolution and the range of applications.

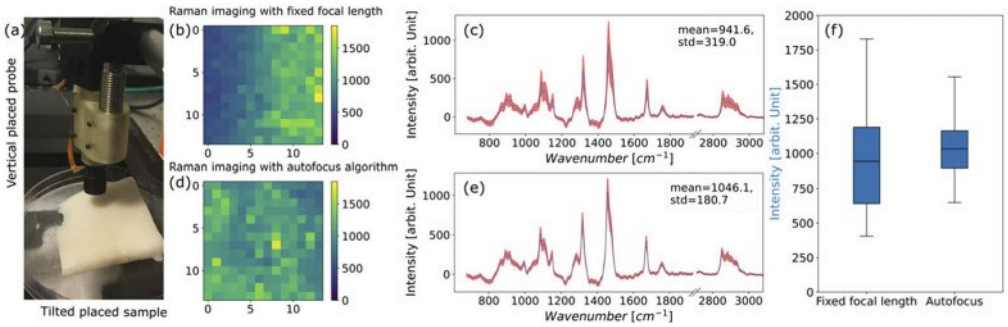

Fig. 7. Photograph of the setup doing Raman imaging using our present probe on a tilted placed bio-sample (a); Raman image result with fixed focal length (b) and corresponding mean Raman spectra (blue) with the standard deviation (red) (c); Comparison Raman image result with the autofocus method (d) and corresponding mean Raman spectra (blue) with the standard deviation (red) (e). The intensity variation for the band at 1459 cm^{-1} for the fixed focal length and for the autofocus mode are plotted in (f).

The comparison between the performance of the fixed focal length probe and variable focal length probe shows a significant improved performance for the signal acquisition for hand-held Raman probes, allowing the acquisition of Raman spectra without reducing the signal intensity. Furthermore, the proposed approach can be extend to many other optical modalities, which need to focus light to the sample, such as fluorescence lifetime imaging microscopy (FLIM), second harmonic generation (SHG) imaging, coherent anti-Stokes Raman scattering (CARS) and others. It is, however, important to point out that for non-linear modalities the change in the NA could result in a significant signal generation reduction, which is why a thorough characterization of the change of the NA is essential.

4. Conclusion

In the reported work, we present a hand-held autofocus fiber-optic Raman probe, which allows to overcome the probe-to-sample distance problems by dynamically adjusting the focal length of the

Research Article Vol. 28, No. 21 / 12 October 2020 / Optics Express 30769

Optics EXPRESS

probe. The reported approach is realized based on a liquid lens implementation combined with an open and closed-loop algorithm, where the open-loop method uses an ultrasonic distance sensor for coarse search and adjusts the focal length and the closed-loop method uses feedback of Raman intensity for fine search. The performance of the proposed probe was experimentally evaluated on a sample by acquiring spectra, while continuously changing the probe-to-sample distance during a hand-held operation. Through comparison to control experiments using a fixed focal length it could be shown that the autofocus allows to acquire Raman spectra without reducing the distance-related signal intensity, whereas the experiment with a fixed focal-distance probe, resulted in significant signal loss. Under current experimental conditions, the present probe has a dynamic distance range of about from 2.8 mm to 6.4 mm, and a response time of 45 ms, which can easily tolerate the instability of hand-held operation. The close-loop implementation can in future developments significantly benefit from spectral fitting approaches, which could help to deal with potential problems from sample autofluorescence or heterogeneous molecular content distribution, when compared to using a single Raman band. This reported work can significantly improve the performance of hand-held Raman probes and enables the acquisition of spectra without reduced performance. Furthermore, this approach can be extended to other spectroscopy and microscopy modalities, such as FLIM, SHG, CARS and others.

Funding

China Scholarship Council; European Research Council; Bundesministerium für Bildung und Forschung (01KL1904); Horizon 2020 Framework Programme (No 667933).

Acknowledgements

W.Y. received a scholarship support from the China Scholarship Council.

Disclosures

The authors declare no conflicts of interest.

References

1. E. Cordero, I. Latka, C. Matthäus, I. W. Schie, and J. Popp, "In-vivo Raman spectroscopy: from basics to applications," J. Biomed. Opt. **23**(07), 1 (2018).
2. M. J. Baker, H. J. Byrne, J. Chalmers, P. Gardner, R. Goodacre, A. Henderson, S. G. Kazarian, F. L. Martin, J. Moger, N. Stone, and J. Sulé-Suso, "Clinical applications of infrared and Raman spectroscopy: state of play and future challenges," Analyst **143**(8), 1735–1757 (2018).
3. E. Upchurch, M. Isabelle, G. R. Lloyd, C. Kendall, and H. Barr, "An update on the use of Raman spectroscopy in molecular cancer diagnostics: current challenges and further prospects," Expert Rev. Mol. Diagn. **18**(3), 245–258 (2018).
4. F. Nardella, M. Beck, P. Collart-Dutilleul, G. Becker, C. Boulanger, L. Perello, A. Gairard-Dory, B. Gourieux, and G. Ubeaud-Séquier, "A UV-Raman spectrometry method for quality control of anticancer preparations: Results after 18 months of implementation in hospital pharmacy," Int. J. Pharm. **499**(1-2), 343–350 (2016).
5. H. Chen, Z. M. Zhang, L. Miao, D. J. Zhan, Y. B. Zheng, Y. Liu, F. Lu, and Y. Z. Liang, "Automatic standardization method for raman spectrometers with applications to pharmaceuticals," J. Raman Spectrosc. **46**(1), 147–154 (2015).
6. L. Lê, M. Berge, A. Tfayli, A. Baillet Guffroy, P. Prognon, A. Dowek, and E. Caudron, "Quantification of gemcitabine intravenous drugs by direct measurement in chemotherapy plastic bags using a handheld Raman spectrometer," Talanta **196**(November 2018), 376–380 (2019).
7. I. Latka, S. Dochow, C. Krafft, B. Dietzek, and J. Popp, "Fiber optic probes for linear and nonlinear Raman applications - Current trends and future development," Laser Photonics Rev. **7**(5), 698–731 (2013).
8. C. Krafft, S. Dochow, I. Latka, B. Dietzek, and J. Popp, "Diagnosis and screening of cancer tissues by fiber-optic probe Raman spectroscopy," Biomed. Spectrosc. Imaging **1**(1), 39–55 (2012).
9. O. Stevens, I. E. Iping Petterson, J. C. C. Day, and N. Stone, "Developing fibre optic Raman probes for applications in clinical spectroscopy," Chem. Soc. Rev. **45**(7), 1919–1934 (2016).
10. Z. Sun, B. Song, X. Li, Y. Zou, Y. Wang, Z. Yu, and M. Huang, "A smart optical fiber probe for Raman spectrometry and its application," J. Opt. **46**(1), 62–67 (2017).

Research Article Vol. 28, No. 21 / 12 October 2020 / *Optics Express* 30770

Optics EXPRESS

11. J. Wang, M. S. Bergholt, W. Zheng, and Z. Huang, "Development of a beveled fiber-optic confocal Raman probe for enhancing in vivo epithelial tissue Raman measurements at endoscopy," Opt. Lett. **38**(13), 2321 (2013).
12. . "Integrated Raman Probe," https://www.ipslasers.com/integrated-Raman-probe.html.
13. B. Berge and J. Peseux, "Variable focal lens controlled by an external voltage: An application of electrowetting," Eur. Phys. J. E **3**(2), 159–163 (2000).
14. B. Berge, "Liquid lens technology: principle of electrowetting based lenses and applications to imaging," in *18th IEEE International Conference on Micro Electro Mechanical Systems, 2005. MEMS 2005*. (IEEE, n.d.), pp. 227–230.
15. J. Fuentes-Fernández, S. Cuevas, L. C. Álvarez-Nuñez, and A. Watson, "Tests and evaluation of a variable focus liquid lens for curvature wavefront sensors in astronomy," Appl. Opt. **52**(30), 7256–7264 (2013).
16. S. Pasinetti, I. Bodini, M. Lancini, F. Docchio, and G. Sansoni, "Experimental characterization of an autofocus algorithm based on liquid lens objective for in-focus imaging in the macro range," in *Proceedings - 2017 7th International Workshop on Advances in Sensors and Interfaces, IWASI 2017* (IEEE, 2017), pp. 195–200.
17. M. Bathe-Peters, P. Annibale, and M. J. Lohse, "All-optical microscope autofocus based on an electrically tunable lens and a totally internally reflected IR laser," Opt. Express **26**(3), 2359 (2018).
18. J. Yang, L. Liu, J. P. Campbell, D. Huang, and G. Liu, "Handheld optical coherence tomography angiography," Biomed. Opt. Express **8**(4), 2287 (2017).
19. C. Xu, W. Zhao, J. Hu, B. Zhang, and S. Wang, "Liquid lens-based optical sectioning tomography for three-dimensional flame temperature measurement," Fuel **196**, 550–563 (2017).
20. F. Zhang, Y. Yao, X. Qu, T. Zhang, and B. Pei, "Dual-beam laser autofocusing system based on liquid lens," Opt. Laser Technol. **88**, 198–204 (2017).
21. N. Hasan, A. Banerjee, H. Kim, and C. H. Mastrangelo, "Tunable-focus lens for adaptive eyeglasses," Opt. Express **25**(2), 1221 (2017).
22. . "The First in the Industry to use an Autofocus Solution in a Raman Spectrometer," https://serstech.com/industry-first-autofocus-an-interview-with-katja-szybek/.
23. K. Szybek and J. Sonnvik, "Raman spectroscopy system," U.S. patent US10295408B2 (2019).
24. . "C-S-25H0-096 Auto Focus Lens Module," https://www.corning.com/worldwide/en/innovation/corning-emerging-innovations/corning-varioptic-lenses/auto-focus-lens-modules-c-s-series/varioptic-C-S-25H0-096.html.
25. . "The product brochure of CorningVariopticLenses," https://www.corning.com/media/worldwide/Innovation/documents/FINAL_CorningVariopticLenses_productbrochure_5.4.18_lowresWEB.pdf.
26. S.-J. Baek, A. Park, Y.-J. Ahn, and J. Choo, "Baseline correction using asymmetrically reweighted penalized least squares smoothing," Analyst **140**(1), 250–257 (2015).

7.2 [WY 2]

Raman ChemLighter: Fiber optic Raman probe imaging in combination with augmented chemical reality

Wei Yang, Abdullah S. Mondol, Clara Stiebing, Laura Marcu, Jürgen Popp, and Iwan W. Schie

Journal of biophotonics, 12(7), e201800447, 2019
DOI: 10.1002/jbio.201800447

Der Nachdruck der folgenden Publikation erscheint mit freundlicher Genehmigung von Wiley
Erklärung zu den Eigenanteile der Promovend sowie weitere Doktoranden / Doktorandinnen als Koautoren an den Publikationen und Zweitpublikationsrechten bei einer kumulativen Dissertation.

Doktoranden	Wei Yang
Konzeption des Forschungsansatzes	X
Planung der Untersuchungen	X
Datenerhebung	X
Datenanalyse und –interpretation	X
Schreiben des Manuskripts	X
Vorschlag Anrechnung Publikationsäquivalente	1,0

Received: 2 December 2018 | Revised: 1 February 2019 | Accepted: 5 March 2019
DOI: 10.1002/jbio.201800447

Journal of BIOPHOTONICS

FULL ARTICLE

Raman ChemLighter: Fiber optic Raman probe imaging in combination with augmented chemical reality

Wei Yang[1] | Abdullah S. Mondol[1] | Clara Stiebing[1] | Laura Marcu[2] | Jürgen Popp[1,3] | Iwan W. Schie[1]*

[1]Leibniz Institute of Photonic Technology Jena, Jena, Germany
[2]Department of Biomedical Engineering, University of California Davis, Davis, California
[3]Institute of Physical Chemistry and Abbe Center of Photonics, Friedrich-Schiller University Jena, Jena, Germany

***Correspondence**
Iwan W. Schie, Leibniz Institute of Photonic Technology Jena, 07745 Jena, Germany.
Email: iwan.schie@leibniz-ipht.de

Funding information
H2020 European Research Council, Grant/Award Number: 667933

Raman spectroscopy using fiber optic probe combines non-contacted and label-free molecular fingerprinting with high mechanical flexibility for biomedical, clinical and industrial applications. Inherently, fiber optic Raman probes provide information from a single point only, and the acquisition of images is not straightforward. For many applications, it is highly crucial to determine the molecular distribution and provide imaging information of the sample. Here, we propose an approach for Raman imaging using a handheld fiber optic probe, which is built around computer vision–based assessment of positional information and simultaneous acquisition of spectroscopic information. By combining this implementation with real-time data processing and analysis, it is possible to create not only fiber-based Raman imaging but also an augmented chemical reality image of the molecular distribution of the sample surface in real-time. We experimentally demonstrated that using our approach, it is possible to determine and to distinguish borders of different bimolecular compounds in a short time. Because the method can be transferred to other optical probes and other spectroscopic techniques, it is expected that the implementation will have a large impact for clinical, biomedical and industrial applications.

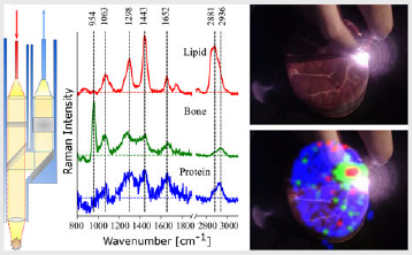

KEYWORDS
augmented reality, fiber optic probe, Raman imaging, Raman spectroscopy

1 | INTRODUCTION

Raman spectroscopy provides label-free molecular fingerprint information of organic and inorganic materials and has been frequently used in analytical chemistry. The application of Raman spectroscopy to biological samples, such as eukaryotic and prokaryotic cell, and tissue sections demonstrated that it can be a promising tool for biomedical applications and clinical diagnostics [1–4]. For example, Raman imaging of tissue samples provides visual information on the distribution of macromolecules in the sample and has been used to detect, diagnose and delineate tumor and healthy tissues [5–7]. To acquire Raman images of samples, typically, confocal Raman microscopy platforms are used [8, 9]. A Raman signal is generated in the focal spot through laser excitation, and an image can be created by mechanically translating the sample, acquiring signals at each location and mapping this signal. These microscopy devices have been widely used for ex vivo Raman imaging of tissue section. Nevertheless, these platforms are quite large, very rigid and

not easy to move, allowing only minimal access directly at the patient site. Fiber optic Raman probes can be used to overcome these problems because they combine all optical components in small handheld or endoscopic probes, providing easy access to the patient. Such probes have been widely used for ex vivo and in vivo classification of tumor grades [10–14]. One common drawback with fiber optical probes is that information is only recorded from a single point and no imaging information can be acquired, without a suitable mechanical translational stage. This drawback significantly diminishes the advantages of Raman spectroscopy for in vivo applications. Recent studies overcome this drawback by using a bundle of several fibers to scan multiple points at once and creating a Raman image through a scanning mirror on the detection side rather than mechanical translation of a stage [15]. Also, an imaging fiber approach using gradient-index (GRIN) lenses was introduced for non-linear coherent anti-Stokes Raman scattering, which was tested on skin tissue [16]. These approaches have significant advantages for probing the molecular characterization of tissue on small scale in a fast manner. However, in most implementations, the acquired data are processed after the acquisition and cannot be directly correlated with the sample, delaying the diagnostic and analytical result. Recently, various imaging modalities, such as computed tomography, magnetic resonance imaging, ultrasound image and fluorescence lifetime have been combining their respective imaging information with images of the sample in an augmented way to improve or supplement real-time surgery [17–21]. These approaches offer the surgeons a direct interpretation of physical information from the tissues by superimposing the imaging modalities information into the visual field of view, allowing the surgeon to detect and determine locations of disease in a real-time. Although Raman spectroscopy has a significant potential for biomedical diagnostics, it has not yet been implement in a fiber optic probe–based imaging platform and in combination with augmented reality [22–24].

Here, we present a newly developed Raman-probe–based imaging approach, using a conventional handheld fiber optic Raman probe in combination with computational image processing to acquire fiber-based Raman images and display the chemical information in an augmented reality fashion in real-time. The proposed approached allows to sample surfaces and to acquire Raman images from those surfaces using a fiber probe. By simultaneously assessing positional information of the handheld probe, and acquiring and processing the spectroscopic data in real-time, it is possible to create Raman images from biological sample in a short time and visualize the data live in a comprehensible way. The chemical information can be evaluated for each position and overlaid during the acquisition with the brightfield imaging on a computer screen to create a chemical augmented reality image of the biochemical distribution on the sample surface. This method allows to easily distinguish borders of different bimolecular composition and can be extended to clinical applications of tumor margin delineation.

2 | MATERIALS AND METHODS

2.1 | Raman spectroscopy setup with handheld fiber optic probe

The schematic diagram of the instruments for the presented Raman probe imaging approach is displayed in Figure 1A. It consists of a regular webcam (C920; Logitech, Switzerland), an imaging spectrometer (IsoPlane160; Princeton Instruments, Trenton, New Jersey), a back-illuminated scientific charged coupled device (CCD) (PIXIS-400-BReXcelon; Princeton Instruments Trenton, New Jersey), and a 785 nm single-mode laser (Xtra, Toptica, Germany) with a nominal output power of max 300 mW. The setup is used to acquire conventional brightfield images and Raman spectra simultaneously. To achieve the spatial flexibility requirement, a handheld fiber optic Raman probe (RPB Laboratory Probe; InPhotonics, Westwood, Massachusetts) is used, Figure 1B. The excitation laser is fiber-coupled into a coaxial, dual fiber handheld probe. The laser passes a bandpass filter to remove the intrinsically generated Raman signals of the excitation fiber, that is, silica Raman background, and is focused into the sample plane, using a lens with a working distance of 7.5 mm. The generated Raman signal from the sample is collected by the same lens, transferred through a dichroic mirror, and a longpass filter to attenuate the Rayleigh scattered excitation signal. The Raman signal is then focused into a 200 μm collection fiber, which guides the signal to the spectrometer. The positional information of the laser spot and the corresponding Raman information are extracted by image and data processing of the acquired brightfield images and Raman spectra. The combination of

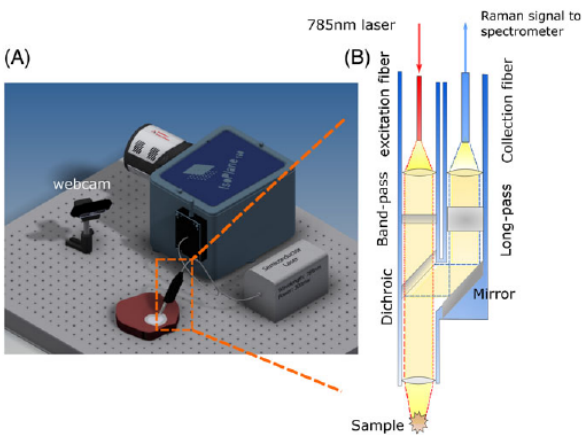

FIGURE 1 Diagram of the setup, which contains of a regular webcam to acquire brightfield images and a handheld probe based Raman spectroscopy setup (A); and optical design of the handheld fiber optic probe (B)

the simultaneous measurements of positional information with spectroscopic Raman information, allows the reconstruction of Raman image from large tissue sample in a short time and displaying a real time augmented reality image by mean of overlaying chemical information with the brightfield image information on a computer screen. The data acquisition, analysis and image processing procedures are performed by an in-house written software in LabView (National Instruments, Austin, Texas).

2.2 | Positional tracking of the laser spot

Using an image processing algorithm, the positional information can be extracted from the brightfield images. A regular low-cost webcam is used to acquire conventional brightfield images of the sample. The image contains a high intensity Rayleigh scattering signal of the laser spot on the sample, Figure 2A, and is used to determine the position using localization algorithm. First, a single color plane is extracted from the RGB brightfield image, where each pixel of the intensity image has 8 bit (0-255) information, Figure 2B. Because the Rayleigh scattered laser light has a higher intensity than the surrounding, an intensity threshold is applied to the single color plane image, which ensures that only the signals resulting from the Rayleigh scattered light remain, resulting in a binary image, Figure 2C. To determine the central position of the excitation spot, the contour of the spot is extracted first by using a Laplacian filter, which extracts neighboring pixels with significant variations of light intensities, followed by an ellipse fitting algorithm to assess the actual shape of the excitation spot. A Laplacian 3 × 3 convolution kernel defined as:

$$\begin{matrix} a & d & c \\ b & x & b, \\ c & d & a \end{matrix}$$

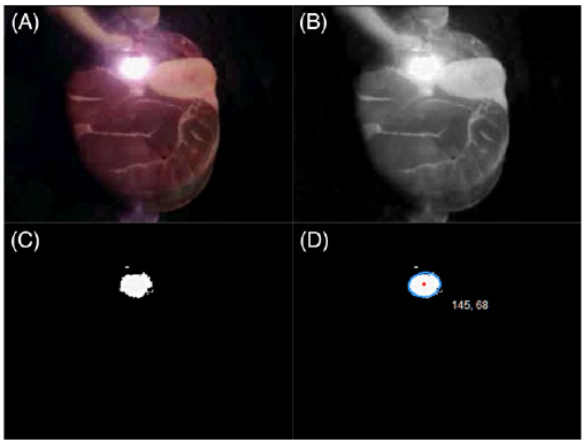

FIGURE 2 Conventional bright-field image (A), eight-bit image of extracted luminance plane (B), after the application of a threshold (C), and image with overlaid center information based on an ellipse fitting (D)

with x = 8, and all other elements as 1 was used.

For this filter function, the relation x = 2*(|a| + |b| + |c| + |d|) produces a contour of the focal spot. The positional information of the excitation spot is determined by fitting an ellipsoid function to the contour and to extract the center coordinate, Figure 2D.

2.3 | Data processing algorithm for Raman spectra

To achieve a real-time assessment of chemical information and to display the data in an augmented fashion on the computer screen, the data processing procedure has to be performed live during the data acquisition. The following sequence of data processing steps was implemented in the LabView environment: wavelength calibration, intensity calibration, offset voltage bias correction, normalization, and asymmetrically least-squares baseline correction [25–28]. Because the goal is to visualize the distribution of specific macromolecules in the sample, spectra from relevant macromolecules present in biological samples were acquire, that is, lipid, bone, and protein in Figure 3A. The spectra of these three macromolecules are shown in Figure 3B. To determine the relative macromolecule at a specific location of the sample, each measured spectrum was preprocessed and least-squares fitted by the molecular signatures of interest from the database [29]. To visualize the information each acquired spectrum during imaging procedure is assigned an RGB color, representing the relative contribution of the different chemical components. Here, the RGB color was assignment as red for lipid, green for bone, and blue for protein.

2.4 | Reconstruction of a Raman image in combination with augmented reality

The chemical information image, that is, Raman image, was created by moving the handheld probe over the area of interest. For each location, the positional information of the probe was extracted from the brightfield image, and spectroscopic information was acquired and converted to pseudo-color information as explained in 2.3. To display the chemical information, a circle with a scalable diameter was mapped onto the chemical image for each spectrum. The coordinates and the color information of the circle are determined through the positional information and chemical information, respectively. The scale of the diameter has a significant influence on the resolution of the Raman image. Too big or too small diameter will lead too smooth or too sparse Raman images, respectively. The parameter is adjustable and can be modified, depending on the specific application. Because the Raman image and the brightfield image are mapped onto the same dimensional space, the positional information is inherently identical between the images can be directly overlay to form an augmented reality image. This augmented reality image is updated live during the data acquisition.

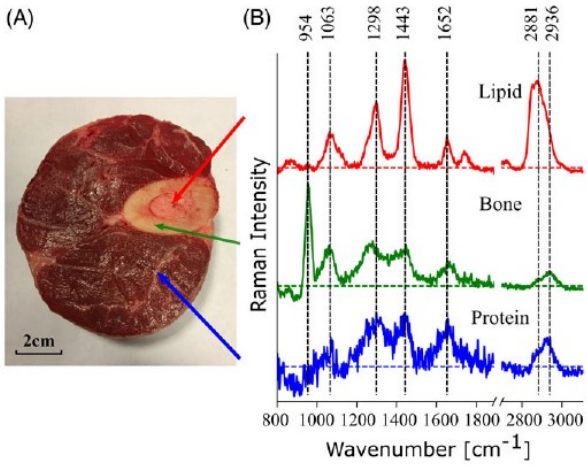

FIGURE 3 Image of the proposed sample, a beef steak with bone (A), and mean spectra of the main chemical contributions of the sample, lipid, bone and protein (B)

3 | RESULTS AND DISCUSSION

To demonstrate the performance of the newly developed Raman imaging approach in combination with augmented reality, a biological tissue was measured, which contains multiple structured components, that is, bone, lipid and protein-rich structures. Figure 4 displays representative results from the measurement at three different time points for brightfield images, chemical images and the augmented images in individual windows. The image resolution for the brightfield camera was set to 320 ×240 pixels, and a brightfield image stream is constantly taken from the sample at 24 Hz. Figure $4A_1$ shows the time point $t = 0$ minute, where no Raman acquisition or reconstruction of was performed. Thus, the chemical information image (Figure $4A_2$) was blank, and the augmented image (Figure $4A_3$) is identical to the brightfield image.

The spectral acquisition is triggered by pushing a button. The spectra were acquired by moving the fiber optic Raman probe above the sample. The power of the excitation laser was set to 100 mW at the sample and the spectral acquisition time to 50 ms to enable a near video-rate acquisition. As explained in section 2.4, the Raman image was acquired by moving the fiber optic Raman probe over the sample and was reconstructed using pseudo-color information, that is, red, green and blue representing lipid, bone and protein contributions, respectively. A circle with a diameter of 8 pixels combined the color information with the positional information, to form the chemical information image point by point. Figure $4B_2$ shows the online update image with the fiber optic probe scanning after approximately 3 minutes and the acquisition of 330 points. Figure $4B_3$ displays the augmented reality image for the same time. A separation of the macromolecules of interest can readily be seen.

After approximately 6 minutes, it is possible to sample a large part of the biological tissue, using the fiber optic probe to form a Raman image, consisting of 640 points, Figure $4C_{1\text{-}3}$. The entire experiment was video-recorded and can be found in the Supporting Information Video S1, alongside another video of a similar experiment to demonstrate the reproducibility of the measurement (S2). Both videos are

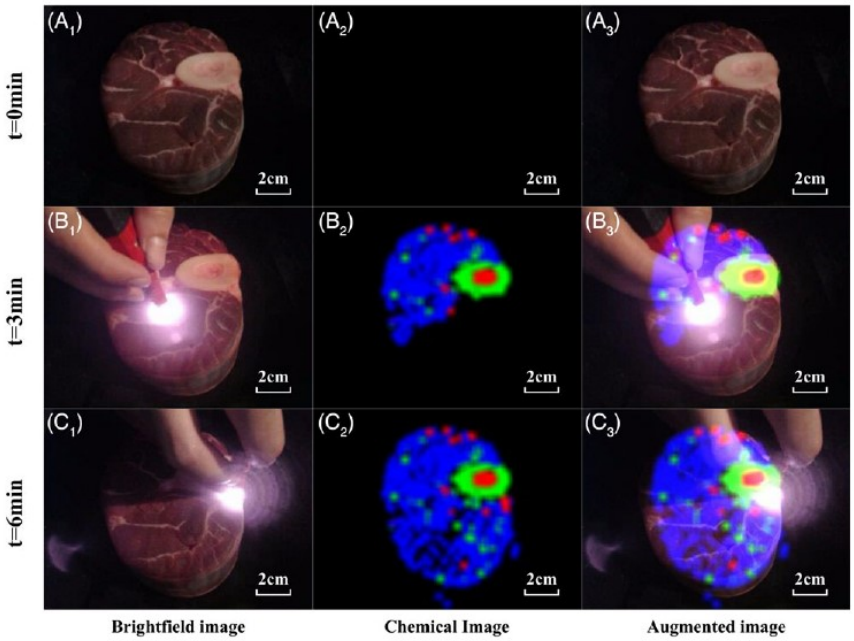

FIGURE 4 Representative Screenshot images of brightfield, chemical and augmented image at the beginning ($t = 0$ minute, A_1, A_2 and A_3), during ($t = 3$ minutes, B_1, B_2 and B_3), and at the end of the measurement ($t = 6$ minutes, C_1, C_2 and C_3). The color information represents different chemical component, that is, red for lipid, green for bone, and blue for protein

shown at 4-times the speed, as evident from the spectral acquisition time, the total measurement time, and the number of measured spectra a mismatch can be observed. Even though the acquisition time was set to 50 ms, only 640 spectra were acquired in 360 seconds. This is primarily due to the significant amount of data pre-processing and analysis on the current system. In total it takes around 0.56 s to acquire and process an individual spectrum, and to augment the chemical information in the brightfield image, resulting in an acquisition rate of approximately 1.8 Hz. Furthermore, the acquisition of a real-time screen recording slows down the processing time. This reduction of processing speed can be compensated in future implementations, using parallel processing approaches for the data processing. Nevertheless, readily in the presented implementation it is possible to distinguish between different components during the data acquisition process, resulting in a real-time assessment of the macromolecular distribution of the sample, offering a great potential to visually distinguish non-differentiable samples, such as neoplasia and healthy tissue.

The positional tracking method is based on the analysis of the brightfield image acquired by the webcam, which has a resolution of 320 × 240 pixels, corresponding at the adjusted distance to approximately 15 × 12 cm in the sample plane. The positional information for the reconstruction of the Raman image is directly related to the positional tracking, which means one Raman pixel corresponds to 0.47 mm in the sample plane. Thus the proposed approach has theoretically an achievable spatial resolution of 0.47 mm per pixel, currently limited by the resolution of the camera. However, to cover a large-enough area each spectral measurement point in the Raman image was scaled and mapped as a circle with diameter of 8 pixels, reducing the resolution of the Raman image to approximately 3.76 mm. This limitation, however, is not static as the parameters are adjustable by the user and in theory only limited by the resolution of the brightfield image and the spot size in the sample plane. The theoretical focal spot size in the sample plane is 100 μm, and is governed by the optical system in the handheld fiber probe. Here, the excitation delivery fiber, with a diameter of 100 μm imaged one-to-one in to the sample plane. As such, the current limitation for the resolution is the imaging of the brightfield camera. This, however, can readily be solved using conventional cameras, that is, commercial 2 K resolution camera and a 10 × 10 cm sample, the spatial resolution of 50 μm can readily be achieved. Another factor, which can affect the resolution and the quality of the reconstructed Raman image is the movement speed of the fiber optic probe during the measurement. A too fast movement will lead to a not fully covered and therefore sparse image. Too slow leads however to a blurred image. The parameters used here are compromised between spatial resolution, movement speed and the processing speed of the setup.

4 | CONCLUSION

In the presented work, we propose and experimentally demonstrated an implementation of a fiber-optic–based Raman imaging system in combination with augmented reality, which can be used for surface analysis of biological tissue samples. The reported approach is realized based on combining positional tracking of the laser spot through brightfield images, with the simultaneous spectroscopic measurements to assess the chemical information. The online spectral processing feature allows for short-time reconstruction of Raman images from large tissue samples, and for real-time augmentation of the chemical information with the brightfield image on a computer screen. The performance of the proposed approach was experimentally evaluated on a biological sample, showing that a Raman image can be created using a handheld probe and structural boundaries based on their molecular signatures can be discriminated. Hereby, complex Raman signatures of biological macromolecules can be displayed in a comprehendible way. Under current experimental conditions a Raman image from a large biological tissue of 15 × 12 cm at a resolution of 3.76 mm can be acquired in 6 minutes, with a spectral acquisition speed of 1.8 Hz. The current limitation due to the sequential processing of the data can be significantly improved in future implementations. The proposed method can be extended towards preclinical and clinical applications, that is, to evaluate the borders between neoplasia and normal tissue sites. Applications on ex vivo diagnostics of tissue biopsies, but also in vivo studies on skin cancer or open brain surgery, can be envisioned. Furthermore, future improvements are being directed towards creating a mixed reality by back-projecting the Raman image directly onto the sample, to allow observing the chemical information with the naked eye. The reported work will contribute to bring Raman spectroscopy into the clinical environment for real-time, online surgery using augmented reality.

ACKNOWLEDGMENTS

This work was funded by the EU-project MIB (No 667933). W.Y. received a scholarship support from the China Scholarship Council.

AUTHOR BIOGRAPHIES

Please see Supporting Information online.

ORCID

Iwan W. Schie https://orcid.org/0000-0003-0336-3168

REFERENCES

[1] M. Schmitt, J. Popp, *J. Raman Spectrosc.* **2006**, *37*, 20.
[2] H. J. Butler, L. Ashton, B. Bird, G. Cinque, K. Curtis, J. Dorney, K. Esmonde-White, N. J. Fullwood, B. Gardner, P. L. Martin-Hirsch,

M. J. Walsh, M. R. McAinsh, N. Stone, F. L. Martin, *Nat. Protoc.* **2016**, *11*, 664.
[3] A. C. S. Talari, Z. Movasaghi, S. Rehman, I. ur Rehman, *Appl. Spectrosc. Rev.* **2015**, *50*, 46.
[4] E. B. Hanlon, R. Manoharan, T. W. Koo, K. E. Shafer, J. T. Motz, M. Fitzmaurice, J. R. Kramer, I. Itzkan, R. R. Dasari, M. S. Feld, *Phys. Med. Biol.* **2000**, *45*, R1.
[5] B. W. D. De Jong, T. C. B. Schut, K. Maquelin, T. Van Der Kwast, C. H. Bangma, D. J. Kok, G. J. Puppels, *Anal. Chem.* **2006**, *78*, 7761.
[6] Z. Huang, A. McWilliams, H. Lui, D. I. McLean, S. Lam, H. Zeng, *Int. J. Cancer* **2003**, *107*, 1047.
[7] C. Krafft, M. Schmitt, I. W. Schie, D. Cialla-May, C. Matthäus, T. Bocklitz, J. Popp, *Angew. Chemie Int. Ed.* **2017**, *56*, 4392.
[8] I. Anna, P. Bartosz, P. Lech, A. Halina, *Oncotarget* **2017**, *8*, 85290.
[9] E. Cordero, F. Korinth, C. Stiebing, C. Krafft, I. W. Schie, J. Popp, *Sensors (Switzerland)* **2017**, *17*, 1724.
[10] I. Latka, S. Dochow, C. Krafft, B. Dietzek, J. Popp, *Laser Photonics Rev.* **2013**, *7*, 698.
[11] C. Krafft, S. Dochow, I. Latka, B. Dietzek, J. Popp, *Biomed. Spectrosc. Imaging* **2012**, *1*, 39.
[12] H. C. McGregor, M. A. Short, A. McWilliams, T. Shaipanich, D. N. Ionescu, J. Zhao, W. Wang, G. Chen, S. Lam, H. Zeng, *J. Biophotonics* **2017**, *10*, 98.
[13] W. Wang, J. Zhao, M. Short, H. Zeng, *J. Biophotonics* **2015**, *8*, 527.
[14] H. Chen, X. Li, N. Broderick, Y. Liu, Y. Zhou, J. Han, W. Xu, *J. Biophotonics* **2018**, *11*, e201800016.
[15] K. St-Arnaud, K. Aubertin, M. Strupler, W. J. Madore, A. A. Grosset, K. Petrecca, D. Trudel, F. Leblond, *Med. Phys.* **2018**, *45*, 328.
[16] A. Lukic, S. Dochow, H. Bae, G. Matz, I. Latka, B. Messerschmidt, M. Schmitt, J. Popp, *Optica* **2017**, *4*, 496.
[17] M. N. Van Oosterom, H. G. Van Der Poel, N. Navab, C. J. H. Van De Velde, F. W. B. Van Leeuwen, *Curr. Opin. Urol.* **2018**, *28*, 205.
[18] D. Ntourakis, R. Memeo, L. Soler, J. Marescaux, D. Mutter, P. Pessaux, *World J. Surg.* **2016**, *40*, 419.
[19] J. Morita, S. Shimamura, M. Kanegae, Y. Uema, M. Takahashi, M. Inami, T. Hayashida, M. Sugimoto, in *2015 IEEE Virtual Real. Conf. VR 2015 - Proc.*, IEEE, **2015**, pp. 239–240.
[20] L. Yang, J. Wang, T. Ando, A. Kubota, H. Yamashita, I. Sakuma, T. Chiba, E. Kobayashi, *Comput. Med. Imaging Graph.* **2015**, *40*, 205.
[21] D. Gorpas, D. Ma, J. Bec, D. R. Yankelevich, L. Marcu, *IEEE Trans. Med. Imaging* **2016**, *35*, 1802.
[22] E. Upchurch, M. Isabelle, G. R. Lloyd, C. Kendall, H. Barr, *Expert Rev. Mol. Diagn.* **2018**, *18*, 245.
[23] I. P. Santos, E. M. Barroso, T. C. Bakker Schut, P. J. Caspers, C. G. F. Van Lanschot, D. H. Choi, M. F. Van Der Kamp, R. W. H. Smits, R. Van Doorn, R. M. Verdijk, et al., *Analyst* **2017**, *142*, 3025.
[24] M. J. Baker, H. J. Byrne, J. Chalmers, P. Gardner, R. Goodacre, A. Henderson, S. G. Kazarian, F. L. Martin, J. Moger, N. Stone, J. Sulé-Suso, *Analyst* **2018**, *143*, 1735.
[25] C. H. Tseng, J. F. Ford, C. K. Mann, T. J. Vickers, *Appl. Spectrosc.* **1993**, *47*, 1808.
[26] M. Fryling, C. J. Frank, R. L. Mccreery, *Appl. Spectrosc.* **1993**, *47*, 1965.
[27] S.-J. Baek, A. Park, Y.-J. Ahn, J. Choo, *Analyst* **2015**, *140*, 250.
[28] P. H. C. Eilers, *Anal. Chem.* **2003**, *75*, 3631.
[29] I. W. Schie, L. Nolte, T. L. Pedersen, Z. Smith, J. Wu, I. Yahiatène, J. W. Newman, T. Huser, *Analyst* **2013**, *138*, 6662.

SUPPORTING INFORMATION

Additional supporting information may be found online in the Supporting Information section at the end of this article.

How to cite this article: Yang W, Mondol AS, Stiebing C, Marcu L, Popp J, Schie IW. Raman ChemLighter: Fiber optic Raman probe imaging in combination with augmented chemical reality. *J. Biophotonics*. 2019;e201800447. https://doi.org/10.1002/jbio.201800447

7.3 [WY 3]

Real-time molecular imaging of near-surface tissue using Raman spectroscopy

Wei Yang, Florian Knorr, Ines Latka, Matthias Vogt, Günther O. Hofmann, Jürgen Popp, and Iwan W. Schie

Light: Science & Applications, **11**, 90 (2022)
DOI: 10.1038/s41377-022-00773-0

Der Nachdruck der folgenden Publikation erscheint mit freundlicher Genehmigung von Springer Nature

Erklärung zu den Eigenanteile der Promovend sowie weitere Doktoranden / Doktorandinnen als Koautoren an den Publikationen und Zweitpublikationsrechten bei einer kumulativen Dissertation.

Doktoranden	Wei Yang
Konzeption des Forschungsansatzes	X
Planung der Untersuchungen	X
Datenerhebung	X
Datenanalyse und –interpretation	X
Schreiben des Manuskripts	X
Vorschlag Anrechnung Publikationsäquivalente	1,0

Yang et al. *Light: Science & Applications* (2022)11:90
https://doi.org/10.1038/s41377-022-00773-0

Official journal of the CIOMP 2047-7538
www.nature.com/lsa

ARTICLE Open Access

Real-time molecular imaging of near-surface tissue using Raman spectroscopy

Wei Yang[1], Florian Knorr[1], Ines Latka[1], Matthias Vogt[2], Gunther O. Hofmann[2], Jürgen Popp[1,3] and Iwan W. Schie[1,4]✉

Abstract

The steady progress in medical diagnosis and treatment of diseases largely hinges on the steady development and improvement of modern imaging modalities. Raman spectroscopy has attracted increasing attention for clinical applications as it is label-free, non-invasive, and delivers molecular fingerprinting information of a sample. In combination with fiber optic probes, it also allows easy access to different body parts of a patient. However, image acquisition with fiber optic probes is currently not possible. Here, we introduce a fiber optic probe-based Raman imaging system for the real-time molecular virtual reality data visualization of chemical boundaries on a computer screen and the physical world. The approach is developed around a computer vision-based positional tracking system in conjunction with photometric stereo and augmented and mixed chemical reality, enabling molecular imaging and direct visualization of molecular boundaries of three-dimensional surfaces. The proposed approach achieves a spatial resolution of 0.5 mm in the transverse plane and a topology resolution of 0.6 mm, with a spectral sampling frequency of 10 Hz, and can be used to image large tissue areas in a few minutes, making it highly suitable for clinical tissue-boundary demarcation. A variety of applications on biological samples, i.e., distribution of pharmaceutical compounds, brain-tumor phantom, and various types of sarcoma have been characterized, showing that the system enables rapid and intuitive assessment of molecular boundaries.

Introduction

Methods, such as magnetic resonance imaging, computed tomography, positron-emission-tomography, and ultrasound are go-to tools that allow physicians to screen patients for cancer and localize suspicious lesions for surgical excision. These methods can also be functionalized, improving the precision for guided surgery, while allowing continuous and non-invasive monitoring of patients. In most cases, however, current imaging techniques provide information based on morphological or anatomic differences of the tissue, disregarding the underlying molecular composition. Recently, there has been a significant emphasis on Raman-based technologies for clinical in vivo applications. Raman spectroscopy is based on an inelastic scattering event between a photon and a molecule, providing the intrinsic molecular fingerprint of a sample. The advantage is that the information can be assessed label-free, without contact, and non-destructive. A number of previous studies have indicated that it is quite capable to detect and delineate cancer from healthy tissues[1–8]. However, the current implementation of fiber optic probe-based Raman spectroscopy stays well behind the technological possibilities the method can offer. To explore the potential of the method, multiple challenges have to be addressed, including imaging acquisition, sample topology, and real-time data analysis. The solution will also result in new opportunities, such as data visualization and comprehension, which will have to be explored.

For in vivo applications fiber optic probe-based Raman systems are used, because these probes are small, flexible, and allow direct access to the patient site[9–12], see

Correspondence: Iwan W. Schie (iwan.schie@leibniz-ipht.de)
[1]Leibniz Institute of Photonic Technology Jena, Albert-Einstein-Straße 9, 07745 Jena, Germany
[2]Department of Trauma, Hand and Reconstructive Surgery, University Hospital Jena, Am Klinikum 1, 07747 Jena, Germany
Full list of author information is available at the end of the article

Supplementary Table S1. Currently, Raman measurements with fiber optic probes are performed from individual locations of the sample, representing the molecular information from the respective focal volumes. Because the measurement position of a probe is not co-registered with the measurement information it is currently not possible to create an image using a handheld fiber optic Raman probe. To enable image formation, approaches using multiple optical fibers have been suggested[13]. This allows to sample multiple points at once to create a low-resolution image from a limited area but requires the application of a very large power-density on the tissues, making them less favorable for clinical translation. For large-scale imaging, a physical tracking of the probe movement to relate the positional information with the measurement location can be achieved using passively coordinated mechanical arms[14,15] and robotic arms[16]. This, however, is not only bulky but also increases unnecessarily the complexity of a system. Rather than using physical tracking, computer vision-based positional tracking approaches can provide a suitable alternative. Those operate with conventional imaging detectors to track the position of an aiming laser, avoiding complex physical instrumentations, and enabling more flexible handling, while providing positional registration with the sample[17–19].

Besides no real imaging capability for fiber optic Raman probes, current Raman systems only acquire the data but do not provide instantaneously the diagnostic information, and the collected data are analyzed post-acquisition, reducing the benefit of the method. While some implementations provide online analysis[20,21], they do so for single-point measurements and cannot be used for applications, such as tumor margins detection. However, if the acquisition of Raman images with a handheld probe was possible, the combination with real-time data processing could enable the visualization of the molecular distribution in clinical applications. This could also be favorably combined with augmented reality (AR) and mixed reality (MR) to enhance the perception of molecular information. These virtual reality (VR) approaches offer an interesting potential to improve the precision of real-time diagnosis or surgery[22] and have readily been combined with various imaging modalities, such as computed tomography[23], optical coherence tomography[24], magnetic resonance tomography[25,26], fluorescence lifetime imaging[17,19], and others[18,19,27,28].

To overcome the aforementioned challenges, we propose and experimentally demonstrate a fiber-based Raman imaging approach with real-time data analysis and combination with augmented and mixed reality on three-dimensional (3D) sample surfaces as a potential tool for real-time opto-molecular visualization of tissue boundaries for disease diagnostics and surgical resection. The reported imaging platform combines Raman spectra measurements, simultaneous computer vision-based positional tracking with real-time data processing, and real-time formation of molecular virtual reality (MVR) images. The MVR images can be perceived on the computer screen or, by additionally using a laser projector system, directly mapped on the tissue, creating MR information that can be perceived by the naked eye in real-time. Because most samples have a topological surface profile, we have additionally implemented a photometric stereo measuring system, which allows mapping the molecular information on a 3D sample surface. The presented work outlines the potential for future clinical translation of real-time Raman-based molecular imaging, by allowing easy access to patients and by providing biochemical distributions from the region of interest for disease tissue differentiation during surgical resection.

Results

Imaging of a 3D structured bio-sample surface and ex-vivo tumor tissue

To evaluate potential biomedical applications porcine cerebrum and sarcoma tissue were used to differentiate molecularly distinct regions with the proposed approach. A porcine cerebrum with dimensions of 7 cm × 4 cm × 2.6 cm was used. To simulate heterogeneous regions two areas of the cerebrum were coated with a lipid-rich and a pharmaceutical compound (N-Acetyl-4-aminophenol). The brightfield image of the prepared sample is presented in Fig. 1a and reference spectra from both compounds and the gray matter are presented in Supplementary Fig. S1. The laser power and acquisition time was set to ~100 mW and 0.1 s, respectively. The brain surface was scanned by hand with the outlined approach and in 260 s a total of 856 points were sampled, processed, and reconstructed, Fig. 1b, c. To visualize the topological distribution of molecular compounds photometric stereo was used and the non-textured height image and the textured image with the original color image are presented in Fig. 1d, e, and the molecular information mapped onto the reconstructed 3D model, Fig. 1f and gridded molecular data, Fig. 1g. The combination of the molecular information with the photometric stereo offers an intuitive and realistic view of the distribution of the chemical information on the surface in a 3D scene compared to the conventional 2D image. The 3D representation of the structured sample was recorded and displayed in individual panels of non-textured height image, original color textured image, and Raman textured image, in Supplementary Video 1a. The MR-representation is presented in Fig. 1h, i, where the users can intuitively observe the distribution of the components directly on the sample. The video recordings of the acquisition-procedure, including augmented and mixed reality visualizations can be found as Supplementary Video 1b. As shown in

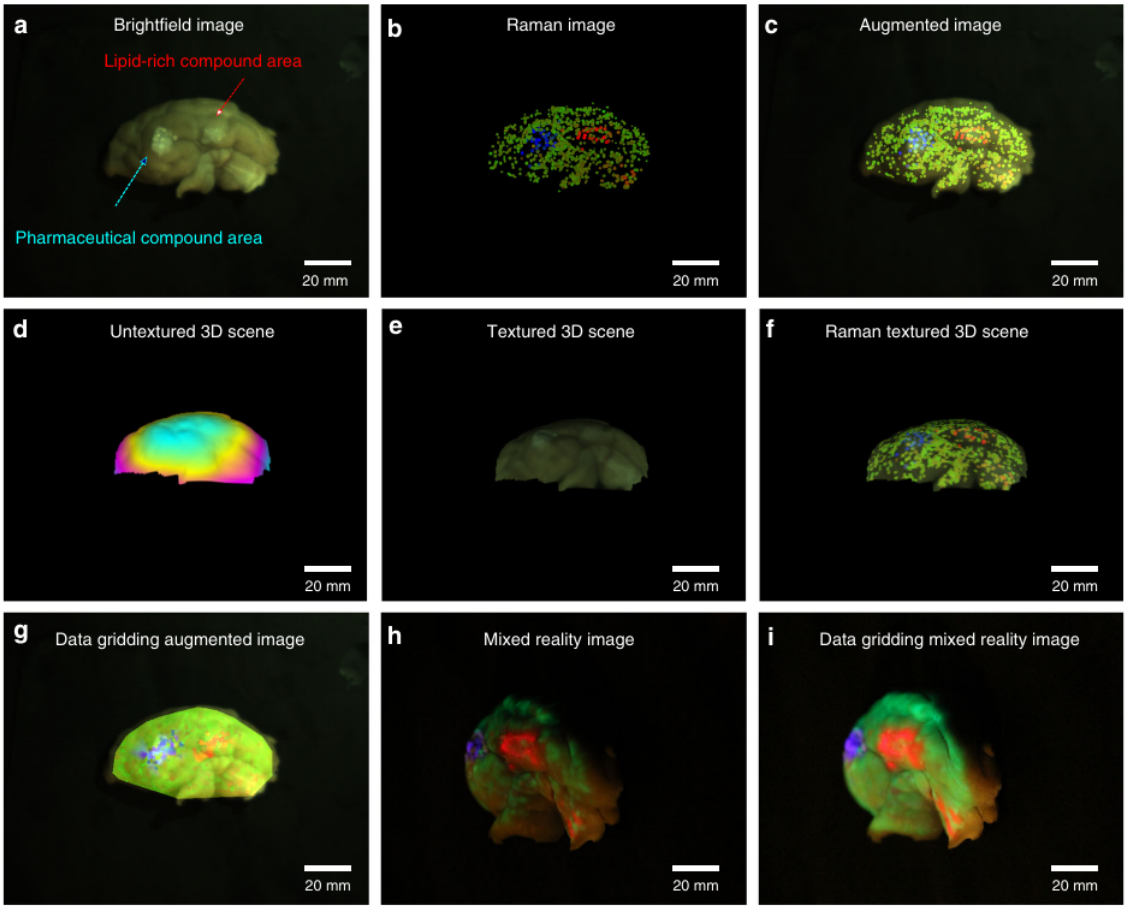

Fig. 1 Representative results of the proposed approach on a porcine brain sample. a Brightfield image of the sample, where the arrows indicate areas with a lipid-rich and pharmaceutical compound. In the brightfield image it is not only challenging to localize the regions but does not provide any possibility to differentiate between regions. **b** Reconstructed Raman image provides the molecular distribution on the sample. **c** Augmented reality image directly combines the molecular information with the brightfield scene, readily providing a differentiation between the regions. **d** The reconstructed untextured height 3D scene image of the sample employing photometric stereo and **e** as textured 3D image with the original brightfield image. **f** The height 3D scene image textured with the reconstructed Raman image, which now not only enables the two dimensional, but three dimensional visualization of the augmented molecular information. **g** Raman image after data gridding of the molecular data, forming a fully filled 3D augmented molecular image. **h** Improved and direct visualization of the mixed Raman reality image is back-projected onto the sample, so that the molecular boundaries are visible to the user. **i** Presents the results as in **h**, but with gridded data, which allows to better visualize molecular boundaries. The color information in all figures represent the different chemical components, i.e., red for the lipid-rich compound, green for gray matter on the cerebrum, and blue for the pharmaceutical compound

Supplementary Fig. S1c, the detection of very low concentrations can be challenging. While the current implementation uses compounds at a high concentration, future modifications of the optical parameters of the acquisition system will additionally improve the performance, which will enable measurements at very low concentrations.

To demonstrate the performance of the reported approach for the tumor characterization, a measurement on a freshly excised tumor sample with a size of 5.2 cm × 4.1 cm was performed. The laser power and acquisition time was set to ~100 mW and 0.1 s, respectively. By scanning the sample surface with the handheld movement of the probe a total of 994 points were acquired in 184 s, and the corresponding brightfield image, Raman image, the augmented image, and the gridded are presented in Fig. 2a–d, respectively, showing distinct molecular boundaries within the pathological tissue. The reference spectra can be found in Supplementary Fig. S2. Using the mixed reality visualization method, the molecular information was projected on the sample surface and recorded with an external DSLR camera (digital single-lens reflex camera, EOS 1200D, Canon, Japan), Fig. 2f, g. Due to an increase of sample transparency, the mixed Raman reality was not real-time updated, but only the final molecular

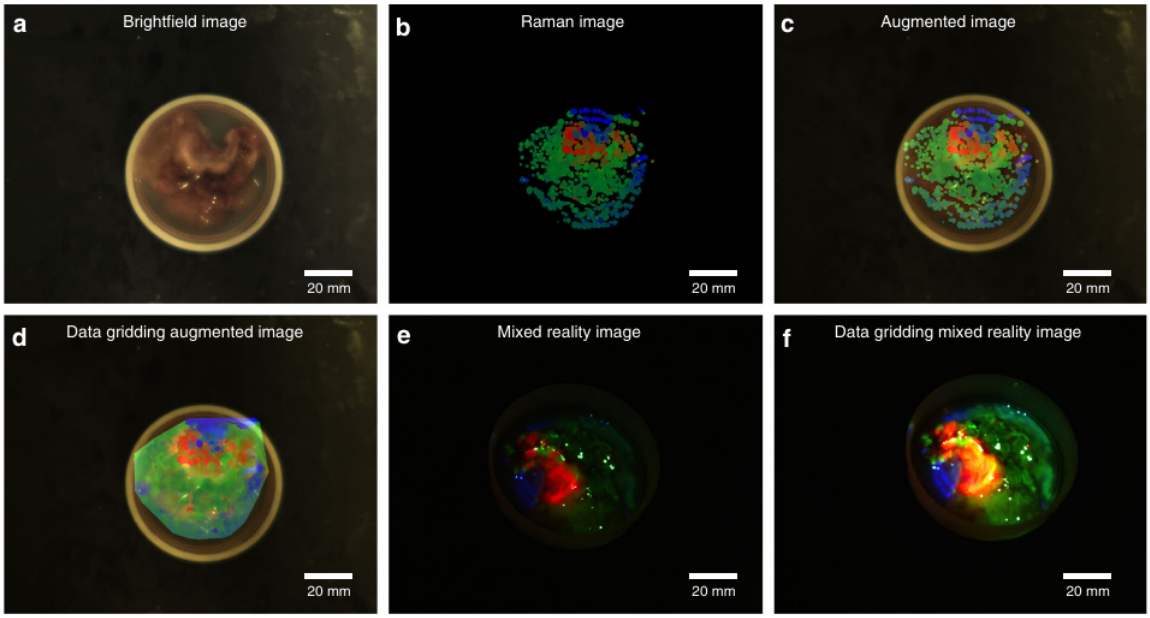

Fig. 2 Representative results of the proposed approach on the ex-vivo clinical sample. a Brightfield image of the sample does not allow to differentiate between different molecular regions. **b** Raman imaging with the presented approach readily enables the visualization of distinct molecular locations. **c** The augmentation of the molecular information with the brightfield image provides distinct differentiation of the information of the sample. **d** Data gridding of molecular information and augmented overlay with brightfield image. **e** Mixed Raman reality image enabled through projection the direct visualization of the molecular information in the sample plane; and, in combination with data gridding (**f**), provides a rich image with molecular distinct boundaries. The color information represents the different chemical components, i.e., red for collagen, green for epithelial tissue, and blue for the plastic sample holder

image projected on the sample. The video of the whole procedure of the Raman reconstruction with the augmented method can be found in Supplementary Video 2. Additionally, measurements on ex vivo cancer lipoma tissue and the results can be found in Supplementary information of Fig. S3 and Video S1. In all examples the presented implementation is able to differentiate between various biomedical components during the data acquisition process, resulting in a real-time assessment of the macromolecular distribution of the sample, opening new potentials for image-guided in-vivo disease diagnostics and surgical resection.

Data-flow and diagram

The data flow and diagram of the implementation are presented in Fig. 3, where the first part focuses on parallel running spectral acquisition and simultaneous positional tracking, while the second part on the topographic reconstruction, real-time Raman-data analysis, and the molecular visualization using AR and MR. In AR the molecular information is mapped on the brightfield image or a 3D surface model formed by the photometric stereo method on the computer screen. In MR the molecular information is projected on the sample. In our implementation we register the projected image with the sample in the following way:

Block 1: As described in ref. [18], a handheld fiber-optic Raman probe is used to acquire Raman spectra. First, a database of reference spectra from the relevant components of the sample is built. For bio-sample, this database contains Raman spectra of basic molecular components, such as lipid, bone, protein, collagen, and so on. Additional reference-spectra can be added to the database by sparse Raman sampling on the target sample. Each newly acquired spectrum is baseline corrected, using an ALS (alternating least squares) -based background estimation and normalized to unity[29]. The corrected and normalized spectra are then fitted using the database-spectra by non-negatively constrained least squares fitting[30]:

$$\mathbf{s} = \mathbf{P}\mathbf{c} + \varepsilon \tag{1}$$

where $\mathbf{s}$ is an acquired spectrum, $\mathbf{P}$ is the database spectra, $\mathbf{c}$ a coefficient vector with the length of the vector equals the number of spectra in the components database, representing the relative concentration of the components and ε is the error of the measurement. By solving the equation under the non-negativity constrain for the

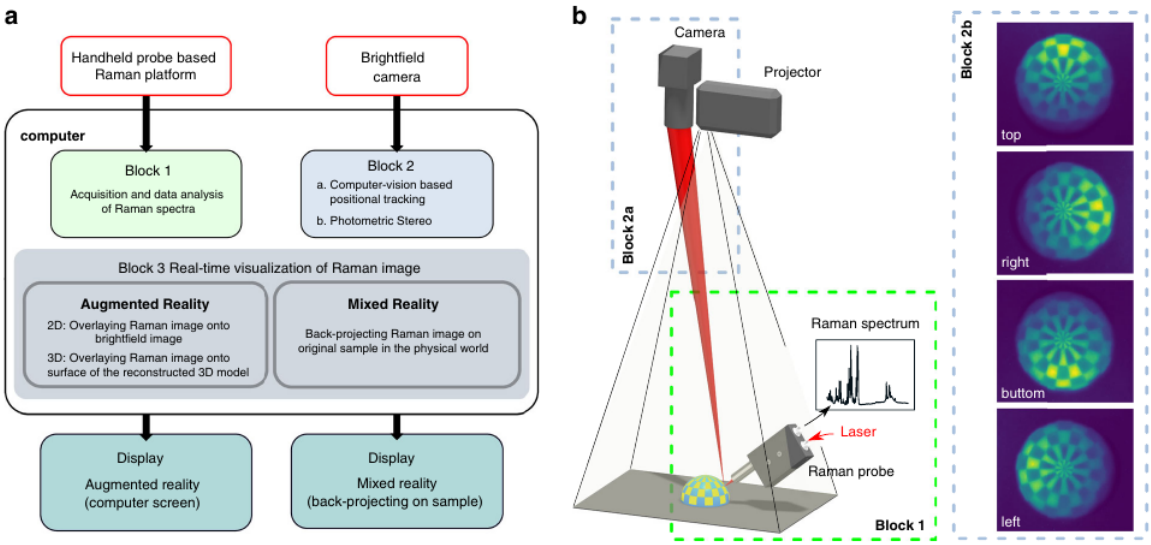

Fig. 3 Data-flow (a) and diagram (b) of the developed approach. Raman spectra are acquired with a handheld Raman probe (Block 1) and positional information where the spectra were acquired is determined in parallel through a brightfield camera (Block 2a). The Raman spectra are processed in real-time and combined with the positional information to reconstruct the Raman image, forming the molecular virtual reality visualization of the molecular distribution. Furthermore, a computer vision-based 3D surface reconstruction method (Block 2b), i.e., photometric stereo, is used to construct a 3D height map of the sample surface, allowing to overlay the reconstructed Raman image on the 3D map for a 3D visualization of the molecular composition

coefficient values, the vector result **c** is used to construct molecular concentration maps for the database spectra.

Block 2: a. During the Raman measurement, the brightfield camera video-stream is used to identify the current measurement location through the analysis of the excitation laser point generated by Rayleigh scattered light. The image processing is based on color-segmentation, thresholding, and ellipse fitting during the measurement. It should be pointed out that the threshold in this step cannot only ensure that the bright beam generated by the Rayleigh scattered light is retained, but also helps to avoid a certain degree of defocused measurement. Because in case of the strong defocusing, the intensity of the laser beam will be too low for the intensity threshold, resulting in failure of subsequent ellipse fitting and the measurement is discarded. If the fitting is successful, the parameters of the fitted ellipse, i.e., center, and minor radius are used for Raman image reconstruction. **b**. Photometric stereo, based on four light sources, is integrated into the reported approach to reconstruct the 3D surface of a sample. This method is applied prior to the Raman measurements to build a 3D surface model of the sample, which is then used to map the extracted molecular distribution on the 3D model of the sample.

Block 3: The next steps concern the visualization of the Raman information, both as augmented and as mixed reality. For each new frame, a circle with an auto-scalable diameter is computed in the 8-bit intensity image of each known components plane. The center point of the circle is equal to the center point determined by laser tracking (Block 2), whereas the concentration coefficient is determined by the non-negative estimation (Block 1). The scalable diameter (*d*) of the circle is determined by the minor radius (*r*) of the fitted ellipse and the Euclidian distance (*D*) between the center of the current fitting ellipse and the one from the previous frame as the following rule:

$$d = \begin{cases} 0.5r, & \text{if } D < r \\ r, & \text{if } r \leq D < 2r \\ 2r, & \text{else} \end{cases} \tag{2}$$

For each element of the database, an image plane is updated according to:

$$I^{k}_{x,y} = \frac{\sum c^{k}_{x,y}}{N_{x,y}} / c_{max} \times 255 \tag{3}$$

where for the image plane of the *k*th component, at the pixel location (*x*, *y*), the intensity $I^{k}_{x,y}$ is determined by the mean value of the relevant non-negative estimation result $\frac{\sum c^{k}_{x,y}}{N_{x,y}}$. Here, $N_{x,y}$ is the number of measurements at the pixel (*x*, *y*), which is then normalized to the maximum value of all the fitting result c_{max}, and rescaled into an 8-bit (0–255) scale. Additionally, a data gridding function,

using the triangulation-based nearest-neighbor interpolation method can be used[31]. This method is applied to individual 8-bit intensity images of component planes and spatially interpolates randomly distributed data points over a uniform grid. Here, the grid size is set to the image resolution and can be adjusted as needed. At last, an RGB-image is displayed by merging the three pseudo-color planes. Because the Raman image is reconstructed on the same dimensional space as the brightfield image, it is easy and convenient to overlay the molecular distribution on the brightfield image to display the augmented chemical reality on the computer screen in real-time. This overlay can be performed with both 2D and 3D models, whichever is most appropriate for the current sample.

To overcome the need to change viewing directions during surgery is the use of mixed reality. We additionally implemented spatial mixed reality by projecting the molecular information in real-time during the acquisition onto the tissue, using a small-size laser projector (BML100PI, Bosch, Germany). In order to avoid disturbances of the laser tracking, the intensity of the projected image is reduced by adjusting the transparency.

Characterizing the instrumentation

3D reconstruction

Because in most relevant clinical applications the sample has a topographic profile, we have added photometric stereo to the implementation. To characterize the combination of the proposed Raman imaging approach with the photometric stereo method, a hemisphere phantom was designed and fabricated by 3D printing of Poly (methyl methacrylate) (PMMA), which has slices of every 20° from the center on the horizontal plane and vertical plane, respectively, Fig. 4a$_1$. Relevant parameters can be found in the top-view, Fig. 4a$_2$, and three-quarter view, Fig. 4a$_3$. The basic implementation of the proposed Raman imaging method only allows the reconstruction of information from 2D surfaces, meaning that the information of the present phantom is a projection of the topography to the camera plane, resulting in a compression of the individual points at lower heights, Fig. 4a$_2$. The laser power and acquisition time was set to ~100 mW and 0.1 s, respectively. The results for the molecular imaging without the topographic assessment are presented for the brightfield image, Raman image, and augmented Raman image in Fig. 4b$_{1-3}$, resulting in deviations for tiles lengths located closer to the equator. To reduce these deviations photometric stereo was implemented on the same system, allowing to determine the topological height information and enabling to establish the molecular and height information and a 3D visualization of the molecular signatures. The 3D-surface model of the hemisphere phantom, Supplemental Fig. S4, shows a root-mean-square error (RMSE) and normalized root mean square error (NRMSE) between reconstructed height map and real height map of ~11.9 pixels for ~2.8 mm, corresponding to 0.24 mm/pixel and 10.6%, respectively. The reconstructed 3D image of the hemisphere phantom is shown in Fig. 4c$_1$ and Fig. 4c$_2$ with the untextured height scene and textured scene with the brightfield image. The untextured height scene is formed through a mapping of the height information into a CMY (cyan, magenta, and yellow) color scale, while the textured scene was formed by mapping the brightfield image on the height 3D model according to the corresponding pixel coordinates. Because the brightfield image is correlated with the acquired Raman information it is straightforward to map the molecular information on the 3D-surface, forming AR images, Fig. 4c$_3$, c$_4$. A video showing the 3D view representation of these images, Fig. 4c$_{1-4}$, is found as Supplementary Video 3.

Because the homographic relationship can only be applied for two planar surfaces, the representation of the mixed chemical reality of the projection of the Raman image on the 3D surface would result in distortions between the projection and the original surface, Fig. 5a. For the phantom sample, taking the section of $Y = 0$ into account, c_0 and p_0 represent the position of the camera and projector, respectively. Here, the horizontal distance between camera and projector is fixed to 1 cm, where c_1 and c_2 are the tangent points from c_0 to the phantom, and the cone spanned by these lines represents the FOV of the camera on the phantom. c_1' and c_2' are the foot of the perpendicular from c_1 and c_2 to X-axis. If the camera-projector calibration is based on the surface at $Z = 0$, c_1' and c_2' would be the projected points for c_1 and c_2. Thus, the projection points would be distorted, i.e., from c_1 and c_2 to p_1 and p_2, which are the intersections of the segments of p_0 to c_1' and p_0 to c_2' with the phantom, respectively. Exemplary, Fig. 5a, b show the situation for camera/projector distances to the sample of 4 cm and of 40 cm, respectively. The subimage is the zoom of the small black-dashed box to show the details for Fig. 5b. Based on this simulation, a plot of height in the Z-axis vs. the distance between c_1 to p_1 (black curve) and c_2 to p_2 (red curve) is shown in Fig. 5c. The distortions decrease with increasing height, if the thickness of the sample is fixed. For the current implementation, the height of the camera and projector to the sample was set to 40 cm, resulting in distortions between approx. 0.23 and 0.06 cm. Figure 5d, e show the photographs of the hemisphere phantom and mixed Raman reality by projecting the Raman image on the phantom. Since the PMMA is relatively transparent, the red color overlay is not obvious. The result also shows that the experimental distortions agree with the theoretical simulation, which indicates the distortions could be minimalized by increasing the ratio between the height of the projector (camera) and the thickness of the sample.

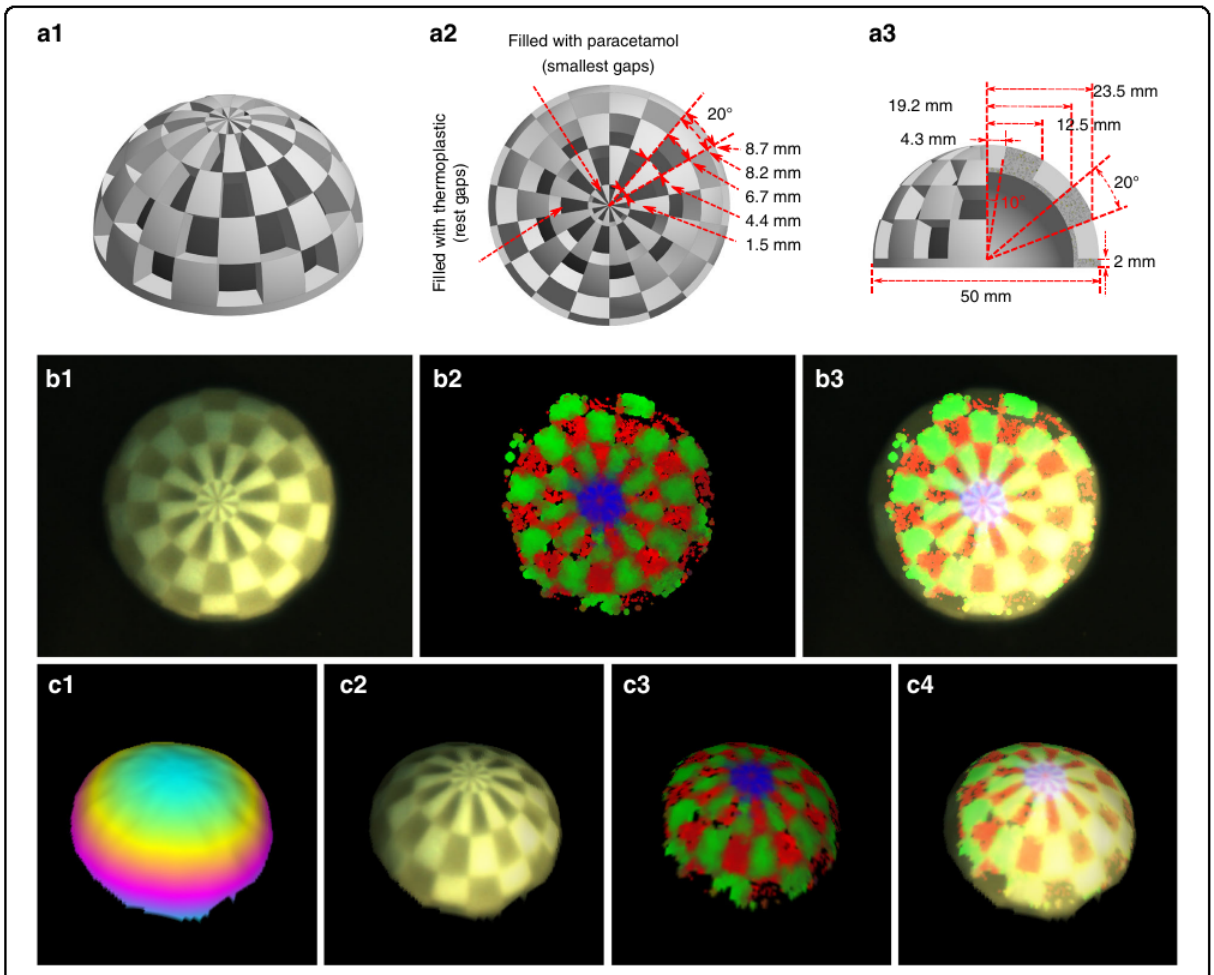

Fig. 4 Combination with the photometric stereo. a_1 Diagram of the PMMA hemisphere phantom with 20°-slices from the center on the horizontal plane and vertical plane. The spaced area on the top surface is hollowed and the small gaps refilled with paracetamol, while the remaining gaps are filled with moldable thermoplastic (polycaprolactone). **a_2** Top-view of the phantom, which shows the arc lengths of a 20° slice on each horizontal level. **a_3** Three-quarter side-view of the phantom, which shows the radiuses of each horizontal level. The diameter of the hemisphere is 50 mm and the thickness of the basement is 2 mm. **b_{1-3}** Top-view on the sample. **b_1** Brightfield image of the hemisphere phantom, where no molecular boundaries can be discerned. **b_2** Reconstructed Raman image by the developed imaging approach with the handheld operation with clear molecular boundaries, and **b_3** overlayed with the brightfield image as augmented molecular information. **c_1** A representative image of the height map of the phantom through photometric stereo. **c_2** The brightfield image textured height map, viewed from the same angle, and **c_3** with relevant molecular-textured 3D image. **c_4** The three modes combined and represented as 3D augmented molecular image. The color information represents the different chemical components, i.e., red for PMMA, green for thermoplastic (polycaprolactone), and blue for paracetamol

Spatial resolution

The auto-scale diameter rule of Eq. (2) was characterized to demonstrate the relationship between the spatial resolution of the Raman imaging system with the speed of the probe movement and the diameter of the reconstructed circle. Theoretically, the spatial resolution of the system is defined by the spatial resolution of the brightfield camera and the size of the laser spot. Here, the resolution of the brightfield camera is set to 640 × 512 pixels, and the field of view is approx. 156 mm × 125 mm, resulting in approx. 0.24 mm per pixel. The focal spot diameter of the laser is close to 105 µm, as in the fiber optic probe the excitation fiber with a core diameter of 105 µm is imaged by the optical system with a 1:1 magnification. As such, only the resolution of the brightfield camera and motion speed of the probe limits the resolution of the system. The projector used for the MR has a format of 854 × 480 pixels, which is similar to the one of the brightfield camera. However, for each frame, the reconstruction of the Raman image is based on the scalable circle, which is related to the minor radius of the fitted ellipse as mentioned above. The ellipse fitting method requires at least five points to

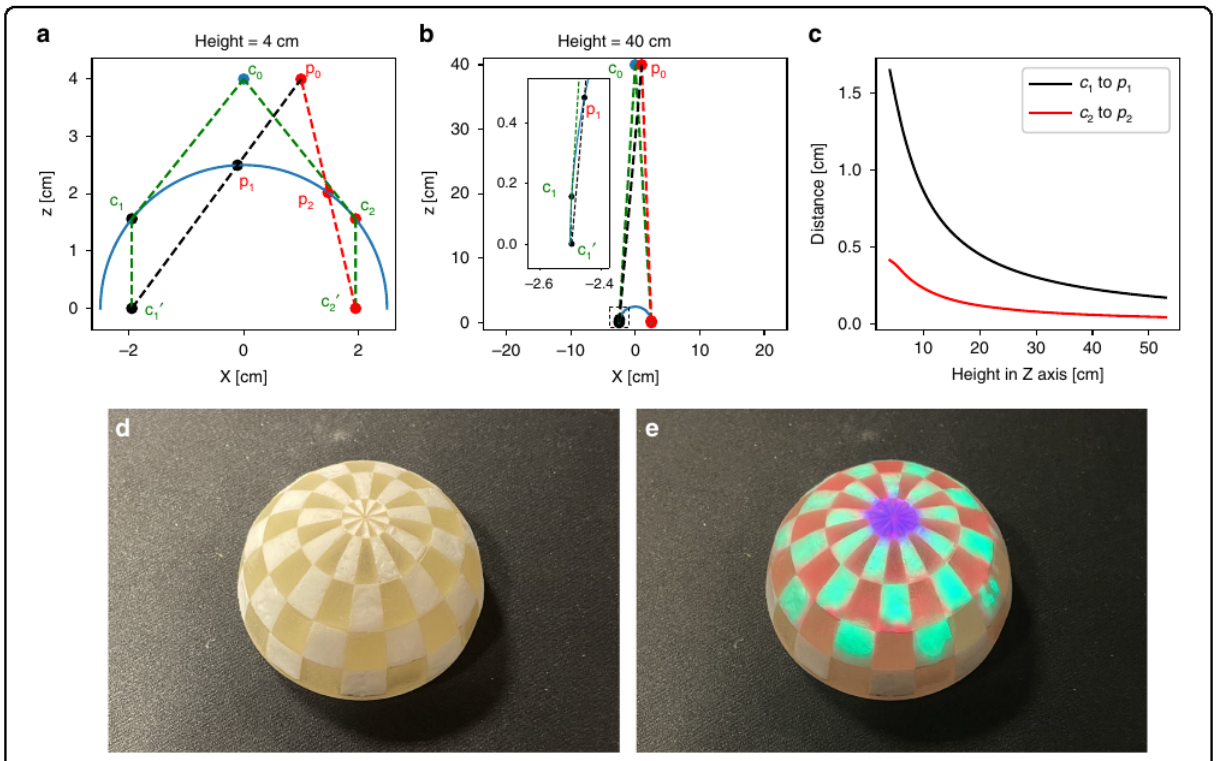

Fig. 5 Characterization of the performance of mixed Raman reality for the hemisphere phantom. a Schematic diagram for the implementing of mixed Raman reality with the hemisphere phantom. Here, taking the section of $Y = 0$ into account, c_0 and p_0 represent the position of camera and projector, respectively. The horizontal distance between them is fixed to 1 cm. c_1 and c_2 are the tangent points from c_0 to the phantom. c_1' and c_2' is the base perpendicular from c_1 and c_2 at $Z = 0$ axis. p_1 and p_2 are the intersections of the hemisphere with the segments of p_0 to c_1' and p_0 to c_2'. **b** Same consideration for the arrangement, but at a height of 40 cm, where the subimage is the zoom-in of the small black-dashed box. **c** Height plot in Z axis vs. the distance between c_1 to p_1 (black curve) and c_2 to p_2 (red curve). **d** Photograph of the hemisphere phantom; and **e** photograph of the mixed molecular reality image by projecting the molecular image on the phantom. The color information represents the different chemical components, i.e., red for PMMA, green for thermoplastic (polycaprolactone), and blue for paracetamol

perform the fitting[32], i.e., at least a diameter of two pixels for the fit. The reconstruction requires minimal ±1 pixel surrounding the center position to draw the constructed circle, which sets the diameter of the reconstructed circle to at least two pixels. Thus, the theoretic spatial resolution of the whole system is approx. 0.5 mm in x-direction and y-direction. To assess these considerations a molecular sensitive spatial resolution target with stripes of different widths was designed and 3D printed, Fig. 6a. The widths of stripes and grooves vary from 0.5 mm to 5 mm. The molecular sensitive spatial resolution target is made of PMMA and the grooves between stripes are filled with moldable thermoplastic, i.e., polycaprolactone for gaps >1 mm and powdery paracetamol for gaps ≤1 mm. The Raman spectra of these three components are plotted as Fig. 6b, which were used as the database for the data evaluation. Pseudo colors were assigned to the individual components, i.e., red for PMMA, green for thermoplastic, and blue for paracetamol. Figure 6c shows the reference brightfield image of the resolution target and an indicator of the ellipse-fitted laser spot. To demonstrate the influence of the moving speed of the probe, a translation stage (MLS203–1, Thorlabs, Austin, Texas) was used. The probe was attached at a slight angle to ensure that the laser spot is not obscured. The speed of the stage was set to 2 mm/s, 5 mm/s, and 10 mm/s, respectively. The distance between probe and sample was to the focal distance of 8 mm. Also, a handheld operation for the probe movement was performed for comparison. For these measurements, the laser power and the acquisition time were set to 100 mW and 0.1 s, respectively. The images of visualization by AR method for 2, 5, and 10 mm/s and consequently different reconstructed circle diameters are shown as Supplemental Fig. S5. The reconstructed Raman image fits the known distribution and spacing of molecular compounds. To better visualize these details a region of interest (ROI), indicated by the red dashed box in Fig. 6c, was selected. Images were cropped and are presented in Supplemental Fig. S6, which shows that a small diameter of the reconstructed circle at a high speed of movement may lead to a

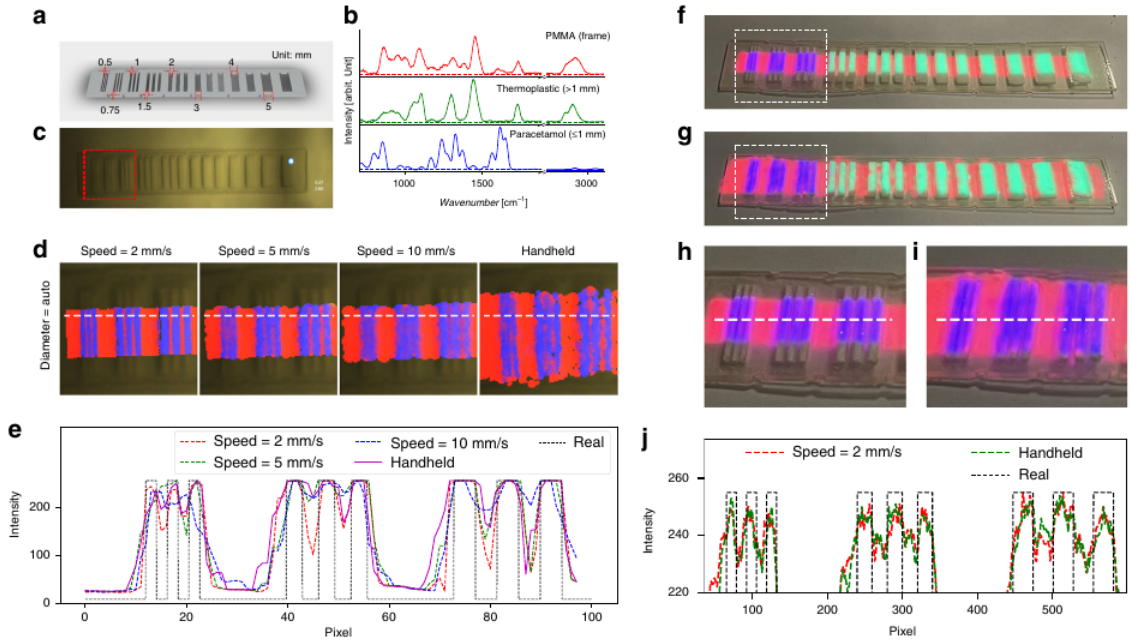

Fig. 6 Evaluation of the spatial resolution of the developed approach. a Diagram of the spatial resolution target with stripes of various widths. The gaps between the stripes are filled with moldable thermoplastic (polycaprolactone) and paracetamol powder for gaps >1 mm and ≤1 mm, respectively. **b** Raman spectra of the relevant three components are color-coded, i.e., red for PMMA, green for thermoplastic, and blue for paracetamol. **c** Brightfield image of the spatial resolution target and an indicator of the ellipse fitted laser spot with positional information. The red dashed box indicates the ROI for imaging cropping. **d** The cropped augmented Raman images in the ROI of the auto-scale reconstructed diameter of the circles by moving probe at various speeds or handheld operation. The white dashed line on each image indicates the line for profile analysis. **e** The plots of the blue path (paracetamol plane) of the lines profile from the individual augmented Raman images. The black dashed line indicates the real region of the gaps filled with paracetamol. **f** Photograph of the mixed Raman reality result by projecting the molecular image reconstructed for the speed moving speed of 2 mm/s and the auto-scale diameter condition; and **g** for handheld operation. The white dashed boxes in the images indicate the ROI shown in detail in **h** and **i** and the corresponding intensity profiles of the dashed white line are presented in **j**. The real curve (black) indicates the gaps where the paracetamol is filled in

sparse image, while the big diameter may result in a too smooth image with a decreased spatial resolution. The results show that the auto-scale rule, Eq. (2), can improve visual perception by dynamically adjusting the reconstructed diameter according to the moving speed. To demonstrate the details of the auto-scale results, the relevant cropped images with various moving speeds and the handheld operation by auto-scaling reconstructed diameters are presented in Fig. 6d. To visualize the contrast between the molecular components the intensity profile along the horizontal line (white dashed line) for the paracetamol (blue) plane on the individual images was plotted for different motion speeds, Fig. 6e. These images and the plots demonstrate that the auto-scale reconstruction strategy can strike a balance between the speed of the probe movement, and the quality of the reconstructed Raman image. It allows coarse-mapping at a higher speed to cover a larger image area, but reduced resolution and fine-mapping at low speed to acquire high resolution, especially benefiting the handheld operation. The plot also shows that the experimental spatial resolution agrees with the theoretical analysis. This means that a spatial resolution of approx. 0.5 mm can be achieved. The spatial resolution was also investigated for MR, by back projecting the reconstructed Raman image on the resolution target. However, beforehand the projector-camera was calibrated to establish the homographic relationship between the projector and the camera, i.e., the projective transformations between the camera plane and the projector plane, using a checkerboard. For details see supplementary information Figs. S7 and S8. With this calibration, the spatial mismatch error is around 0.3% or 1.5 pixels. Here, representative results of the movement speed of probe at 2 mm/s and handheld operation, both with auto-scale reconstructed circles were projected on the original resolution target, respectively, and photographed by the external DSLR camera, see Fig. 6f, g. The white dashed boxes in the photographs indicate the ROI which forms Fig. 6h, i, respectively. Figure 6j shows the horizontal line profiles of the paracetamol (blue) plane of

the white-dashed lines on Fig. 6h, i with red-dashed curve and green-dashed curve, respectively. The real (black-dashed) curve represents the gap area where the paracetamol is filled in. The plot demonstrates that the mixed reality visualization has the same positional accuracy and spatial resolution as augmented reality. The achievable spatial resolution is comparable with conventional medical imaging methods, e.g., CT and MRI[33,34], and should be suitable for the scenario as an image-guidance instrument for clinical applications. The spatial resolution could be improved with a higher resolution brightfield camera and smaller laser spot. In return, this would increase the measurement time for the same fill factor. The current parameters are a compromise between the time consumption for covering a sufficiently large area and suitable image quality.

Discussion

Our proposed and experimentally demonstrated fiber-optic probe-based imaging system enables the non-destructive acquisition of molecular images from a large tissue sample label-free. To overcome the current disadvantage of conventional Raman systems, we have directly implemented the data-processing engine into the acquisition flow, enabling the evaluation of complex biochemical macromolecules Raman signatures in real-time and visualization molecular virtual reality, i.e., augmented reality and mixed reality. Additionally, for the application to 3D surfaces, an assessment of the topography through photometric stereo was implemented, allowing the mapping of the reconstructed molecular information on the 3D model of the sample. In the current configuration, the system achieves a spatial resolution of 0.5 mm, which is already below the typical excision precision of a surgical procedure, Fig. 3. Depending on the particular application acquisition and mapping frequency of 10 Hz can be achieved for excitation powers, which are below the minimally permittable exposure (MPE) value for radiation of for a 785 nm excitation, i.e., approx. 159 mW for 1 s, making this quite feasible for clinical translation. The photometric stereo can be determined with a normalized root-mean-square error (NRMSE) of only 3.3% in depth, corresponding to less than 1 mm in depth, also showing compatibility for clinical translation. The characterization of augmented reality and mixed reality on the resolution target and the hemisphere phantom for the situation of flat sample and 3D structure sample, show that depth distortions can be as low as 0.6 mm for a projector to sample distance of 40 cm. The application to the biological tissue phantom has shown the distinct differentiation of the molecular margins between the distribution of a lipid-rich and pharmaceutical compound on a 3D-structured porcine cerebrum. Through the implementation of photometric stereo, it is possible to precisely determine the distribution of the molecular composition on the tissue, enabling evaluation of the position of molecular margins and the analysis of two ex-vivo biopsy samples, breast cancer, and lipoma. Future improvements of the system will aim at a more precise probe movement and control of the sample to probe distance, i.e., combination with a rapid and accurate autofocus unit[35]. Additionally, we envision the combination or the translation to other optical modalities, such as optical coherence tomography (OCT), hyperspectral imaging, second harmonic generation (SHG), and others for improved biomarker analysis. This presented work outlines the potential for future clinical translation of real-time Raman-based molecular imaging, by allowing easy access to patients and providing biochemical distributions from the region of interest for tissue differentiation during surgical resection.

Materials and methods

Raman setup

The handheld fiber-optic Raman probe, as described in our previous report[18], is a coaxial, dual fiber handheld probe. The excitation laser is fiber-coupled into the probe through a multi-mode fiber with 105 µm core diameter, passes through a 785 nm bandpass filter to remove the silica Raman background from the excitation fiber, then through a dichroic mirror and is focused at the sample plane through an objective lens, with a working distance of 7.5 mm and a numerical aperture (NA) of 0.22, see Supp. Fig. S9. The outline of the probe can be found in the supplementary materials. The generated Raman signal is collected by the same objective lens, passes through a long-pass filter to remove the Rayleigh scattering signal, is fiber-coupled into a 200 µm fiber, which is also used as the entrance aperture of the spectrometer (Acton LS 785; Princeton Instruments, Trenton, New Jersey). The spectrometer is equipped with a back-illuminated deep depletion charged coupled device (CCD, PIXIS-400-BReXcelon; Princeton Instruments Trenton, New Jersey). A 785 nm laser with maximum output power about of 300 mW (FERGIE-785 nm laser; Princeton Instruments, Trenton, New Jersey) is used for the excitation. Taking the parameters of the diameter of the fiber, the wavelength of the laser, the grating of 830 g/mm and the type of the spectrometer into account for grating dispersion calculation, the setup has a spectral resolution of ~2.2 nm, i.e., 24 cm^{-1}. The typical output laser power and acquisition time in the report was ~100 mW and 0.1 s, respectively.

Computer vision-based positional tracking of the laser beam spot

During the acquisition, the Rayleigh scattering of excitation laser is used for positional tracking. The positional

tracking method of this study has been described in detail in our previous work of ref. [18]. In this paper, a CMOS (complementary metal-oxide-semiconductor) camera (DCC1645C; Thorlabs, Austin, Texas) replaces the conventional webcam as it has a 650 nm short-pass filter to decrease the influence of high-intensity Rayleigh scattering, which can artificially increase the detection area, decreasing the accuracy of the positional tracking. The resolution of the camera was set to 640 × 512 pixels. Briefly, in the image processing algorithm, a single plane is extracted from the color brightfield RGB image, followed by intensity thresholding. The contour of the spot is extracted by a Laplacian filter, and an ellipse contour fitting function is used to determine the center and size of the laser spot. The fitted parameters of center and size are used for Raman image reconstruction.

Photometric stereo

Photometric stereo is used for 3D surface reconstruction and is based on estimating the surface normal by multiple conventional two-dimensional (2D) images under different illumination directions. Here, a four source photometric stereo approach[36–38] was applied, allowing the acquisition of four 2D images under four different illumination orientations from the top, right, bottom, and left, respectively. The camera for the acquisition is identical to the one for positional tracking. Four light-emitting diodes, which are set surrounding the camera with distances of 15 cm were controlled by a multifunction I/O device (USB6001; National Instruments, Austin, Texas). The intensity value of the same pixel from these four 2D images, I_n, are determined by the surface normal $\boldsymbol{N}$, the albedo (reflectivity) k and coordinates of four different illuminations, L_n, following the equation[39]:

$$I_{\boldsymbol{n}} = k_d(\boldsymbol{L_n} \cdot \boldsymbol{N}) \tag{4}$$

Solving for $k_d\boldsymbol{N}$, i.e., $k_d\boldsymbol{N} = \left(\boldsymbol{L}_n^T\boldsymbol{L}_n\right)^{-1}\boldsymbol{L}_n^T I_n$, where $\boldsymbol{N}$ is a unit vector, and the albedo k_d can be estimated as the length of this vector. With the known coordinates of the four illuminations and acquired four 2D images, the surface normal $\boldsymbol{N}$ of each pixel can be calculated, and the gradient of each pixel can be approximated as follows:

$$G_{x,y} = \left(\frac{N_x}{N_z}, \frac{N_y}{N_z}\right) \tag{5}$$

Last, the surface height map, i.e., the shape, can be iteratively approximated from a manually set start point, e.g., the center position, to the outermost pixels by integration based on the gradients between adjacent pixels.

Fixed porcine brain sample

The porcine brain was ordered from a normal butcher shop and was isolated and fixed in 4% PFA in PBS solution overnight at 4 °C. The fixed porcine brain sample was used for the experiment after rinsing with distilled water.

Ex-vivo tumor sample

The ex-vivo tumor samples were the center part of the biopsy resection during tumor removal surgery of muscle-skeletal sarcoma. The surrounding part which may contain conjunction part of health and tumor tissue was kept for histologic analysis. The experiment protocol was approved by Jena University, Ethik Votum 2018–115.s8.

Acknowledgements
This work was funded by the ERA-CVD project MultiFib (01KL1904) and W.Y. received scholarship support from the China Scholarship Council.

Author details
[1]Leibniz Institute of Photonic Technology Jena, Albert-Einstein-Straße 9, 07745 Jena, Germany. [2]Department of Trauma, Hand and Reconstructive Surgery, University Hospital Jena, Am Klinikum 1, 07747 Jena, Germany. [3]Institute of Physical Chemistry and Abbe Center of Photonics, Friedrich-Schiller University Jena, Helmholtzweg 4, 07743 Jena, Germany. [4]Department of Medical Engineering and Biotechnology, University of Applied Sciences - Jena, Carl-Zeiss-Promenade 2, 07745 Jena, Germany

Funding
Open Access funding enabled and organized by Projekt DEAL.

Data availability
The datasets acquired for this study are available from the corresponding authors upon reasonable request.

Conflict of interest
The authors declare no competing interests.

Supplementary information The online version contains supplementary material available at https://doi.org/10.1038/s41377-022-00773-0.

Received: 30 September 2021 Revised: 9 March 2022 Accepted: 19 March 2022
Published online: 08 April 2022

References

1. Cordero, E. et al. In-vivo Raman spectroscopy: from basics to applications. *J. Biomed. Opt.* **23**, 071210 (2018).
2. Krafft, C. et al. Label-free molecular imaging of biological cells and tissues by linear and nonlinear Raman spectroscopic approaches. *Angew. Chem. Int. Ed.* **56**, 4392–4430 (2017).
3. Upchurch, E. et al. An update on the use of Raman spectroscopy in molecular cancer diagnostics: current challenges and further prospects. *Expert Rev. Mol. Diagn.* **18**, 245–258 (2018).
4. Jermyn, M. et al. A review of Raman spectroscopy advances with an emphasis on clinical translation challenges in oncology. *Phys. Med. Biol.* **61**, R370–R400 (2016).
5. Austin, L. A., Osseiran, S. & Evans, C. L. Raman technologies in cancer diagnostics. *Analyst* **141**, 476–503 (2016).
6. Wang, W. B. et al. Real-time in vivo cancer diagnosis using Raman spectroscopy. *J. Biophotonics* **8**, 527–545 (2015).
7. Santos, I. P. et al. Raman spectroscopy for cancer detection and cancer surgery guidance: translation to the clinics. *Analyst* **142**, 3025–3047 (2017).
8. Baker, M. J. et al. Clinical applications of infrared and Raman spectroscopy: state of play and future challenges. *Analyst* **143**, 1735–1757 (2018).

9. Latka, I. et al. Fiber optic probes for linear and nonlinear Raman applications-current trends and future development. *Laser Photonics Rev.* **7**, 698–731 (2013).
10. Krafft, C. et al. Diagnosis and screening of cancer tissues by fiber-optic probe Raman spectroscopy. *Biomed. Spectrosc. Imaging* **1**, 39–55 (2012).
11. Pence, I. & Mahadevan-Jansen, A. Clinical instrumentation and applications of Raman spectroscopy. *Chem. Soc. Rev.* **45**, 1958–1979 (2016).
12. Desroches, J. et al. A new method using Raman spectroscopy for in vivo targeted brain cancer tissue biopsy. *Sci. Rep.* **8**, 1792 (2018).
13. St-Arnaud, K. et al. Development and characterization of a handheld hyper-spectral Raman imaging probe system for molecular characterization of tissue on mesoscopic scales. *Med. Phys.* **45**, 328–339 (2018).
14. Reisner, L. A. et al. A prototype biosensor-integrated image-guided surgery system. *Int. J. Med. Robot. Comput. Assist. Surgry* **3**, 82–88 (2007).
15. Lapeer, R. J. et al. Using a passive coordinate measurement arm for motion tracking of a rigid endoscope for augmented-reality image-guided surgery. *Int. J. Med. Robot. Comput. Assist. Surgry* **10**, 65–77 (2014).
16. Ashok, P. C. et al. A Raman spectroscopy bio-sensor for tissue discrimination in surgical robotics. *J. Biophotonics* **7**, 103–109 (2014).
17. GORPAS, D. et al. Real-time visualization of tissue surface biochemical features derived from fluorescence lifetime measurements. *IEEE Trans. Med. Imaging* **35**, 1802–1811 (2016).
18. Yang, W. et al. Raman ChemLighter: fiber optic Raman probe imaging in combination with augmented chemical reality. *J. Biophotonics* **12**, e201800447 (2019).
19. Lagarto, J. L. et al. Simultaneous fluorescence lifetime and Raman fiber-based mapping of tissues. *Opt. Lett.* **45**, 2247–2250 (2020).
20. Huang, Z. W. et al. Rapid near-infrared Raman spectroscopy system for real-time in vivo skin measurements. *Opt. Lett.* **26**, 1782–1784 (2001).
21. Huang, Z. W. et al. Near-infrared Raman spectroscopy for optical diagnosis of lung cancer. *Int. J. Cancer* **107**, 1047–1052 (2003).
22. Nicolau, S. et al. Augmented reality in laparoscopic surgical oncology. *Surg. Oncol.* **20**, 189–201 (2011).
23. Pratt, P. et al. Through the HoloLens™ looking glass: augmented reality for extremity reconstruction surgery using 3D vascular models with perforating vessels. *Eur. Radiol. Exp.* **2**, 2 (2018).
24. Lee, D. et al. In vivo near infrared virtual intraoperative surgical photoacoustic optical coherence tomography. *Sci. Rep.* **6**, 35176 (2016).
25. Morita, J. et al. MRI overlay system using optical see-through for marking assistance. In *Proceedings of the 2015 IEEE Virtual Reality (VR)* 239–240 (IEEE, 2015).
26. Tabrizi, L. B. & Mahvash, M. Augmented reality–guided neurosurgery: accuracy and intraoperative application of an image projection technique. *J. Neurosurg.* **123**, 206–211 (2015).
27. Yang, L. et al. Vision-based endoscope tracking for 3D ultrasound image-guided surgical navigation. *Comput. Med. Imaging Graph.* **40**, 205–216 (2015).
28. Mahmood, F. et al. Augmented reality and ultrasound education: initial experience. *J. Cardiothorac. Vasc. Anesth.* **32**, 1363–1367 (2018).
29. Baek, S. J. et al. Baseline correction using asymmetrically reweighted penalized least squares smoothing. *Analyst* **140**, 250–257 (2015).
30. Schie, I. W. et al. Direct comparison of fatty acid ratios in single cellular lipid droplets as determined by comparative Raman spectroscopy and gas chromatography. *Analyst* **138**, 6662–6670 (2013).
31. Amidror, I. Scattered data interpolation methods for electronic imaging systems: a survey. *J. Electron. Imaging* **11**, 157–176 (2002).
32. Rosin, P. L. Further five-point fit ellipse fitting. *Graph. Models Image Process.* **61**, 245–259 (1999).
33. Wang, J. & Fleischmann, D. Improving spatial resolution at CT: development, benefits, and pitfalls. *Radiology* **289**, 261–262 (2018).
34. Stucht, D. et al. Highest resolution in vivo human brain MRI using prospective motion correction. *PLoS ONE* **10**, e0133921 (2015).
35. Yang, W. et al. Development and evaluation of a hand-held fiber-optic Raman probe with an integrated autofocus unit. *Opt. Express* **28**, 30760–30770 (2020).
36. Barsky, S. & Petrou, M. The 4-source photometric stereo technique for three-dimensional surfaces in the presence of highlights and shadows. *IEEE Trans. Pattern Anal. Mach. Intell.* **25**, 1239–1252 (2003).
37. Zhang, Y. W. et al. A fast 3D reconstruction system with a low-cost camera accessory. *Sci. Rep.* **5**, 10909 (2015).
38. Quéau, Y. et al. LED-based photometric stereo: modeling, calibration and numerical solution. *J. Math. Imaging Vis.* **60**, 313–340 (2018).
39. Esteban, C. H., Vogiatzis, G. & Cipolla, R. Multiview photometric stereo. *IEEE Trans. Pattern Anal. Mach. Intell.* **30**, 548–554 (2008).

Supplementary information for

Real-time molecular imaging of near-surface tissue using Raman spectroscopy

Wei Yang[1], Florian Knorr[1], Ines Latka[1], Matthias Vogt[2], Gunther O. Hofmann[2], Jürgen Popp[1, 3], and Iwan W. Schie [1, 4, *]

[1]Leibniz Institute of Photonic Technology Jena, Albert-Einstein-Straße 9, 07745 Jena, Germany

[2]Department of Trauma, Hand and Reconstructive Surgery, University Hospital Jena, Am Klinikum 1, 07747 Jena, Germany

[3]Institute of Physical Chemistry and Abbe Center of Photonics, Friedrich-Schiller University Jena, Helmholtzweg 4, 07743 Jena, Germany

[4]Department of Medical Engineering and Biotechnology, University of Applied Sciences - Jena, Carl-Zeiss-Promenade 2, 07745 Jena, Germany

*Correspondence: Iwan W. Schie, Email: iwan.schie@leibniz-ipht.de

Supplementary Table S1. Representative Raman fiber optic probe designs and reported excitation and acquisition parameters, i.e. λ: wavelength, *P*: laser power, *t*: acquisition time, *FOV*: field of view, *SR*: spatial resolution.

Probe		Features	Typical parameters	Ref.
Endoscopic Raman probe	**Volume probe**	Without any focusing optics, simplest implementation	*λ:* 785 nm, *P*: 150 mW, *t*: 1 s	[1]
			λ: 720 nm, *P*: 7 mW, *t*: 20 s	[2]
	Confocal probe	Addition of extra optical components, e.g.		
		• Ball lens	*λ:* 785 nm, *P*: 15 mW, *t*: 1 s	[3,4]
		• Gradient index lens (GRIN lens)	*λ:* 830 nm, *P*: 60 mW, *t*: 1 s	[5]
		• Aspheric lenses	*λ:* 830 nm, *P*: 34 mW, *t*: 10 s	[6]
Handheld Raman probe		Robust, bulk, commercially available	*λ:* 785 nm, *P*: 350 mW, *t*: 0.2 s	[7]
			λ: 785 nm, *P*: 100 mW, *t*: 2 s	[8]
Fiber array-based approach		Imaging ability for small area		
		Fiber bundle + galvanometric scanner	*λ:* 532 nm, *FOV*: 0.07 mm^2, *SR*: a few µm	[9]
		Fiber bundle + galvanometric scanner	*λ:* 785 nm, *P*: 950 mW, *t*: 0.9 s, *FOV*: 14 mm^2, *SR*: <115 µm	[10]

Supplementary Figures

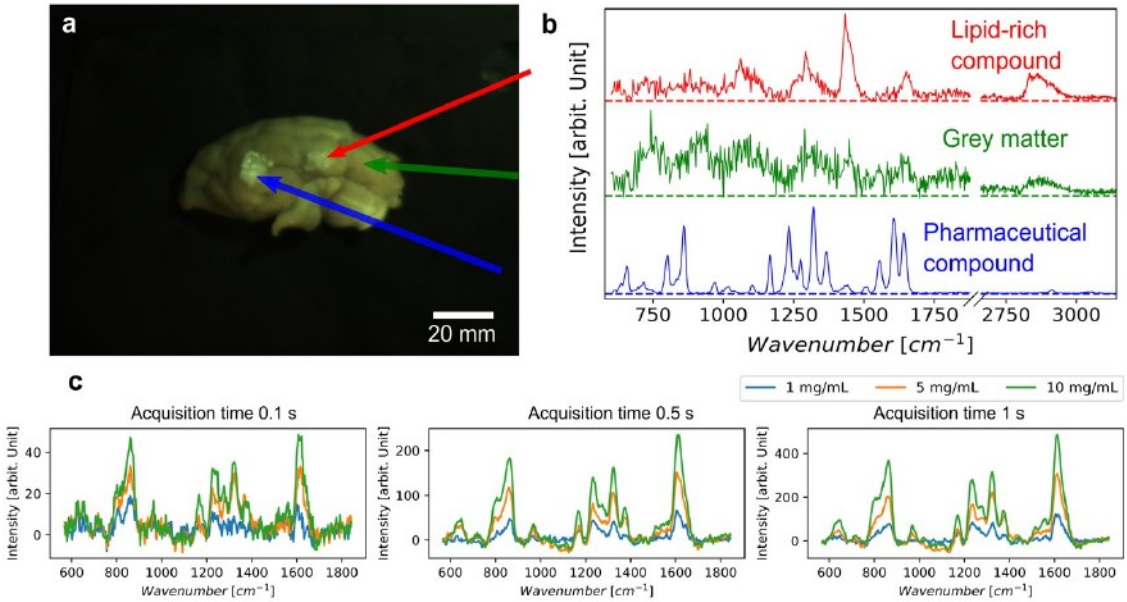

Fig. S1. a. Brightfield image of the 3D structured sample, i.e. a porcine brain sample where one area with a lipid-rich and one with a pharmaceutical compound are indicated. **b**. Relevant representative Raman spectra of the lipid-rich compound, grey matter, and pharmaceutical compound. **c.** Raman spectra of paracetamol solutions at different concentrations (mg mL^{-1}). The solution was pipetted onto a calcium fluoride (CaF_2) microscope slide and the probe was placed on a Z-direction manually adjustable stage with the laser focusing on the droplet. The laser power was set to approx. 100 mW, and three different acquisition time of 0.1, 0.5, 1 s were tested. The water concentration in each acquired Raman spectrum was removed through non-negative-least-squares fitting of a spectrum of the pure water[11].

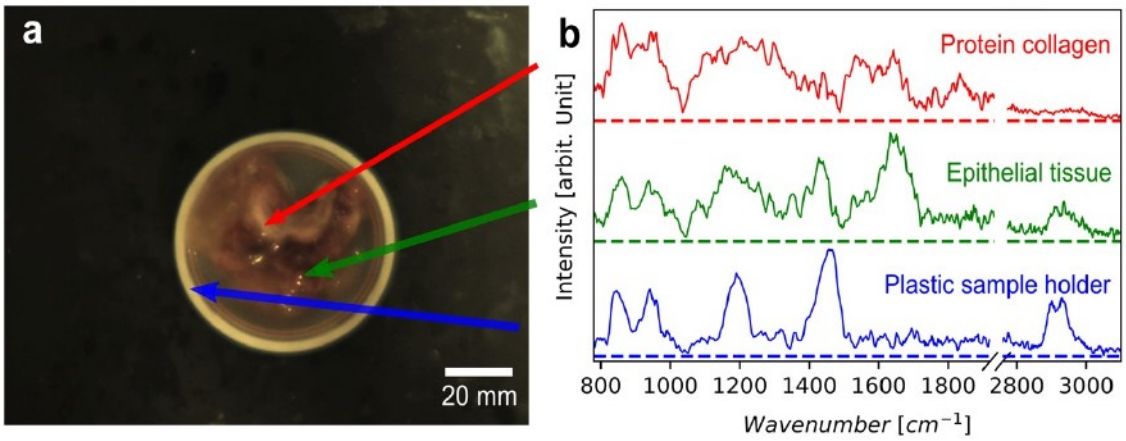

Fig. S2. a Brightfield image of an ex-vivo sample. **b** Representative Raman spectra of collage (red), epithel tissue (green), and plastic sample holder (blue).

Experimental results performed on an ex-vivo sample, which was resected from surgery for extensive intramuscular lipoma in the area of the pectoralis major muscle on the right for a 68-year-old patient with a size of 4 cm × 2.8 cm. The Raman image was reconstructed in about 160 s with 672 points. The brightfield image, Raman image, and the merged augmented image are shown in Figure S3a-c. The data gridding algorithm predicts the blank or missing points to fulfil the Raman image as shown in Figure S3d. The Raman image was back-projected on the sample surface which formed a live update mixed reality image to further obviously and straightforwardly present the biochemical information visually. Figure S3e and S3f show the mixed reality image of the Raman image on the ex-vivo sample with and without the data gridding and were captured by the external camera. Figure S3g shows the related Raman spectra of the chemical components. Since the sample was resected from the intramuscular lipoma, only lipid spectrum from the sample has been detected. The screen-record construction of the augmented image and video-record mixed reality by the external camera are edited to the same timeline in one video and attached as Supplementary Video S1.

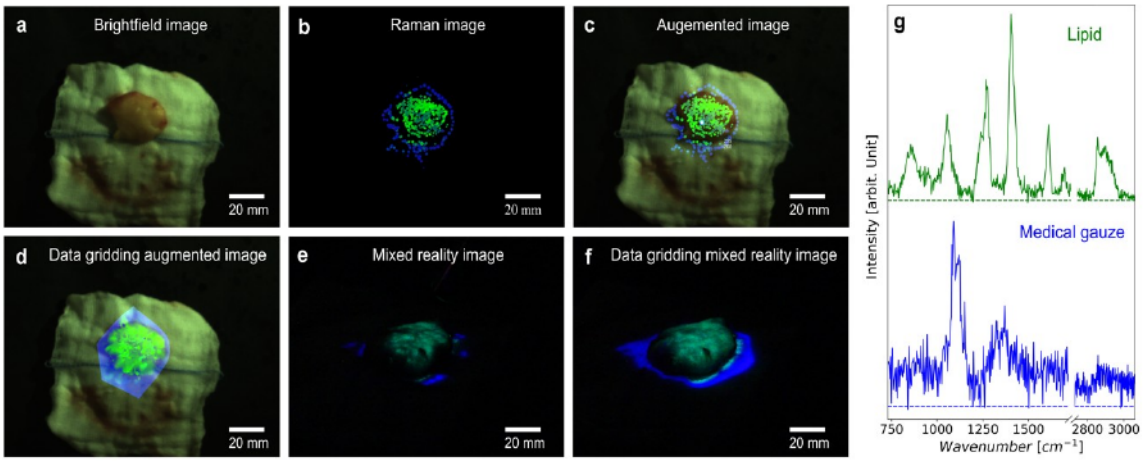

Figure S3. Representative results of the proposed approach on the ex-vivo clinical lipoma sample. **a** Brightfield image of the lipoma sample. **b** Reconstructed Raman image, with green representing the lipoma and blue the sample carrier. **c** Augmented molecular reality image of the lipoma sample. **d** Data gridding applied to the Raman image and overlaid with the brightfield image. **e** Back-projected Raman image on the sample, forming the mixed Raman reality image. **f** Interpolated mixed reality image. **g** The Raman spectra of different chemical components are assigned with pseudocolors, i.e. green for lipid, blue for cellulose fiber of the medical gauze.

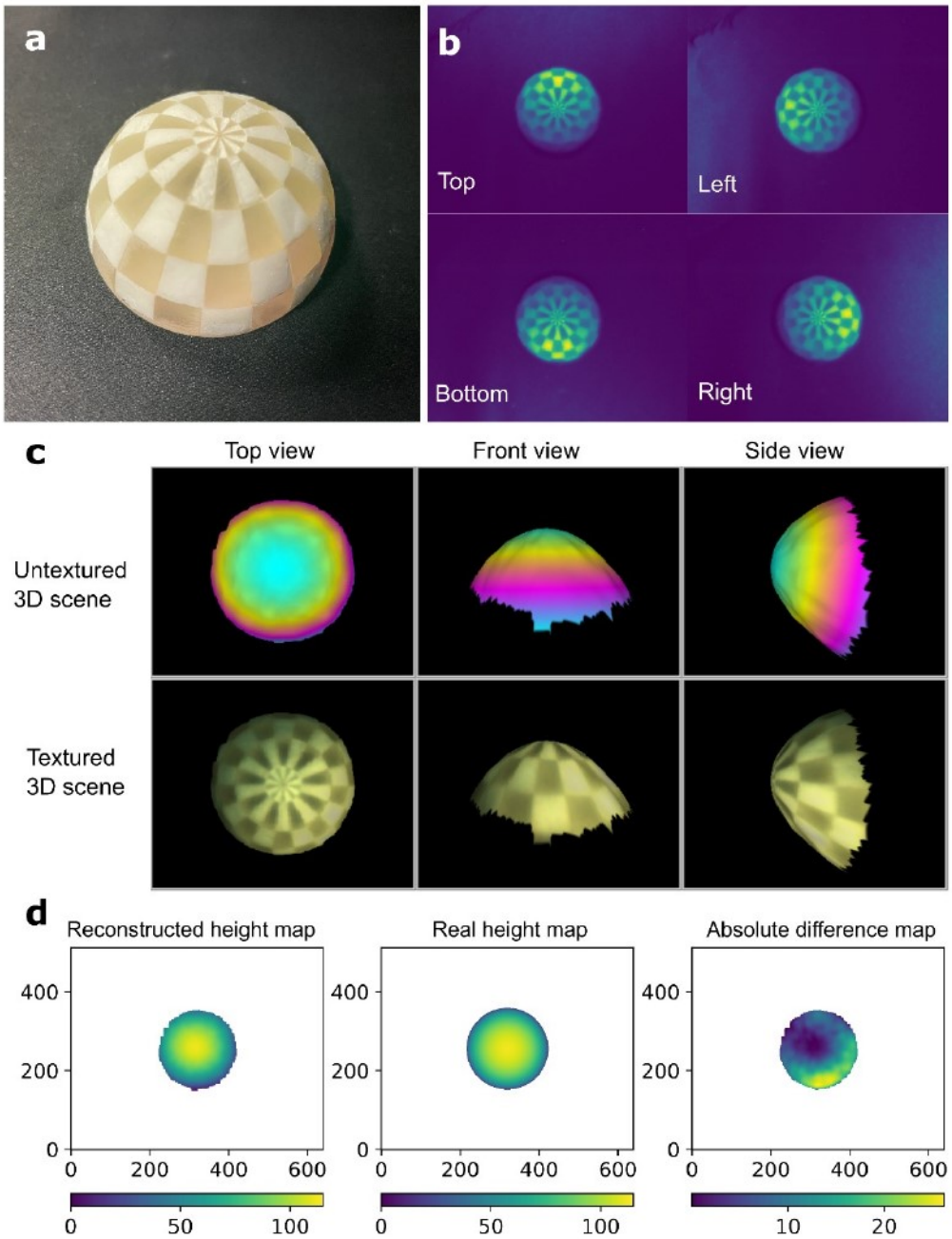

Fig. S4. 3D surface reconstruction of the hemisphere phantom. a A brightfield image of the phantom. **b** Intensity images under various orientations of light illumination: from the top, left, bottom, and right, respectively. **c** Reconstructed images under untextured 3D scene and textured 3D scene with different views: from the top, front, and side, respectively. **d** Height maps of the reconstructed and real hemisphere and the absolute difference between the reconstructed and real data. The real height map is plotted according to the equation: $z=\sqrt{r^2-(x-320)^2-(y-256)^2}+b$, here r = 104, (25 mm ÷ 0.24 mm pixel^{-1}) is the radius of the hemisphere, (320, 256) is the center of the image and b = 8.3 (2 mm) in the lower part of the phantom. The root-mean-square error (RMSE) between reconstructed and real is ~3.7 pixels (0.9 mm) and the normalized root-mean-square error (NRMSE) is 3.3%.

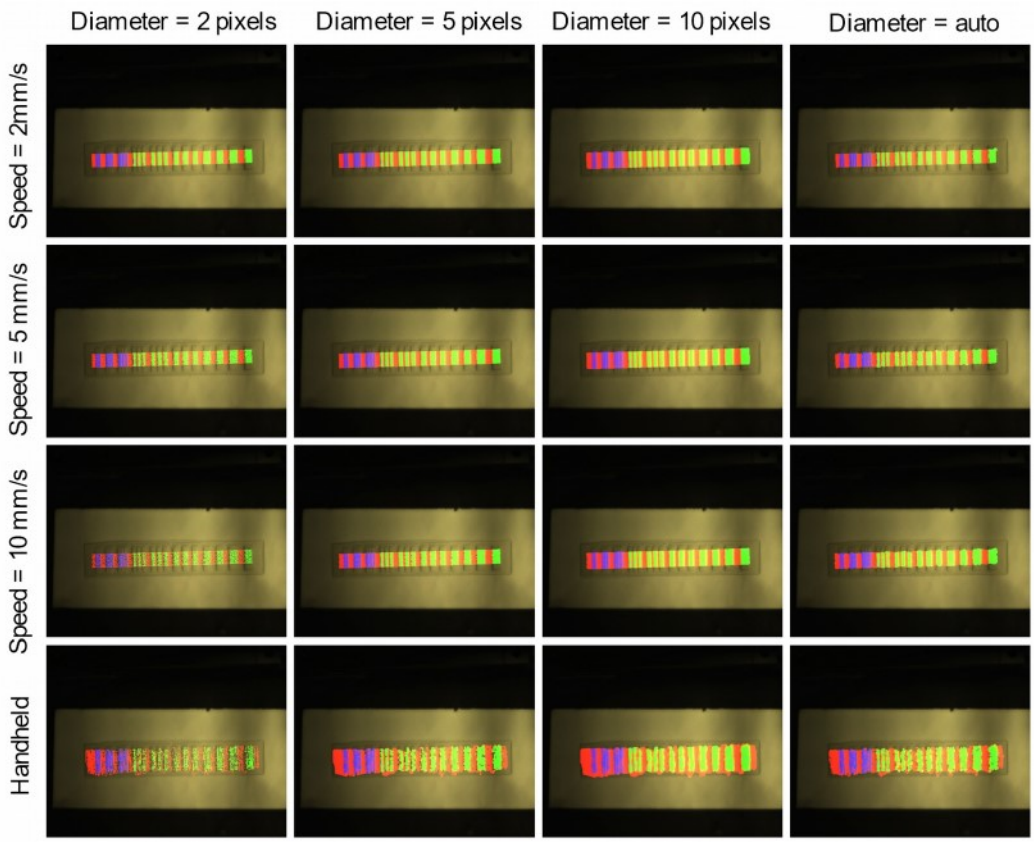

Fig. S5. Evaluation of the influence of scanning speed and mapping dimension on the spatial resolution and comparison to handheld operation. Raman images in combination with augmented reality were acquired automatically with a translational stage at various speeds, showing that for an increasing of the speed the fill-factor is reduced for a fixed diameter size. This can be improved by dynamically adjusting the circle diameter during the acquisition, resulting in an improved visualization of the molecular distribution during the real-time data acquisition and analysis. The reconstruction with different sizes of diameter and auto-scale according to the rules of Eq. (3).

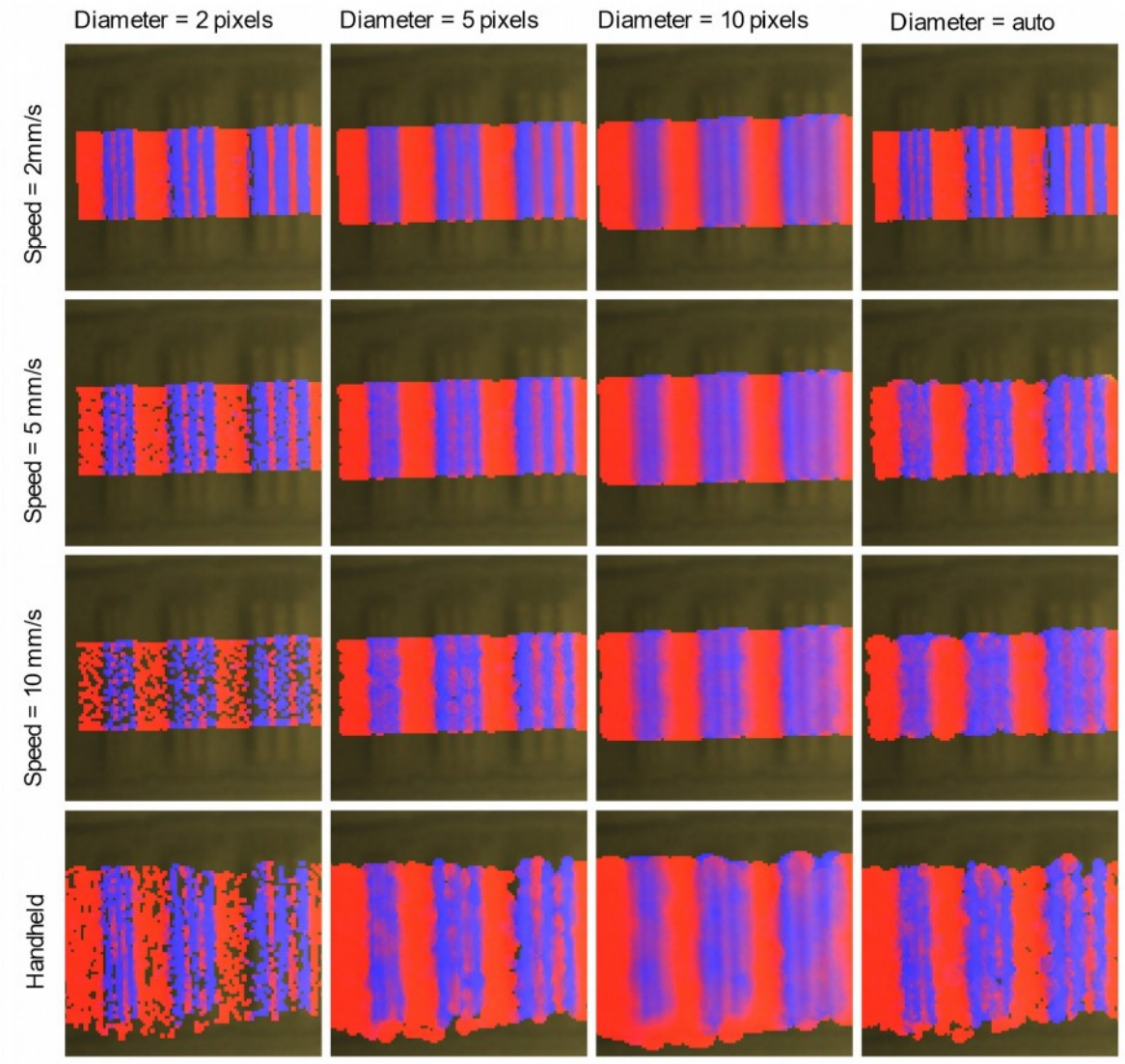

Fig. S6. Zoomed-in images for ROI outlined in Fig. S5, indicating the details for the resolution measurements.

Projector-camera calibration for mixed reality display

A coordinate checkerboard-based projector-camera calibration is applied for realizing the back-projecting of the molecular information on the sample[12–14]. The calibration flowchart is presented in Figure S7. A checkerboard image with 31 × 23 grid was created and projected on the sample plane by a projector and captured by the brightfield camera. For establishing the correlation function between the OpenCV[15] function cv2.findChessboardCorners( ) was applied to both, the original checkerboard image and the captured image. The detected positions of the corners were identified and displayed on both images as red dots. By applying the OpenCV function cv2. findHomography( ) to the detected points, a homographic matrix can be built to connect the projector and the camera, which indicates the rotation and translation between the projected image and the captured image.

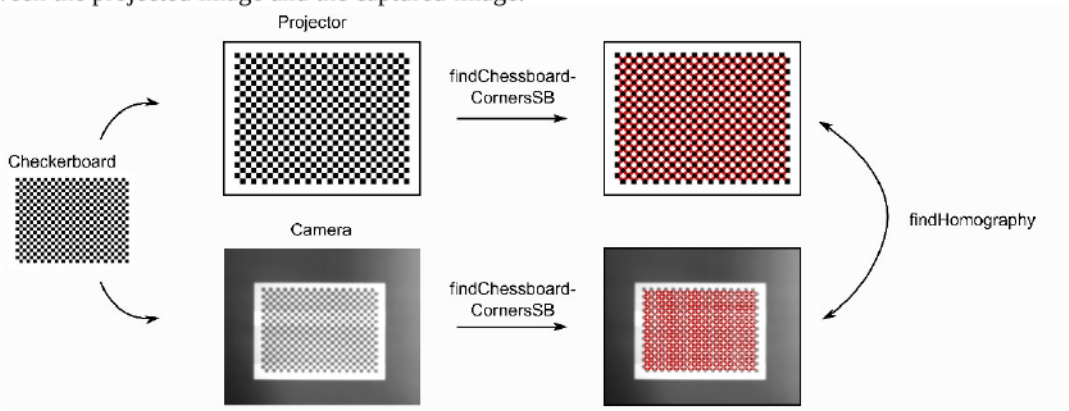

Fig. S7. The flowchart of projector-camera calibration.

Based on the homographic relationship, it is possible to transform the reconstructed molecular image to map it onto the sample. The performance was evaluated on five manually set points, which represent possible locations for acquire Raman data, in a test image, Figure 8Sa. Then, by applying the homographic matrix approach the coordinate locations can be transformed to match the checkerboard image, Figure S8b. By projecting the converted image onto the surface of the worktable, capturing the information by a brightfield camera, and determining the point positions it is possible to establish the deviation, Figure S8c. Comparing the points positions between S8a and S8c, one can get a root mean square error (RMSE) of ~1.5 pixels, which corresponds to normalized error of 0.3%, relative to the image size. Taking the spatial resolution of 0.24 mm per pixel (640 × 512 pixels for a field of view of ~15.6 cm × 12.5 cm) into account, there is a real mismatch of ~0.5 mm between the projected image and the real sample which is acceptable for the current implementation.

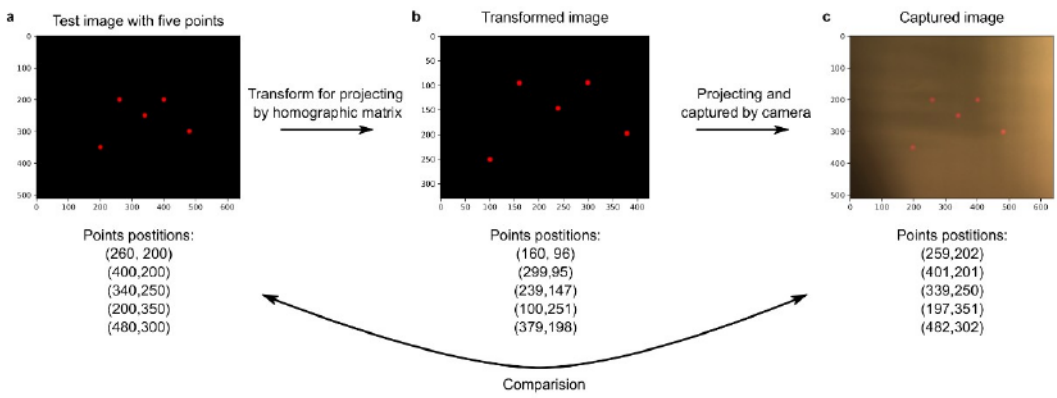

Fig. S8. Evaluation of projector-camera calibration by using five points. a Manually setting of five points as a test image and related positions. **b** Transformation of the original test image to the

projection image by homographic matrix and related transformed points positions, and **c,** the real captured image by the camera and related points positions.

Diagram of the probe

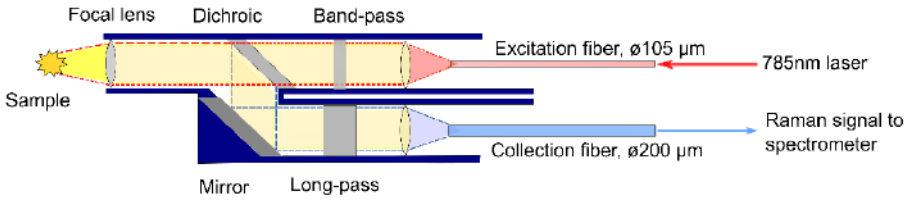

Fig. S9. The optical design of the handheld fiber-optic probe. The excitation laser is fiber-coupled through a 105 µm multi-mode fiber and passes through a 785 nm bandpass filter to remove the silica Raman background generated in the excitation fiber. After passing a dichroic mirror it is focus to the sample plane though an objective lens with a working distance of 7.5 mm and a numerical aperture (NA) of 0.22. The generated Raman signal is collected by the same objective lens, passes through a long-pass filter to remove the Rayleigh scattering signal and fiber-coupled into a 200 µm fiber, which is also used as the entrance aperture of the spectrometer.

Information of the supplementary videos:

Supplementary Video 1a. The 3D scene view record of the 3D structured sample in individual windows of non-textured height image, original color textured image, and augmented chemical textured image.

Supplementary Video 1b. The computer screen and mixed reality result of the molecular imaging for the 3D structured sample surface was screen-recorded and video-recorded by the external camera.

Supplementary Video 2. The computer screen of the Raman imaging for the ex-vivo sample was screen-recorded.

Supplementary Video 3. The 3D scene view record of the hemisphere phantom in individual panels of non-textured height image, original color textured image, Raman textured height image, and augmented chemical textured height image.

Supplementary Video S1. The computer screen and mixed reality result of the molecular imaging for the extra ex-vivo sample was screen-recorded and video-recorded by the external camera.

Reference

1 Shim MG, Wilson BC, Marple E, Wach M. Study of Fiber-Optic Probes for in vivo Medical Raman Spectroscopy. *Appl Spectrosc* 1999; **53**: 619–627.

2 Komachi Y, Sato H, Aizawa K, Tashiro H. Micro-optical fiber probe for use in an intravascular Raman endoscope. *Appl Opt* 2005; **44**: 4722.

3 Motz JT, Hunter M, Galindo LH, Gardecki JA, Kramer JR, Dasari RR *et al.* Optical Fiber Probe for Biomedical Raman Spectroscopy. *Appl Opt* 2004; **43**: 542.

4 Mo J, Zheng W, Huang Z. Fiber-optic Raman probe couples ball lens for depth-selected Raman measurements of epithelial tissue. *Biomed Opt Express* 2010; **1**: 17.

5 Almond LM, Hutchings J, Kendall C, Day JCC, Stevens OAC, Lloyd GR *et al.* Assessment of a

custom-built Raman spectroscopic probe for diagnosis of early oesophageal neoplasia. *J Biomed Opt* 2012; **17**: 0814211.

6 Day JCC, Bennett R, Smith B, Kendall C, Hutchings J, Meaden GM *et al.* A miniature confocal Raman probe for endoscopic use. *Phys Med Biol* 2009; **54**: 7077–7087.

7 Zhang Y, Liu H, Tang J, Li Z, Zhou X, Zhang R *et al.* Noninvasively Imaging Subcutaneous Tumor Xenograft by a Handheld Raman Detector, with the Assistance of an Optical Clearing Agent. *ACS Appl Mater Interfaces* 2017; **9**: 17769–17776.

8 Karabeber H, Huang R, Iacono P, Samii JM, Pitter K, Holland EC *et al.* Guiding Brain Tumor Resection Using Surface-Enhanced Raman Scattering Nanoparticles and a Hand-Held Raman Scanner. *ACS Nano* 2014; **8**: 9755–9766.

9 Doronina-Amitonova L V., Fedotov I V., Fedotov AB, Zheltikov AM. High-resolution wide-field Raman imaging through a fiber bundle. *Appl Phys Lett* 2013; **102**: 161113.

10 St-Arnaud K, Aubertin K, Strupler M, Madore WJ, Grosset AA, Petrecca K *et al.* Development and characterization of a handheld hyperspectral Raman imaging probe system for molecular characterization of tissue on mesoscopic scales. *Med Phys* 2018; **45**: 328–339.

11 Duraipandian S, Knopp MM, Pollard MR, Kerdoncuff H, Petersen JC, Müllertz A. A fast and novel internal calibration method for quantitative Raman measurements on aqueous solutions. *Anal Methods* 2018; **10**: 3589–3593.

12 Zhang Z. A flexible new technique for camera calibration. *IEEE Trans Pattern Anal Mach Intell* 2000; **22**: 1330–1334.

13 Chum O, Pajdla T, Sturm P. The geometric error for homographies. *Comput Vis Image Underst* 2005; **97**: 86–102.

14 Moreno D, Taubin G. Simple, accurate, and robust projector-camera calibration. *Proc - 2nd Jt 3DIM/3DPVT Conf 3D Imaging, Model Process Vis Transm 3DIMPVT 2012* 2012; : 464–471.

15 OpenCV Tutorials. https://docs.opencv.org/master/d9/dab/tutorial_homography.html.

8. Erklärungen

Selbständigkeitserklärung

Ich erkläre, dass ich die vorliegende Arbeit selbständig und unter Verwendung der angegebenen Hilfsmittel, persönlichen Mitteilungen und Quellen angefertigt habe.

Ort, Datum Unterschrift

Erklärung zu den Eigenanteilen der Promovend sowie der weiteren Doktoranden/Doktorandinnen als Koautoren an den Publikationen und Zweitpublikationsrechten bei einer kumulativen Dissertation

Für alle in dieser kumulativen Dissertation verwendeten Manuskripte liegen die notwendigen Genehmigungen der Verlage ("Reprint permissions") für die Zweitpublikation vor.

Die Co-Autoren der in dieser kumulativen Dissertation verwendeten Manuskripte sind sowohl über die Nutzung, als auch über die oben angegebenen Eigenanteile der weiteren Doktoranden/Doktorandinnen als Koautoren an den Publikationen und Zweitpublikationsrechten bei einer kumulativen Dissertation informiert und stimmen dem zu.

Ort, Datum Unterschrift der Promovend

Wei Yang

Ich bin mit der Abfassung der Dissertation als publikationsbasierte, d. h. kumulative, einverstanden und bestätige die vorstehenden Angaben. Eine entsprechend begründete Befürwortung mit Angabe des wissenschaftlichen Anteils der Doktorand an den verwendeten Publikationen werde ich parallel an den Rat der Fakultät der Chemisch-Geowissenschaftlichen Fakultät richten.

Ort, Datum Unterschrift der Erstbetreuer

Prof. Dr. Jürgen Popp

Conference and Workshop

- Raman ChemLighter: Fiber Optic Probe-Based Raman Imaging using Positional Tracking, FT-IR Workshop in Spectroscopy in Microbiological and Medical Diagnostics-Berlin, Germany 2017 (Poster presented), Wei Yang, Iwan W. Schie, and Jürgen Popp

- Raman ChemLighter: A Fiber-optic probe-based Raman imaging approach in combination with augmented reality and mixed reality, Bunsentagung - Jena, Germany 2019 (Poster presented), Wei Yang, Iwan W. Schie, and Jürgen Popp

9. Acknowledgments

I would like to express gratitude to Prof. Dr. Jürgen Popp for allowing me to carry out my doctoral research in this interdisciplinary working group, and for all his constructive comments, suggestions, and support. I would like to express my great gratitude to Prof. Dr. Iwan W. Schie for all his patience, invaluable ideas, suggestions, comments, and kind encouragement in every step of the research. I learn a lot under their supervision which encourages me to explore and enjoy academic research.

I also like to thank Ines Latka, Dr. Jan Rüger, and Dr. Clara Stiebing for their kind suggestions, advice on my research and publications, and for their kind review and correction of the thesis. I like to thank Florian Knorr and David VasquezPinzon for their support, discussion, and sharing the knowledge and skills with the technical. Special thanks go to Florian, Saif, Mohammed, and Tanveer for their encouragement as a friend throughout the doctoral study. I also want to thank the support of my group members in the multimodal instrumentation group and colleagues from the IPHT for various constructive discussions, suggestions. I acknowledge the China Scholarship Council and the IPHT for financial support.

Finally, I would like to sincerely thank my wife for her selfless dedication and my family for their consistent support and understanding. I also thank my friends in China for their encouragement to my doctoral study.